TECHNICAL UNIVERSITY OF LIBEREC

Faculty of Mechanical Engineering

AN INVESTIGATION INTO SELECTED TYPES OF FLOW

By

Tomáš Vít

Applied Mechanics /
Fluid Mechanics and Thermodynamics

Liberec 2009

ACKNOWLEDGMENTS

Without the leadership and hardwork by Zdeněk Trávníček this research would not have been possible. I would also like to thank the Faculty of Mechanical Engineering of Technical University of Liberec, especially the Department of Power Engineering Equipment for the use of their laboratories, equipment and for the considerable help of their employees.

I also gratefully acknowledge the support of the Grant Agency of the Czech Republic (GAČR: 101/05/2681, 101/05/2537, 202/04/1341), Grant Agency of the Academy of Science of the Czech Republic (GAAV ČR: IAA200760504, IAA200760801), Academy of Science of Czech Republic (N.6, IT No. 50026) and the Research Target of the Ministry of Education of the Czech Republic MSM 4674788501

CONTENTS

List of Symbols

A	[1]	calibration constant
a	[K^{-1}]	amplitude of fluctuations
A	[m^2]	area
a_h	[1]	overheat ratio
B	[1]	calibration constant
C		calibration constant
c	[1]	piezoelectric coefficient tensor
d	[m]	diameter
D	[m]	vector of electric flux density
d	[s^{-1}]	tensor of strain rate
E	[J]	total energy
E_k	[J]	kinetic energy
E_p	[J]	potential energy
E_{wire}	[V]	wire voltage
f	[Hz]	frequency
f(x)		function of x
Gr	[1]	Grasshoff number
h	[$Wm^{-2}K^{-1}$]	heat transfer coefficient
I	[A]	current
k_p	[Nm^{-1}]	stiffness of the membrane
l	[m]	length
L	[m]	length
m	[kg]	mass
n	[1]	calibration exponent
N	[1]	parameter of velocity profile
Nu	[1]	Nusselt number
p	[Pa]	pressure
Pr	[1]	Prandtl number
Q	[W]	heat flux
R	[-]	dimensionless velocity (2.12)
R_{20}	[Ω]	resistance of wire at 20°C
R_a	[Ω]	resistance of wire at ambient temperature T_a
Re	[1]	Reynolds number
Re_{cr}	[1]	critical Reynolds number
Re_{eff}	[1]	effective Reynolds number
$\overline{Re}$	[1]	Reynolds number (2.12)
Ri	[1]	Richardson number
R_{wire}	[Ω]	resistance of heated wire at temperature T_{wire}
s	[1]	exponent
S	[1]	strain tensor
Sc	[1]	Schmidt number
Sh	[1]	Sherwood number
Sn	[1]	Stanton number
St	[1]	Strouhal number
$S_{u,CT}$	[V m^{-1}s]	CT mode velocity sensitivity
$S_{\theta,CT}$	[V K^{-1}]	CT mode temperature sensitivity

T	[K]	temperature
T	[Pa]	stress tensor
t	[s]	time
T_∞	[K]	ambient temperature
T^*	[1]	temperature ratio
TI	[1]	turbulence intensity
T_{wire}	[K]	temperature of heated wire
u	[ms^{-1}]	instantaneous velocity
U	[ms^{-1}]	steady velocity
$\overline{U}$	[ms^{-1}]	mean velocity
u'	[ms^{-1}]	fluctuating part of velocity
x, y, z		Cartesian coordinates, curvilinear orthogonal coordinates
y	[m]	coordinate
z	[m]	amplitude of the membrane
Θ	[1]	dimensionless temperature difference
α_{20}	[1]	temperature coefficient of resistivity at 20°C
δ	[m]	half-wide of the wake
ε	[1]	permittivity tensor
λ	[$Wm^{-1}K^{-1}$]	thermal conductivity
μ	[$kgm^{-1}s^{-1}$]	molecular viscosity
ν	[m^2s^{-1}]	kinematic viscosity
ν_{eff}	[m^2s^{-1}]	effective viscosity
ρ	[kgm^{-3}]	density of fluid
σ		standard deviation
ω	[s^{-1}]	angular velocity

Abbreviations

CC	constant current
CT	constant temperature
HWA	hot wire anemometry
NS	Navier-Stokes equation
SJ	synthetic jet
MJ	mixed jet
HSJ	hybrid synthetic jet
CJ	continuous jet
A	absolute unstable
C	convective unstable

CHAPTER 1

OUTLINE AND SCOPE OF THE THESIS

This habilitation thesis introduces a selection of important publications that are the results of scientific research during the last four years (2004-2008). The results of research into the problems of flow behind a heated bluff body in water and problems of synthetic jets (SJ) are presented here. As all the publications are in English the introductory and concluding chapters of this thesis are also provided in English.

1.1. Flow Behind a Bluff Body

The problem of the flow behind a bluff body has been studied for over a hundred years (V.Strouhal-1878; F.Albhorn-1902; A.Mallock-1907; T.von Kármán and H.Rubach-1912; Lord Rayleigh-1915) and has always been a topical problem. Perhaps it is because this apparently simple problem involves three shear layer interactions: a boundary layer, a separation shear layer and a wake. Each of these shear layers significantly influences the global character of the flow. The problem is usually solved experimentally and by analyzing the stability of the boundary layer, or by numerical simulation.

The research on the wake behind a bluff body covers a vast number of topics. It involves the seemingly simple problem of determining the value of the critical Reynolds number but also deals with 3D effects, such as problems of parallel *x* oblique vortex shedding or the influence of end effects. The onset of 3D structures in a wake such as an *A-mode* and *B-mode* transition is also studied. The combination of different structures of bluff bodies is important from an engineering point of view.

Another interesting group of experiments is non-isothermic experiments. In these experiments the influence of the temperature on the onset of the von Kármán vortex street (for low values of overheat- see *Chapter 4*) and the development of 3D structures (for higher values of overheat) are studied.

Fig. 1.1 von Kármán vortex street at Re=75. Unpublished results.

From this enormous range of topics the problem of stability of the flow behind a heated bluff body in water was chosen and studied. The presented work shows the experimental setup, results and comparison of these results with previous experiments carried out in air and with theoretical assumptions.

1.2. Synthetic Jets

Chapters 5 to 10 present the problem of a synthetic jet from primary experiments that were carried out to get a general idea of the character of the flow. This work presents a range of experiments and problems that were solved in the previous four years, and shows the basic principle and applications of a synthetic jet. The theory of synthetic jet actuators and basic experiments carried out in air and in water as working fluids are also presented. From the large family of application areas of synthetic jets the problem of intensifying heat transfer was chosen for the research. Four different constructions – synthetic jet, hybrid jet, mixed jet and continuous jet – are compared with respect to intensity of heat transfer from the affected wall. Other analysis is focused on the dynamics and characteristics of the actuator. Both numerical simulation and experimental study are used to identify the motion of the actuator and its response to different driving signals.

The presented publications are not the work of a single author but a team of scientists. The author of this thesis was mainly responsible for preparing and carrying out the published experiments and numerical simulations.

These publications are presented as they were published in journal proceedings. Some reformatting has been done and typographical errors have been edited for use in this thesis.

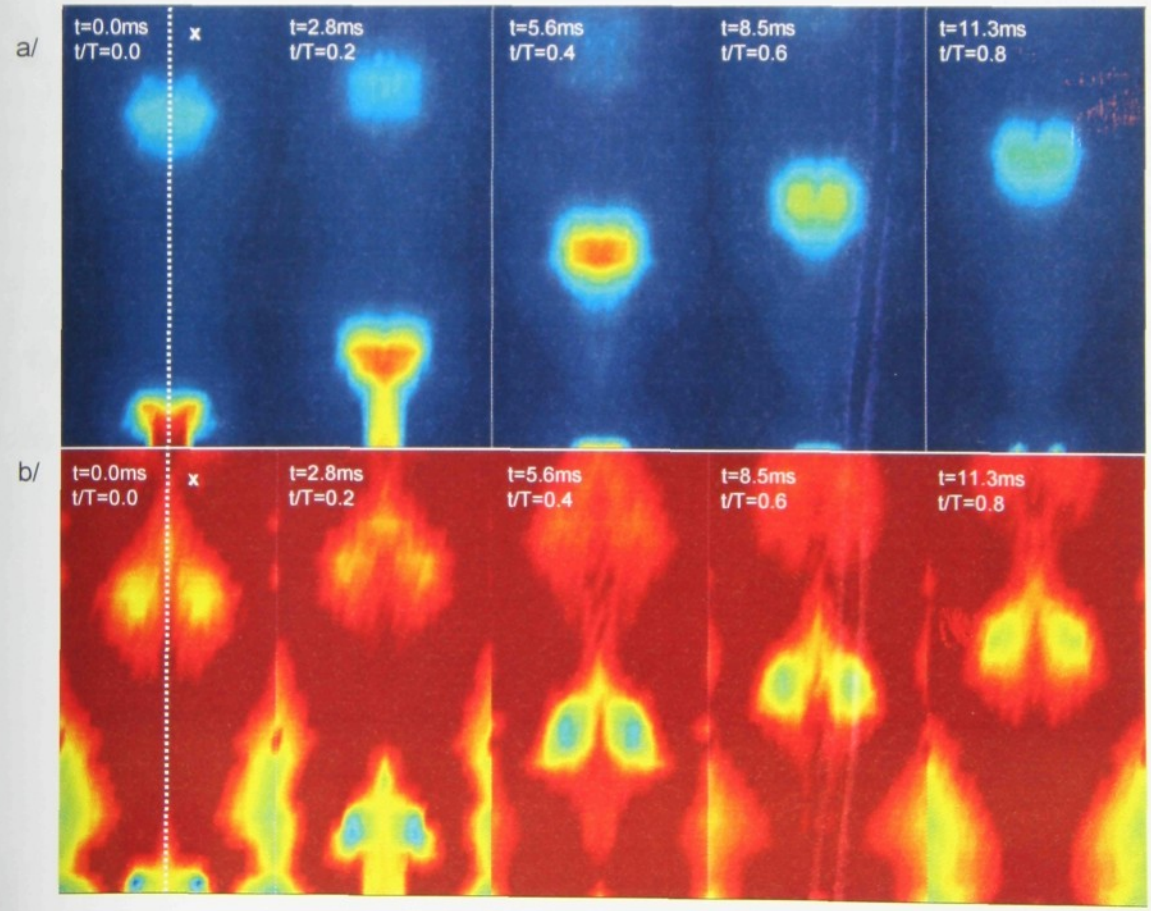

Fig. 1.2 The structure of Synthetic Jet – results from 2D HWA experiments. Frequency of the actuator is 72Hz. a/ velocity; b/ angle of the velocity vector. From [2].

While bluff body flow and synthetic jets seem to be different topics in fact they are very closely related fields and the findings obtained from studying the flow behind a bluff body can be very useful for the study of synthetic jets and vice versa. SJ flow can be used to control the wake in certain applications and the temperature of the circumfluence wall (see Vít[1]). Such cases will be presented in the following chapters.

1.3. Structure of the Thesis

The introductory chapters describe the observed phenomena and the progress in research during the previous years as later presented in particular publications. The details of the observed problems that were not published in presented publications are mentioned in *Chapter 2* .

Most of the presented projects are in connection with experiments using CTA methods and flow visualization. The third chapter therefore contains a brief description of the basic principle of CTA. The chapter mainly focuses on special techniques such as phase averaging of the acquired data or the use of CTA in water and conducting liquids. Also mentioned are the basic principles of visualization methods used, such as smoke wire visualization, tin ion visualization and the basic principle of the naphthalene sublimation method, which is frequently used to determine the heat transfer coefficient.

Selected papers from the years 2004-2008, which show an overview of the achieved results, are presented in the next chapters (*Chapters 4 - 10*). Issues of the stability of a heated bluff body wake are covered in the article "The influence of temperature gradient on the Strouhal-Reynolds number relationship for water and air", published in "Experimental Thermal and Fluid Science (2007)". The problems of synthetic jet flow and related topics are presented in the articles "Synthetic jets actuation at the resonance frequency/ICTAM2004"; "Hybrid synthetic jet intended for enhanced jet impingement heat/mass transfer/ IHTC-13"; "Heat/mass transfer of the pulsatile impinging jets/THMT-5"; "Analysis of SJ Piezo-Ceramic Pulsation Generator/Developments in Machinery Design and Control 2007"; and "Analysis of the Synthetic Jet/JASTFM2008".

The concluding chapter reviews the fundamental findings and presents some ideas for future research in the fields of boundary layer stability and synthetic jets.

CHAPTER 2

INTRODUCTION TO RESEARCH TOPICS

2.1. Flow Behind a Bluff Body

Chapter 4 of this thesis is focused on the experimental study of the influence of temperature and temperature gradient on the *St-Re* relationship in water. Research on non-isothermal effects connected with the wake and stability of the flow is just a small part of the research activities carried out in many laboratories and research centers worldwide. Because the present article deals with non-isothermal flow it provides only a short overview of the problem of flow behind a bluff body in the isothermal case and the stability of the flow. Fundamental information about the flow past the bluff body and the stability of the flow are mentioned below.

Fig.2.1 Vortex street in the wake of Selkirk island - caught by LANDSAT 7 on 9/15/1999 (top)
Flow in a bundle of tubes in alternate rows-from Henri Werlé, Courants et Couleurs published in 1974 by ONERA (bottom)

2.1.1. Regimes of vortex shedding

Examples of flow behind a bluff body can be found almost everywhere, from microcomputer systems and insect motion to airplanes and the atmosphere (Fig. 2.1). Although it has been a subject of interest to engineers and scientists for more than a hundred years (Strouhal [5], Rayleigh [6], Kármán [7]), many phenomena still lack a satisfactory explanation. The flow behind a bluff body is not only of interesting to scientists, but is also a kind of art made by nature. Pictures of the so-called von Kármán vortex street and other regimes of flow behind a bluff body can be found in many varieties in scientific publications as well as on the internet.

The following regimes are observed as the Reynolds number increases:

Potential (creeping) flow $Re \to 0$

According to potential theory, the flow around a circular cylinder experiences no drag. The zero net pressure drag results in a symmetric streamline pattern (Fig. 2.2a).

Low Re ($Re < Re_{cr}$)

The boundary layer in the vicinity of a solid wall is a source of vorticity and reverse pressure

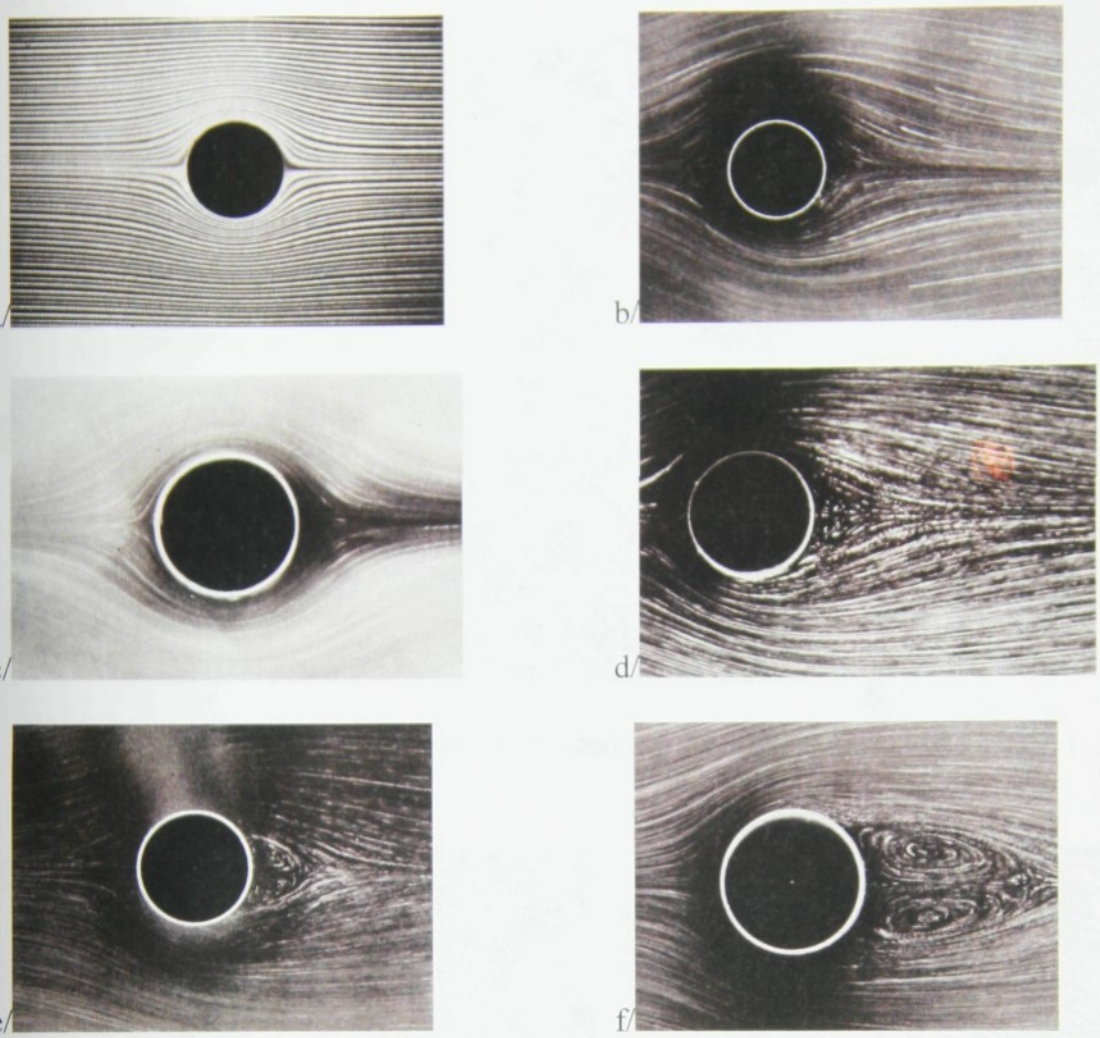

Fig. 2.2 Regimes of the flow past bluff body: a/ creeping flow $Re \to 0$; b/ Re=0.16; c/Re=1.54; d/Re=9.8; e/ Re=13.1; f/ Re=26. (From Van Dyke[9])

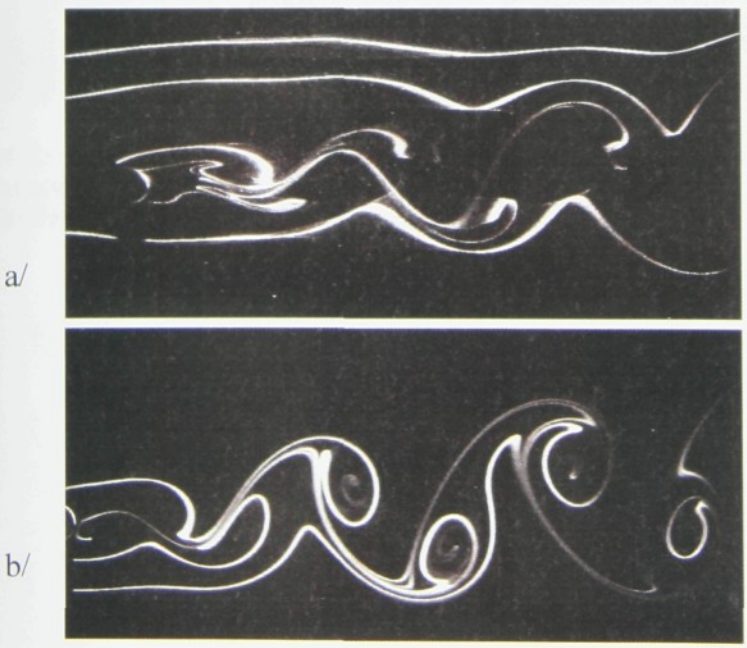

Fig. 2.3 Von Kármán vertex street: a/ Re=68; b/ Re=85 (unpublished results)

c/

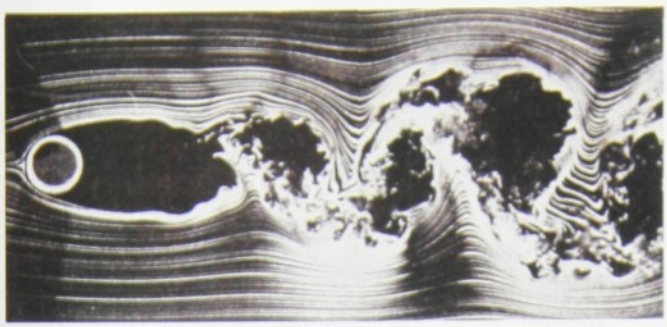

d/

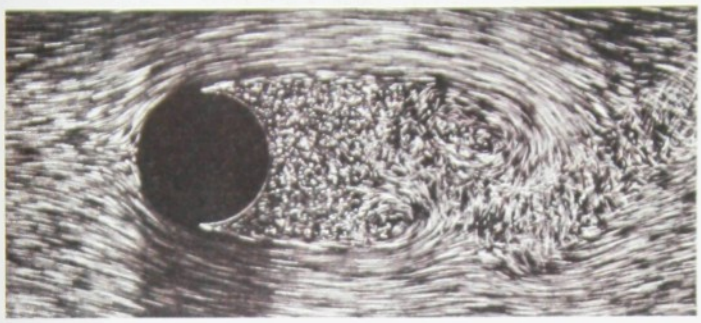

Fig. 2.3 Von Kármán vertex street: c/ *Re*=2000; d/ *Re*=10000 (From Van Dyke[9])

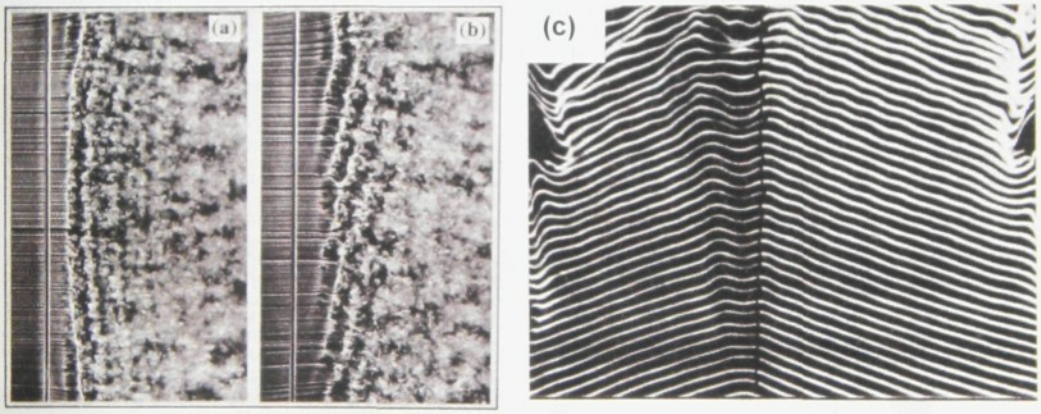

Fig. 2.4 Examples of 3D structures a/parallel vortex shedding in turbulent regime *Re*=10000; b/oblique vortex shedding in turbulent regime *Re*=10000 c/chevrons structures. (a/ and b/ from Williamson[8], c/ form Williamson[10).

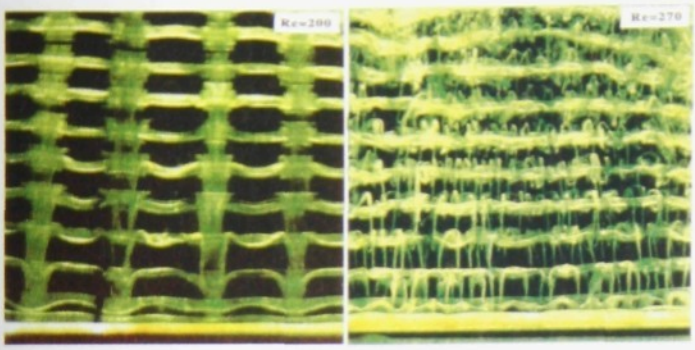

Fig.2.5 A-mode (Re=200) and B-mode (Re=208) instabilities. Wavelength of the instabilities is 4d for *A-mode* and 0.8d for *B-mode*. From Williamson[8].

gradient. Even for a small *Re*, the flow separates from the surface and results in asymmetry between the front and rear of the cylinder. The symmetry in x is lost and vorticity is generated at the rear end of the cylinder (Fig. 2.2b). When the *Re* increases beyond 4, the flow remains steady but a recirculation bubble composed of two counter-rotating vortices appears behind the cylinder (Fig. 2.2c). The length of the recirculation area increases with the Reynolds number (Fig. 2.2d-f).

Von Kármán vortex street ($Re>Re_{cr}$)

At a Reynolds number beyond 40 the wake becomes unstable and a so-called von Karman vortex street appears. At $47<Re<80$, the vortex street does not interact with the pair of attached vortices (Fig. 2.3a). As *Re* increases beyond 80 the vortex street forms close to the cylinder (Fig. 2.3b). While the eddy on one side is shedded, the one on the opposite side forms.

High Re

At $Re<300{,}000$ the boundary layer around the cylinder remains laminar (Fig. 2.3c), while in the range from 300,000 to 3,000,000 the boundary layer undergoes a transition to turbulence (Fig. 2.3d).

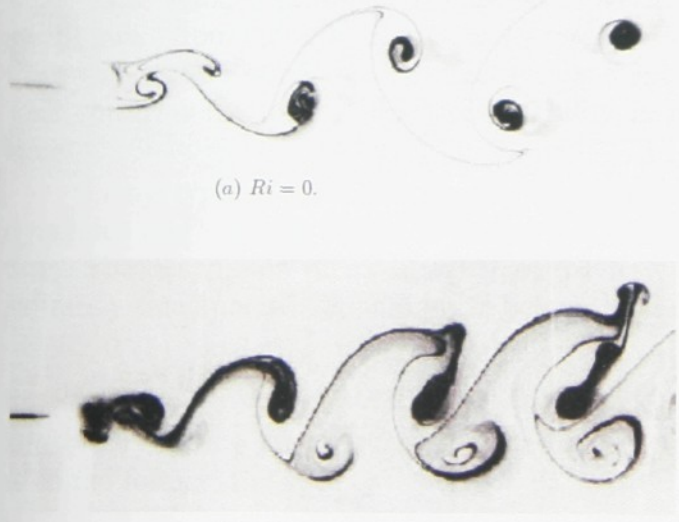

(a) $Ri = 0.$

(b) $Ri = 1.0$

Fig 2.6. The influence of the temperature on a structure of the wake-so called E-mode transition. Mushroom type structures are evident at the top of individual vortices.

3D effects

At low values of *Re* two different regimes – parallel and oblique – of vortex shedding are observed (Fig. 2.4a,b). These regimes are assumed to be caused by end effects (see Williamson [10]).

The flow behind a bluff body remains 2D up to *Re* of around 190. For the highest values of *Re*, three dimensional instability (primary vortex core and braid layer) starts to develop. These instabilities are often denoted as *mode-A* and *mode-B* instabilities (Fig. 2.5a,b).

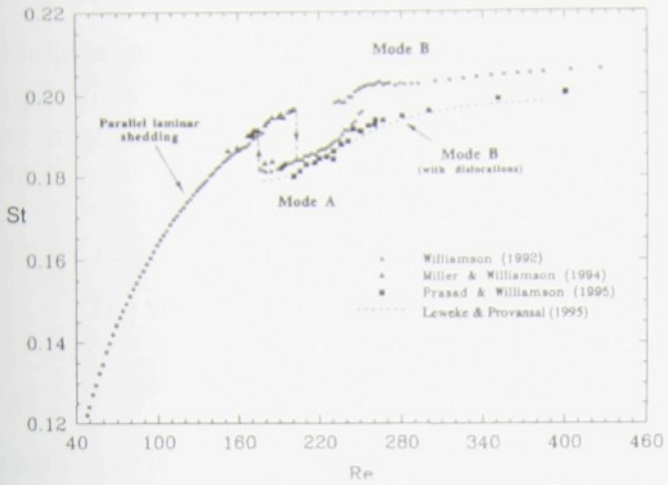

Fig. 2.7. Strouhal number as a function of a Reynolds number

These instabilities are of great interest nowadays. Much attention is also devoted for example to research on the influence of induced heat on 3D structures (Ren [11]- Fig. 2.6).

The development of the flow behind a bluff body, especially the non-dimensional frequency expressed by the Strouhal number, as a function of the Reynolds number, is shown in Fig. 2.7. It shows the onset of the von Kármán vortex street, the increase of the *St* with the *Re* and the areas of the *A-mode* and *B-mode* transitions.

2.1.2. Instability of flow

According to the experimental observations, some spatial-developing shear flows such as co-flowing shear layers or wakes at Reynolds numbers below the onset of the Kármán vortex street behave as noise amplifiers Huerre [12] that are sensitive to external noise. Other flows such as the wake below the critical *Re* value behave as flow oscillators operating on a well-defined frequency insensitive to low noise levels.

This means that the wake behind the cylinder undergoes a transition from noise amplifier to flow oscillator when the *Re* increases to the critical Reynolds number.

The characteristic of flow instability is determined by the behavior of its impulse response. The velocity profile is denoted as locally *absolutely unstable* if localized disturbances spread upstream and downstream and contaminate the flow.

The velocity profile is denoted as locally *convective unstable* if disturbances are swept away from the source. According to experimental observations of Provensal [13] the onset of the Kármán vortex street results from the time-amplified global instability. This confirms the role of absolute instability in the onset of the von Kármán vortex street.

Any type of flow that occurs in nature must satisfy the equations of fluid dynamics and must be stable. It means that small perturbations should decrease with time. The description of the stability of the flow behind a bluff body with respect to infinitely small perturbations is given below (Landau [14]).

We can define the instantaneous velocity $u(x,t)$ as the superposition of the steady velocity $U(x)$ and perturbation $u'(x,\ t)$ as $u(x,t)=U(x)+u'(x,t)$. When we substitute this into the momentum and continuity equations we obtain the equations for u′ in the form:

$$\frac{\partial u'}{\partial t}=(U\cdot\nabla)u'+(u'\cdot\nabla)U=-\frac{1}{\rho}\nabla p'+\nu\nabla^2u';\ \nabla\cdot u'=0 \qquad (2.1)$$

The general solution of these equations can be represented as a sum of particular solutions in which $u' \approx e^{-i\varpi t}$. The solution for $\varpi = \omega + i\gamma$ must satisfy Eq. (2.1) with appropriate boundary conditions. For the flow to be stable it is necessary that the imaginary part γ is negative. The perturbation will then decrease exponentially with time.

2.1.3. Onset of the von Kármán vortex street

The velocity u' can be written as:

$$u'(x,t) = \phi(x)a(t), \tag{2.2}$$

where $\phi(x)$ is the function characterizing the spatial distribution of the flow oscillator and $a(t)$ is the complex amplitude function

$$a(t) = a_0 e^{\gamma t - i\omega t} \tag{2.3}$$

where a_0 is the initial value of $a(t)$. This expression is valid only for a short interval of time after the disruption of the steady flow.

The linearized form of the Landau equation can be derived. With respect to $|a|^2 = a_0^2 e^{2\gamma t}$ it can be written as:

$$\frac{d|a|^2}{dt} = 2\gamma|a|^2. \tag{2.4}$$

Even if the solution to this equation is extremely complicated and the solution for flows such as a flow past a cylinder has not been found yet, we can derive some findings by analyzing this equation.

When $Re<Re_{cr}$ all disturbances are stable with $\gamma<0$. When $Re=Re_{cr}$ just one normal mode takes place ($\gamma=0$), which is marginally stable. When the Re is larger than Re_{cr}, there is only one mode with positive growth rate, $\gamma_1>0$, and all other modes have a negative growth rate ($\gamma_n<0$). As the Reynolds number grows larger these modes also become unstable. This instability can not be described by this linearized form of the Landau equation.

The Landau equation can be extended to include fourth-order terms as:

$$\frac{d|a|^2}{dt} = 2\gamma|a|^2 - \beta|a|^4 \tag{2.5}$$

the solution of this equation is:

$$\frac{1}{|a|^2} = \frac{\beta}{2\gamma} + a_0 e^{-2\gamma t}. \tag{2.6}$$

When $t \to \infty$ then:

$$|a(\infty)|^2 = \frac{2\gamma}{\beta} \tag{2.7}$$

The real part of γ, γ_r, is proportional to the departure from the critical point, $Re\text{-}Re_{cr}$, and the real part of β_r is positive for shear flows and the flow past a bluff body. Since $\gamma_r \sim Re\text{-}Re_{cr}$ it must be from (2.7) that $a(\infty) \sim (Re\text{-}Re_{cr})^{1/2}$.

Based on the analysis of transient records (or impulse response) and measurements of the amplitude and frequency, the variation of the real growth rate with the Reynolds number was determined (Mathis [15], Provansal [13], Sreenivasan 16], Oertel [17]) in the form:

$$\gamma_r = \frac{(Re - Re_{cr})}{5d^2} \tag{2.8}$$

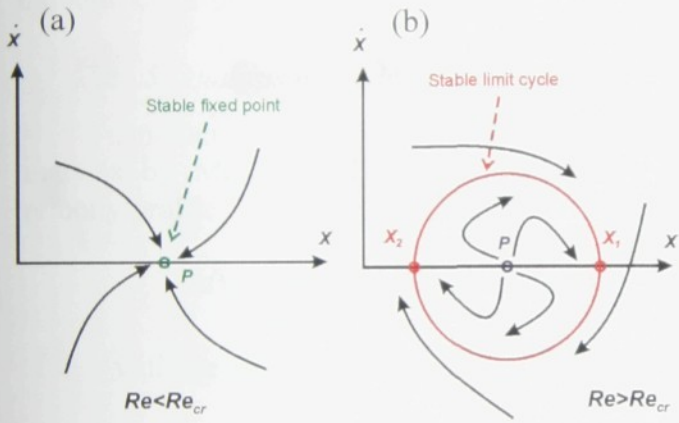

Fig. 2.8 - Bifurcation diagram. Onset of the instability.

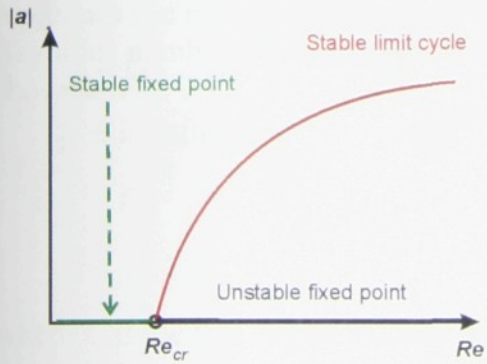

Fig. 2.9. – Increase of the amplitude of fluctuations

2.1.4. Bifurcation[1] theory

The bifurcation system in our case is described by the Landau equation (2.5). The behavior characterized by the Landau equation is called a Hopf bifurcation (in the case of a wake behind a bluff body it is a supercritical bifurcation, see Hourre [12]). It refers to the development of periodic orbits ("self-oscillations") from a stable fixed point, as a parameter crosses a critical value.

A dissipative system is characterized by attractors, toward which neighboring trajectories approach when $t \to \infty$. An attractor can be a fixed point (Fig. 2.8a) representing a stable steady flow or a closed curve, i.e. a limit circle (Fig. 2.8b), representing a stable oscillation.

As Re increases, the flow transits from one steady state to another. In the phase space it is described by a fixed point turning into a limit cycle. In Fig. 2.8b a repeller with spirally outgoing trajectories is shown. It specifies how

[1] A bifurcation occurs when a small smooth change made to the parameter values (the bifurcation parameters) of a system causes a sudden 'qualitative' or topological change in its behavior. (From Wikipedia, the free encyclopedia)

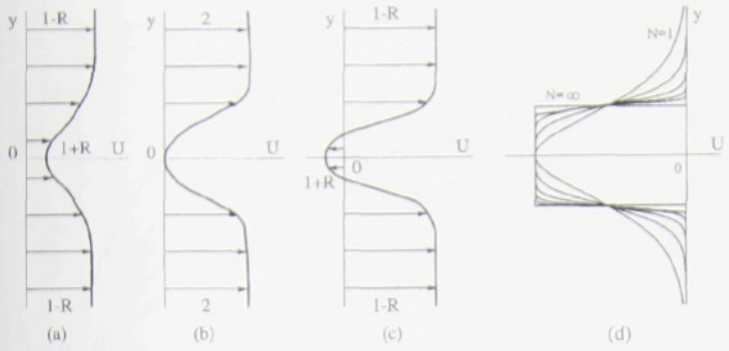

Fig. 2.11- Velocity profiles after (2.10). (a) -1<R<1; (b) R=-1; (c) R<-1; (d)effect of increasing N at R=-1

the steady flow becomes unstable to perturbations. It is obvious in this case how the trajectories are then attracted by a limit cycle, which means that the unstable steady solution leads to a steady oscillation.

In the case of a bluff body the stable steady solution bifurcates to a limit cycle as $Re \rightarrow Re_{cr}$. This phenomenon can also be described, and has been proved by many experiments, in a diagram of a dependent variable $a(X)$ as a function of Re (Fig. 2.9.). At Re_{cr} the solution breaks into two paths. The two values of X in Fig. 2.10 correspond to the maximum and minimum values of amplitude. The size of the limit cycle grows as Re increases.

2.1.5. Analysis of the bluff body wake

Another example of the solution of stability of bluff body wakes is a local analysis by Monkewitz [18]. The mean flow is modeled by the non-dimensional velocity profile

$$U(y;R,N) = 1 - R + 2RU_1(y;N) \tag{2.9}$$

with the shape function

$$U_1(y;N) = \left[1 + \sinh^{2N}\left\{y \sinh^{-1}(1)\right\}\right]^{-1} \tag{2.10}$$

It has been proven that the velocity profiles described by (2.9) faithfully reproduce the measured velocity in the near wake of a circular cylinder in the range of Reynolds numbers Re<48.5 (which is a value of Re_{cr}). The example of such profiles is shown at Fig. 2.11.

R is defined as:

$$R = \frac{U_c - U_\infty}{U_c + U_\infty}, \tag{2.11}$$

where U is the free stream velocity and U_c is the centerline velocity.

The stability of this flow is studied numerically by solving the Orr-Sommerfeld equation for the family of profiles described by (2.9), where the Reynolds number is defined as:

$$\overline{Re} = \frac{\overline{U}\delta}{\nu} \text{ where } \overline{U} = \frac{U_c + U_\infty}{2} \tag{2.12}$$

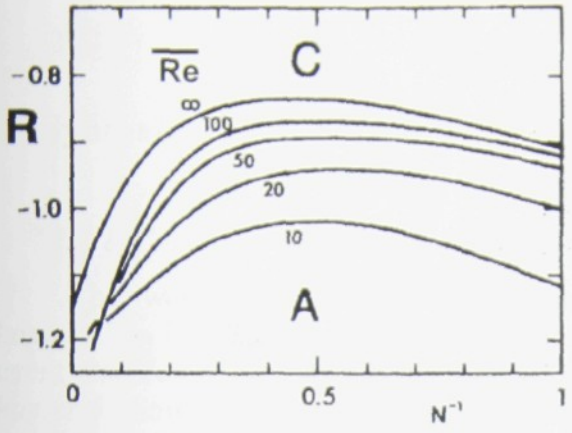

Fig.2.12. Results of stability solution. A-absolutely unstable; C-convectionaly unstable

and δ is a half-wide of the wake. The results are presented in Fig. 2.12.

In the inviscid flow ($Re\rightarrow\infty$) the absolute instability first occurs for a coflowing wake R=-0.85. This means that the velocity profile may undergo a transition to absolute instability, even in the absence of counterflow. The transition is delayed when viscous effects are taken into account. In the case of viscous flows the transition curve is gradually displaced towards the counterflow where R<0.

Important conclusions were derived from this analysis by Monkewitz. In the interval $5<Re<25$ which corresponds to $2<\overline{Re}<10$ the sinuous mode becomes locally convectively unstable in the gradually increasing streamwise domain around $x=d$. In the interval $25<Re<48.5$ which equals $10<\overline{Re}<16$ a pocket of local absolute instability is nucleated around $x=d$, its streamwise extent increasing with $\overline{Re}$ to cover a larger and larger portion of the recirculation bubble. From the local stability point of view, the cylinder wake experiences the following transitional scenario: a locally stable everywhere region of local convective instability, i.e. a region of local absolute instability embedded within a convectively unstable domain.

A number of studies in recent years have shown the importance of three-dimensional phenomena in the wake of nominally two dimensional bodies, mainly circular cylinders, and have pointed out the importance of end effects in creating some of the three-dimensionalities Williamson [8]. Various patterns appear such as oblique vortex shedding Ramberg [19] cells of different frequencies Tritton [20], "chevrons" (Fig. 2.4c) Williamson [10], and vortex dislocations. This phenomenon can not be explained by the theory described above, but by an extended analysis of the Ginzburg-Landau equation.

2.2. Synthetic Jet

2.2.1. Content of the presented papers

The work connected with the research on synthetic jets is presented in *Chapters 5* to *10*. *Chapter 5* contains a detailed description of the topics of the latest and current research as well as the main areas of SJ applications. The article presented in *Chapter 6* shows the results of basic experiments such as determining the operating frequency and time-dependent velocity profiles in crosswise and streamwise directions. The article presents the results from CTA experiments and from "smoke wire" visualization. It also derives the equation for calculating the resonance frequency of the actuator.

Chapter 7 provides the construction of the unique experimental setup and the results from the analysis of the synthetic jet in water. It includes the results of preliminary experiments – identifying the resonance frequency, measuring the time-mean velocity in the streamwise direction, measuring the dependence of the average velocity as a function of time in spatial and time coordinates, and measuring the velocity profiles in the streamwise direction. These results are compared to the results obtained by axisymetric FVM numerical simulation.

The article presented in *Chapter 8* deals with intensification of heat transfer. Four different configurations were studied: the zero-net-mass-flux synthetic jet (SJ), the non-zero-net-mass-flux hybrid synthetic jet (HSJ), the mixed jet (MJ), and the continuous jet (CJ). The article shows the differences in aerodynamic behavior of the SJ, HSJ, MJ and CJ and shows the feasibility of intensifying the heat transfer. The article in *Charter 9* compares the zero-net-mass-flux synthetic jet with the so-called mixed pulsed jet, which is a combination of a continual jet with a synthetic jet. The article also studies the influence of the jet configuration and characteristics on the value of heat transfer. Paragraph 2.2.3 gives a description of the construction of the different types of jets.

Lastly, the article in *Chapter 10* focuses on the dynamics of the actuator. The response of the piezo-ceramic actuator to different driving signals (sinusoidal and square) and to different driving frequencies is studied. It also provides the results of the numerical simulation of the dynamic response of the piezo-ceramic actuator.

2.2.2. Derivation of the resonance frequency

During the working cycle of the actuator the potential energy E_p of the actuator membrane is transformed into the kinetic energy of the fluid E_k in the orifice. The kinetic energy of the fluid in the cavity can be neglected compared to the kinetic energy in the orifice. The whole energy of the fluid can be defined as the sum [21]:

$$E = E_k + E_p . \tag{2.13}$$

When we assume the harmonic oscillations of the membrane the displacement of the membrane is defined as (it is assumed that the loud speaker membrane acts as a piston):

$$z = z_{\max} \sin(\omega t) \tag{2.14}$$

where z_{max} is the amplitude of the membrane and $\omega = 2\pi f$. The velocity of the membrane motion is the derivative of its displacement:

$$\frac{dz}{dt} = \omega \cdot z_{\max} \cos(\omega t) \tag{2.15}$$

When we take into account the mass balance for incompressible flow, the mean velocity of the flow in an orifice of cross section area $A = \frac{\pi d^2}{4}$ can be calculated as:

$$U = \frac{A_m}{A} \omega \cdot z_{\max} \cdot \cos(\omega t), \tag{2.16}$$

where $A_m = \frac{\pi D^2}{4}$ is the area of the membrane with diameter D.

The kinetic energy of the flow is defined as:

$$E_k = \frac{\rho L_e A U^2}{2} \tag{2.17}$$

where L_e is the so-called "equivalent length" and can be calculated as:

$$L_e = L + \frac{8d}{3\pi} \tag{2.18}$$

where L is the length of the orifice with diameter d.
Substituting (2.16) into (2.17) we get the equation for the kinetic energy:

$$E_k = \frac{\rho L_e A \left[\frac{A_m}{A} \omega z_{\max} \cos(\omega t) \right]^2}{2} \tag{2.19}$$

The potential energy of the membrane can be written as:

$$E_p = \frac{1}{2} k_p \cdot A_m \cdot z^2 \tag{2.20}$$

where k_p is the stiffness of the membrane.

The maximum values of the kinetic and potential energies with respect to eq. (2.19) and (2.20)are:

$$E_{k,\max} = \frac{\rho L_e A \left[\frac{A_m}{A} \omega z_{\max} \right]^2}{2} \qquad (2.21.a, b)$$

$$E_{p,\max} = \frac{1}{2} k_p A_m z_{\max}^2$$

Since $E_{k,max}=E_{p,max}$, the value of the resonance frequency can be derived as:

$$f = \frac{1}{2\pi} \frac{d}{D} \sqrt{\frac{k_p}{\rho L_e}} \qquad (2.22)$$

2.2.3. Construction of the different types of jets

Chapters 8 and *9* deal with the problem of intensifying the heat transfer. Four different setups are studied, namely the zero-net-mass-flux synthetic jet (SJ), the non-

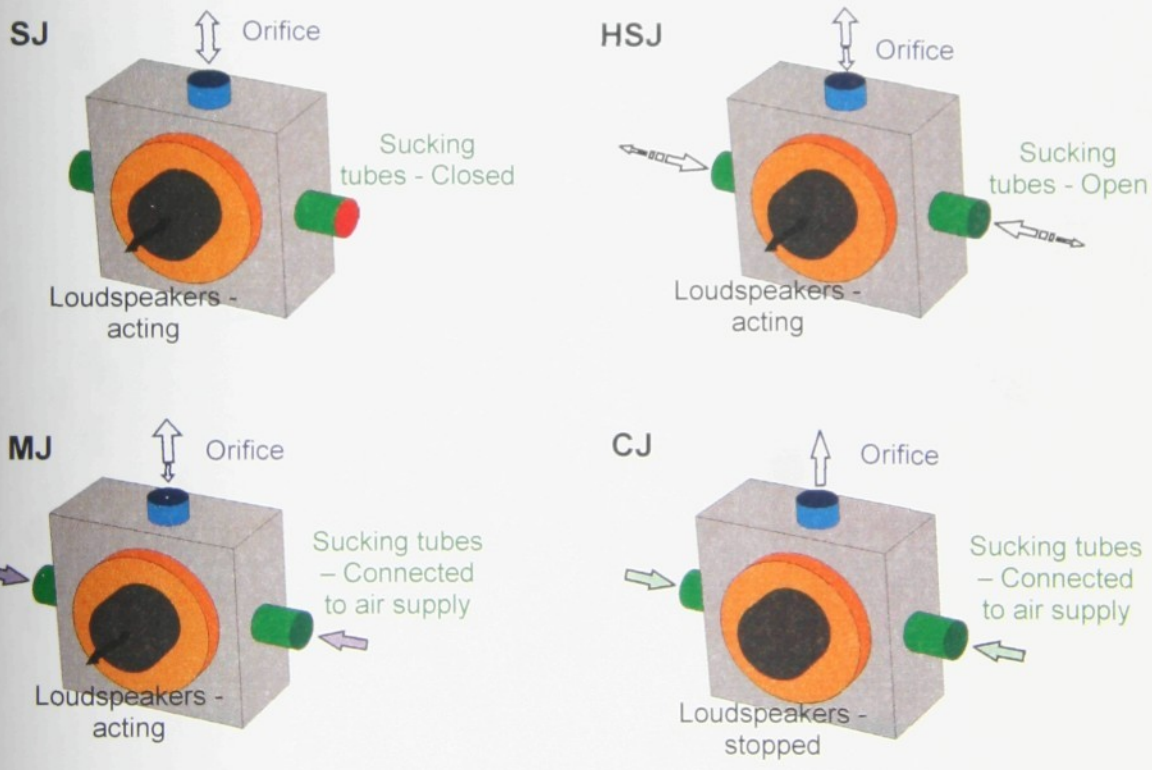

Fig. 2.12. Charts of different setups of actuator.

zero-net-mass-flux hybrid synthetic jet (HSJ), the mixed jet (MJ) and the continuous jet (CJ). The construction of the jets and the principle of functionality are shown in Fig. 2.12. The cavity, the loudspeakers acting as an actuator and the orifice were the same in each setup. Different behavior was provided by opening and closing

the intake tubes in the case of SJ/HSJ, by connecting the intake tubes to the laboratory air supply (MJ), and by shutting out the actuator and connecting the intake tubes to the laboratory air supply (CJ).

CHAPTER 3

EXPERIMENTAL METHODS

This chapter describes the basic experimental methods, such as flow visualization, naphthalene sublimation and hot wire anemometry, used in the research covered by the presented papers.

3.1. Flow Visualization

It is worthwhile using certain visualization techniques at the beginning of the research to get a basic idea of the flow patterns and main flow parameters. The methods of smoke wire visualization and tin ion visualization were used in the presented publications.

3.1.1. Smoke wire visualization (used to visualize the SJ in air)

The smoke wire method was developed by Respet and Moore in the early 1950s (see Yang [22] for details). The basis of this simple but powerful method is a resistively heated thin wire (about 0.15mm in diameter), onto which an oil layer is applied. As the wire is heated by means of electricity, the oil evaporates and the aerosol of condensed oil vapor produced in this way is sufficient to visualize the air flow. Cornell [23] studied the structure of substances used for smoke generation and concluded that the "smoke" does not contain products of combustion but condensed particles approximately 1μm in diameter. This method is suitable for roughly identifying the direction of flow and for identifying large structures in the flow. It is suitable for velocities not exceeding approximately 4m/s. This velocity is limited by the ability to saturate a large amount of air on the one hand and by the magnitude of the critical Reynolds number of the wire on the other hand, so that the von Kármán vortex street behind the wire does not occur.

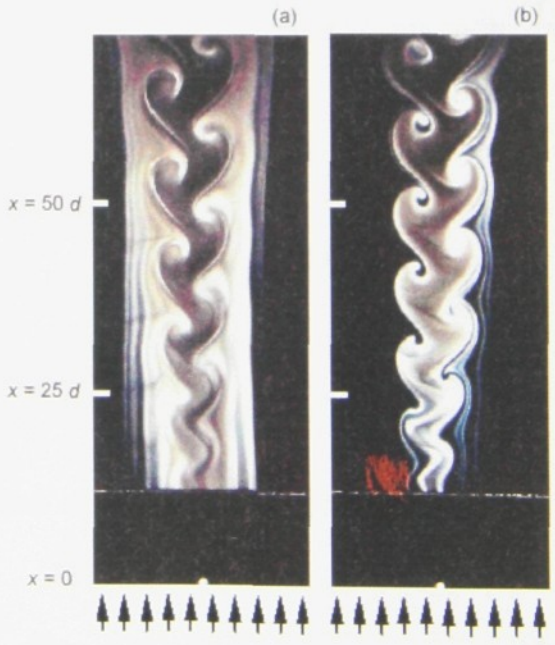

Fig.3.1. Visualization of Kármán vortex street by "Smoke Wire" method at T_∞=144.5°C; Re=61: a/ Isothermal case T*=1; b/ cooled cylinder T*=0.70 (After Travníček[24])

3.1.2. Tin ion visualization (used to visualize the SJ in water and to visualize the von Kármán vortex street)

Visualization by tin ions is one of the "electrolytic precipitation methods" used for flow visualization, described by Honji and Taneda [25]. In this method the test body is coated with a thin layer of solder, or tin wire is used, as the anode. The cathode (in most cases copper) can be placed in any desired position in the flow field. Normal tap water may be used but it is recommended to add salt for better results. When the voltage is applied a cloud of white dye separates from the anode and follows the flow.

The dye is the metallic salt and consists of nearly spherical particles. The particles have a very low sedimentation velocity. This method is sufficient for velocities up to 5cm/s. At higher velocities it is difficult to produce enough dye.

The diameter of the anode must be small enough with respect to the formation of the von Kármán vortex street. Another disadvantage is contamination of the test fluid by tin particles.

3.2. Naphthalene Sublimation Method

Heat transfer coefficients in complex geometries can be determined by mass transfer measurement on similar geometries under similar flow conditions using volatile solids such as naphthalene and utilizing the Reynolds or Chilton-Colburn analogy between heat and mass transfer at low mass flux conditions (see Geankoplis [26]).

The Reynolds analogy can be derived from the momentum and energy equations for negligible pressure gradient and $Pr \sim 1$. It is usually written in the form:

$$Nu = C_f \frac{\mathrm{Re}}{2} \tag{3.1}$$

where we define the Stanton number as

$$St \equiv \frac{Nu}{Re\,\mathrm{Pr}} \tag{3.2}$$

Equation (3.1) transforms (for Pr~1) to:

$$St = \frac{C_f}{2}. \tag{3.3}$$

The Reynolds analogy was expanded on the basis of empirical results to the form:

$$\frac{C_f}{2} = St\,\mathrm{Pr}^{2/3} \equiv j_H \tag{3.4}$$

where j_H is the Colburn factor for heat transfer. The Chilton-Colburn analogy is valid for $0.6<Pr<60$. It is applicable to laminar flows if $dp/dx \sim 0$ and to turbulent flows without restriction on dp/dx.

The amount of mass transfer during a specified time period is determined by weighting the model or measuring the surface recession.

3.3. Hot Wire Anemometry

Although the basis of the HWA method is well-known (for more information see Bruun [27], Perry [28]), we will mention here the basic principle of this method and solutions to certain problems that arise when using HWA to measure velocity in non-isothermal fluid flow and in different media.

3.3.1. HWA principles

The HWA method is based on convective heat transfer from the heated body into the surrounding moving environment. The basic element of the measuring circuit is the probe which, in the simplest case, is in the form of a tungsten wire fixed to the prongs of the carrier. The wire is heated by electric current. We can formulate the heat generated by the electric current in the wire element of length dx according to Joule's law in the form:

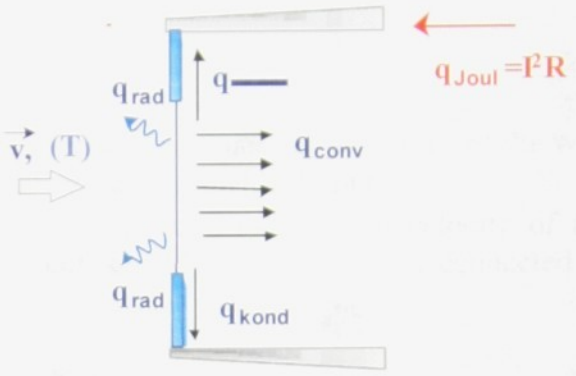

Fig. 3.2. Mechanism of heat transfer from the wire element

$$d\dot{Q}_J = \frac{I^2 \chi_{wire}}{S_{wire}} dx \tag{3.5}$$

In the stationary case, the heat generated in the wire element (Fig.3.2) must equal the sum of the heat transferred into the surroundings, i.e. the convective transferred heat $d\dot{Q}_{conv}$, the heat transferred into the carrier $d\dot{Q}_{cond}$, and the heat radiated into the surroundings $d\dot{Q}_{rad}$. The heat dissipated by means of radiation is in most cases (except for measurements near the wall) negligible and the heat dissipated from the wire into the carrier can be considered as independent of the parameters of the flowing medium. The convective heat transferred into the flowing medium can be formulated according to Newton's law for heat transfer:

$$d\dot{Q}_{conv} = \pi l_{wire} d_{wire} h(T_{wire} - T_{\infty}) \tag{3.6}$$

The transferred heat is then proportional to the fluid velocity and to the temperature difference of the wire T_{wire} and the fluid T_{∞}. This means that HWA can be used for both velocity and temperature measurement. Simultaneously however, a consequence of the above-mentioned dependence is the inaccuracy of the velocity measurement in non-isothermal fluid flow.

If we assume an infinitely long wire where we can ignore heat transfer into the holder, the thermal balance is given by:

$$I^2 R_{wire} = \pi l_{wire} d_{wire} h (T_{wire} - T_\infty) \tag{3.7}$$

If we substitute the relation for temperature dependence of resistance $R_{wire} = R_0 [1 + \alpha_0 (T_{wire} - T_0)]$ and the relation for voltage calculation $E_{wire} = I^2 R_{wire}$, we can rewrite equation (3.7)) in the form

$$E_{wire}^2 = (A + BU^n)(T_{wire} - T_\infty), \tag{3.8}$$

where A, B and n are the functions of wire diameter and material properties of the wire and of the surrounding fluid whose magnitude we get through calibration.

As mentioned above, HWA probes are sensitive to both the velocity of the surrounding fluid and its temperature. Velocity sensitivity of the probe connected in constant temperature (CTA) regime $S_{u,CT}$ can be calculated as follows:

$$S_{U,CT} = \frac{\partial E_{wire}}{\partial U} = \frac{nBU^{n-1}}{2} \left[\frac{R_{wire}(T_{wire} - T_\infty)}{A + BU^n} \right]^{1/2} \tag{3.9}$$

Temperature sensitivity $S_{\Theta, CT}$ can be calculated as:

$$S_{\Theta,CT} = \frac{\partial E_{wire}}{\partial \Theta} = -\frac{1}{2} \left[\frac{(A + BU^n) R_{wire}}{(T_{wire} - T_\infty)} \right]^{1/2} \tag{3.10}$$

There are two regimes of measuring by means of a wire anemometer in practice. All our experiments were carried out in the constant temperature regime.

In the constant temperature (CT) regime of HWA, the temperature of the wire is maintained constant. The wiring of HWA in the CT regime is illustrated in Fig.3.3.

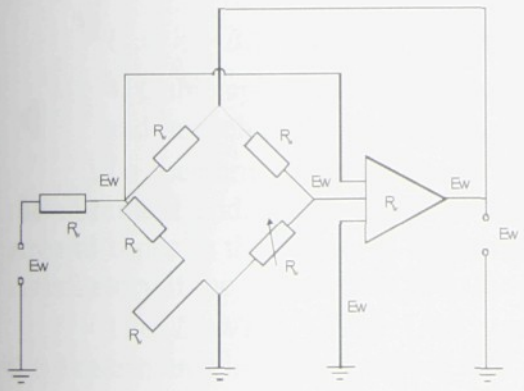

Fig. 3.3 Wheatstone bridge for anemometer operating in CT mode

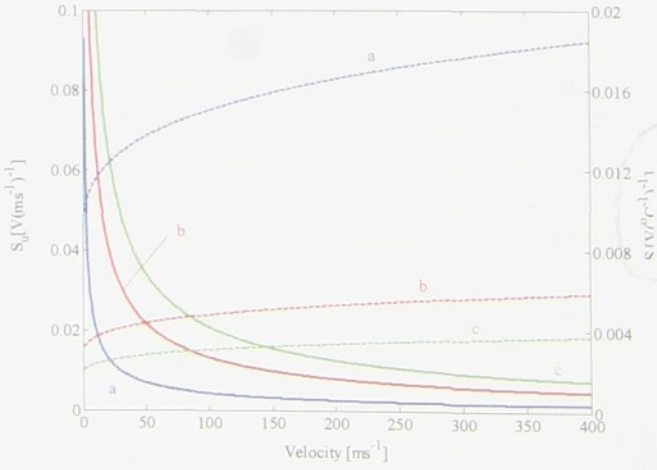

Fig. 3.4 The variation in the velocity (line) and temperature (dotted) sensitivity (for CTA bridge) with velocity for temperature differences T_{wire}-T_a of: a/10K, b/100K, c/250K (After Bruun[27])

The voltage change E_2-E_1, which is proportional to the resistance change of the wire results from the velocity change in the flowing medium. Signal E_2-E_1 is led into an amplifier whose output is current I which is inversely proportional to the wire resistance. Conducting this current back into the bridge results in a repeated adjustment of the initial resistance value of the wire.

An important parameter of the probes under the CTA regime is the so-called *overheat ratio*. The overheat ratio is formulated as follows:

$$a_h = \frac{R_{wire}}{R_a} \tag{3.11}$$

and is a guide for adjusting the wire temperature. From the relations (3.9) and (3.10) it follows that the velocity and temperature sensitivity of the probe is directly dependent on the selection of the overheat ratio. Therefore it is recommended for the velocity measurement to select an overheat ratio as high as possible. Maximum values are limited by the material properties of the wire, especially by a tendency toward faster corrosion at higher temperatures. In experiments performed in water, the overheat ratio is limited by the boiling temperature of the water and by the influence of buoyancy measurements.

3.3.2. Probe calibration

Precise calibration of the probe used is an essential part of each measurement. During calibration the constants shown in the calibration curve $E=f(U)$ for velocity measurement and $E=f(T)$ for temperature measurement are determined. The most common relations for HWA calibration are:

1. The power law (often called King's law) in the form:

$$E^2 = A + BU^n$$

2. The extended power law (see Van der Hegge Zijnen [29]) in the form:

$$E^2 = A + BU^{0.5} + CU$$

3. Polynomial curve fit (see Swaminathal [30]):

$$U = A + BE^2 + C\left(E^2\right)^2 + C\left(E^2\right)^3 \cdots$$

4. Cubic spline fit - the range of measured velocities is divided into n subranges and in each of these subareas a cubic function is fitted using the recorded values.

To perform experiments precisely it is important to calibrate before each measurement and, if necessary, at the end of each measurement, and sometimes also several times in the course of measuring. We can consider the results of experiments as satisfactory if the values from both the initial and final calibrations do not differ.

The *DANTEC Flow Unit* was used to calibrate the probes in air. During the experiments in water a towing tank or calibration by free water jet was used.

3.3.3. Using HWA in water

The HWA methods as described above may be used in water and in other fluids as well. A few aspects must be considered to obtain reliable results:

Fragility: the standard hot wire probes are not robust enough to be used in water. A bigger and more robust hot film probe is used instead.

Electrolysis: Coated hot wire/film probes must be used to overcome problems connected with electrolysis-like formation of bubbles on the wire or by reducing the diameter of the wire. Nowadays a thin quartz coating on hot-film probes is frequently used. The thin protective layer has a negligible effect on frequency response and coated probes can be used for frequencies up to 50 kHz.

Bubble formation on the probe: It is observed that this problem is caused by bubbles suspended in the water. It is recommended to allow the water to stand before use. The effect can be also eliminated by restricting the temperature difference between the film and the water to about 20°C. The corresponding overheat ratio is then about 1.05:1.1.

Cavitation: Cavitation, which is also connected with bubble formation on the wire, may occur at sufficiently high velocities. For a 25μm or 50μm diameter probe it is at about $9ms^{-1}$ or $5ms^{-1}$.

Temperature drift: The temperature difference, T_w-T_∞, for a hot-film probe in water is usually only about 20°C (compared to a typical difference of 250°C in air). The temperature difference that occurs in Eq. (3.8) results in a large shift in the measured velocity, even for a change of a fraction of a degree of water temperature. This problem can be minimized by monitoring the water temperature and then applying a temperature correction (see Bruun [27] for details).

Probe fouling: A gradual build-up of scale, algae and minerals on the probe could cause inaccuracies in reading the velocity. In recirculating test facilities and tanks these problem can be minimized by using de-ionized water, a bypass filtration unit and algae inhibitors.

3.3.4. Phase averaging

Both the Synthetic Jet and Kármán vortex street represent flows where the velocity fluctuations are superposed on the main harmonic velocity. The velocity should be separated into the mean U, harmonic $u(t)$ and fluctuating $u'(t)$ parts Sonnenberger [31]:

$$U(t) = \overline{U} + u(t) + u'(t) \tag{3.12}$$

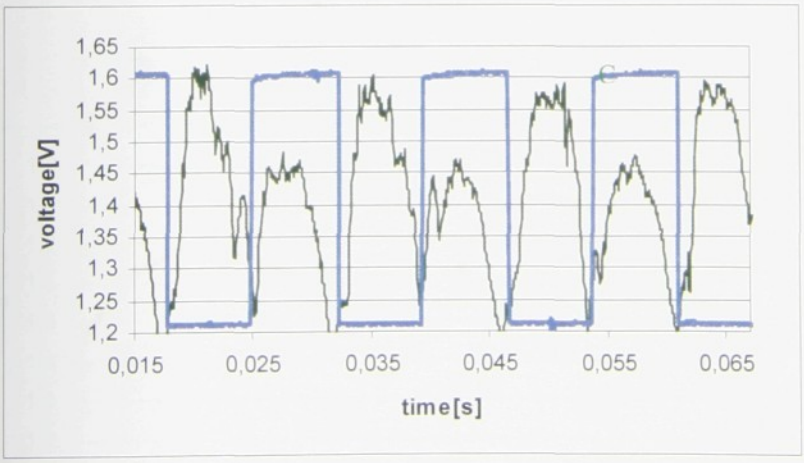

Obr.3.5 Acquired CTA(green) and TTL(blue) signals

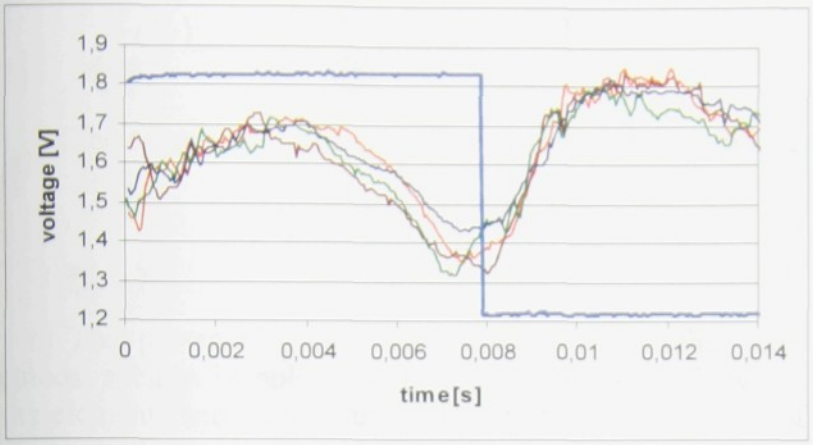

Obr.3.6 Acquired signal devided in individual periods

The mean velocity can be determined as:

$$\overline{U} = \frac{1}{t}\int_{\tau} U(t)d\tau \tag{3.13}$$

However, in many applications it is useful to separate the values of fluctuating velocity from the harmonic and mean part of the velocity. This can be done by so-called phase averaging.

In the phase averaging technique the measured velocity (or voltage) is divided into parts which correspond to individual periods. This can be done with the help of a driving TTL signal from the actuator of the SJ. If the driving signal is missing, which is the case of the flow behind a bluff body, a special procedure (mostly based on FFT analysis) must be used to find the periods $U(t)_{rms}$.

Fig. 3.5 shows a typical record of anemometer voltage and driving TTL signal. With the help of TTL the acquired signal is divided into individual periods (Fig. 3.6). Finally, the mean time dependent velocity $\overline{U}(t) = \overline{U} + u(t)$ and standard deviation in time are derived from the acquired data.

$$\overline{U}(t) = \frac{1}{K}\sum_{K} u(t,K) \tag{3.14}$$

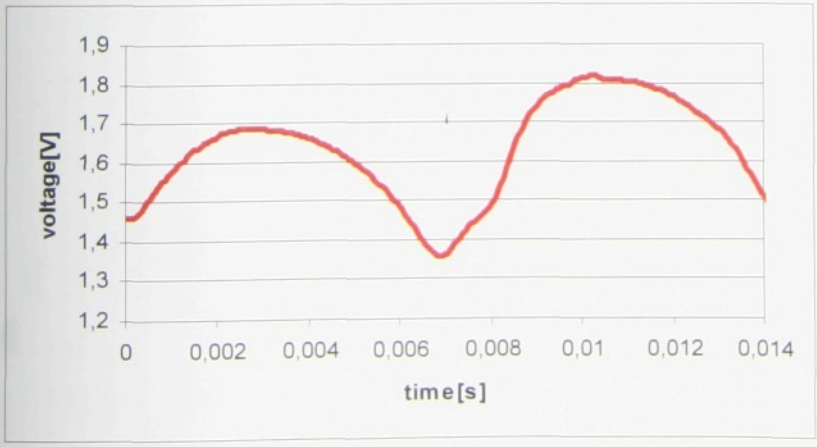

Obr.3.7 Mean time dependent signal

$$U(t)_{rms}^2 = \frac{1}{K-1}\sum_K [u(t,K) - \bar{U}(t)]^2 \tag{3.15}$$

The turbulence intensity at a particular time is defined as:

$$T_i = \frac{U(t)_{rms}}{\bar{U}(t)} \tag{3.16}$$

The presented papers used a number of other experimental and numerical methods, such as Doppler vibrometry, 2D-HWA (see. Fig 1.2), and simulations using finite elements and final volumes. Due to the limited scope of this thesis the details of these methods may be found in the references.

CHAPTER 4

THE INFLUENCE OF TEMPERATURE GRADIENT ON THE STROUHAL-REYNOLDS NUMBER RELATIONSHIP FOR WATER AND AIR

Authors: T. Vít [a], M. Ren [b], Z. Trávníček [c], F. Maršík [c], C.C.M. Rindt [b]

[a] *Faculty of Mechanical Engineering, Technical University in Liberec, Hálkova 6, 461 17 Liberec, Czech Republic*

[b] *Energy Technology Division, Department of Mechanical Engineering, Eindhoven University of Technology, WH-3.127, P.O. Box 513, NL-5600 MB Eindhoven, Netherlands*

[c] *Institute of Thermomechanics, Academy of Sciences of the Czech Republic, Dolejškova 5, 182 00 Prague 8, Czech Republic*

Published in:

EXPERIMENTAL THERMAL AND FLUID SCIENCE, Volume: 31, Issue: 7 Pages: 751-760, Published: JUL 2007, ISSN 0894-1777

Abstract

This paper focuses on the wake flow behind a heated circular cylinder in the laminar vortex shedding regime. The phenomenon of vortex shedding from a bluff body is an interesting scientific and engineering problem. Acquisition of reliable experimental data is considered an indispensable step to deeper physical understanding of the topic.

An experimental study of the wake flow behind a heated cylinder in the forced convection regime is performed using water as the working fluid. Firstly, qualitative visualization experiments have been performed, and the parallel vortex shedding mode was adjusted. Sequentially, hot-wire anemometry was used for *St-Re* data acquisition. Data analysis confirmed the so called thermal effect in water: cylinder heating increases the vortex shedding frequency and destabilizes the wake flow. Further, the effective temperature concept has been used and the *St-Re* data have been successfully transformed to the $St\text{-}Re_{eff}$ curve. The formula for evaluation of the effective temperature in water has been experimentally derived by this transformation.

Finally, a comparison with air as the working fluid is discussed. All the data (from the present experiments in water and known data for air) have been compared with the thermodynamic *St-Re* equation derived by Maršík *et al.*[1] and a satisfactory agreement has been observed.

1. Introduction

Fluid flow around a heated bluff body, namely a circular cylinder, is of principal importance for fluid dynamics as well as for heat transfer (see, e.g., Schlichting & Gersten K, 2000[2]; Incropera, 1996[3]). The low Reynolds number range, when laminar vortex shedding occurs, is considered very important from a scientific as well as an engineering point of view. The phenomenon of vortex shedding from a bluff body has been studied by many authors – e.g. hundreds of references can be found in the comprehensive monograph by Zdravkovich 1997[4]. This phenomenon is of fundamental importance in the theoretical study of hydrodynamic instability which includes many problems dealing with wake flow dynamics (e.g., Monkewitz *et al.*, 1996[5]), such as the onset of vortex shedding, the passing frequency of vortices, and the influence of geometrical and material parameters. From the engineering point of view, the phenomenon of vortex shedding is considered as one of the sources of flow-induced vibrations, noise, or even body collapse. It influences drag as well as heat transfer in an external flow.

This paper focuses on the wake flow behind a heated bluff body, namely a circular cylinder in the laminar vortex shedding regime. It is known that the temperature can be treated as a passive scalar contaminant only if (1) the heating rate is relatively low and if (2) the wake flow is far from any instability (Mi & Antonia, 1994[6]). However, in many other cases the structure of the near wake can be controlled by means of thermal effects.

1.1. Thermal effects in air and water for forced convection

The forced convection regime occurs at a low level of heating. The working fluid properties such as viscosity, density and thermal conductivity are fundamentally important for the thermal effects. In the text below two of the most common working fluids such as air and water are discussed.

In air, a heat input stabilizes the wake flow, thus laminar vortex shedding can be completely suppressed by heating the cylinder. The onset of vortex shedding (the lower limit of the vortex shedding regime) for an unheated cylinder has been studied many times. Commonly accepted critical Reynolds number ($Re = d\ U/\nu$, where d is the diameter of the cylinder, U the velocity of the undisturbed flow and ν the kinematic viscosity at the temperature of the undisturbed flow) ranges from 40 to 49 (e.g., Re_c = 40 by Kovasznay, 1949[7]; 44 by Collis & Williams, 1959[8]; 45.9 by Lange *et al.*, 1998[9]; 47 by Fey *et al.*, 1998[10]; 49 by Williamson, 1996[11]). Cylinder heating suppresses this onset of instability, thus the Re_c value increases with heating. This increase was evaluated in the range of Re_c = 47.7 to 70, if the cylinder temperature increases to nearly 290°C, Wang *et al.*, 2000[12]. A possible explanation for this thermal effect in air is the increase of the kinematic air viscosity with temperature, which causes a decrease of the local Reynolds number. Another known explanation of the thermal effect in air emphasizes a reduction of fluid density by a temperature increase, thus a reduction of absolute instability (Yu, Monkewitz, 1990[13]). Another approach, based on the analytical description of the variable properties of fluids, was suggested by Herwig & Wickern, 1986[14].

If the idea of the so called *effective temperature* is applied, the onset of vortex shedding even for a heated cylinder case can be described by the critical effective

Reynolds number $Re_{c,eff}$, which is the same for both heated and unheated cylinder cases. A value of $Re_{c,eff} = 47.5 \pm 0.7$ was evaluated by Wang *et al.*, 2000[12].

The idea of the effective temperature was proposed originally by Lecordier *et al.*, 1991[15], and used later by Dumouchel *et al.*, 1998[16], who worked out this concept and calculated the effective kinematic viscosity ν_{eff} from an effective temperature T_{eff} that is defined by

$$\frac{T_{eff}}{T_\infty} = 1 + c\frac{T_w - T_\infty}{T_\infty}, \tag{1}$$

where T_∞ and T_w are the free-stream and cylinder surface temperatures, respectively. Recently, the effective temperature was evaluated by Wang *et al.*, 2000[12] in the following form

$$T_{eff} = T_\infty + 0.28(T_w - T_\infty). \tag{2}$$

A recent numerical study by Shi, Gerlach and Durst, 2004[17] concluded that the effective temperature defined by Eq. (2)[12] agrees well with their results[17]. It is obvious that a quite opposite situation occurs in water, where the kinematic viscosity decreases with temperature. Therefore, cylinder heating destabilizes the wake flow in water. This was confirmed experimentally by Lecordier *et al.*, 2000[17]. However, a lack of adequate experimental data for quantitative confirmation (or adaptation) of the T_{eff} - concept at different fluids than air is evident.

It is worth mentioning that the effective temperature is not "only an artificial value", like the well known film temperature, (which is defined as the arithmetic mean of the wall and free-stream temperatures, $T_\infty + 0.5(T_w - T_\infty)$. The effective temperature is close to the hot recirculation zone temperature according to Dumouchel *et al.*, 1998[16], and the maximum temperature in the wake measured by Yahagi, 1998[19] has been apparently very close to the effective temperature, according to the evaluation by Wang *et al.*, 2000[12]. However, no consistent and reliable experimental confirmation of this idea has been published in available literature so far, a fact that is one of the main motivations of this study.

The dynamics of the wake behind a bluff-body is commonly quantified by means of the Strouhal number (*St*, denoting a non-dimensional frequency: $St = d f/U$, where f is the flow frequency). For the *St-Re* relation of the isothermal case, several equations have been presented in the literature, e.g., Roshko, 1954[20], Williamson, 1989[21], and Fey *et al.*, 1998[10]. The influence of heating on the frequency of vortex shedding was studied recently in air, and it was concluded that vortex shedding frequency decreased with increasing cylinder temperature. This frequency decrease was quantified by means of the effective temperature concept. When Re_{eff} is evaluated at T_{eff} defined above in Eq.(2), the derived relationship St–Re_{eff} was found to be "universal", i.e. valid for both heated and unheated cylinder cases (Wang *et al.*, 2000[12]):

$$St = 0.2660 - \frac{1.0160}{\sqrt{\mathrm{Re}_{eff}}} \tag{3}$$

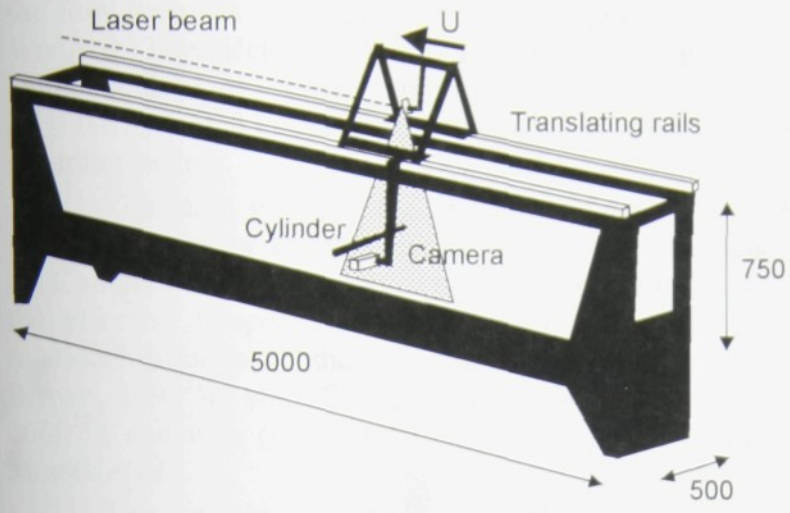

Fig. 1 – Towing tank

A recent numerical study by Shi, Gerlach and Durst, 2004[17] uses the results of Wang *et al.*, 2000[12] as the reference experimental data for the heated cylinders. Shi, Gerlach and Durst, 2004[17] concluded that the experimental data[12] agree well with the numerical results[17, 22], and that their numerical results[17] confirm the experimental finding of the effective temperature (Eq. (2)[12]).

It can be presumed now, that this (or a similar) relation is valid for the vortex shedding in water as well, where the cylinder heating (logically) increases the frequency of the shedding of vortices. However, no studies have focused on this problem.

It is worth noting that a precise evaluation of the *St-Re* curve is intrinsically complicated if the wake is under the influence of the so-called end effects caused by the end conditions of the tested cylinder. Under these circumstances, the vortex shedding from the cylinder is not parallel but slanted to the cylinder axis, and typical discontinuities in the *St-Re* curve exist (Williamson, 1996[11]). There are a few different end-manipulating methods to isolate the end effects and generate parallel vortex shedding. They have been shown by Williamson, 1989[21]; Eisenlohr & Eckelmann, 1989[23]; Miller & Williamson, 1994[24]; Hammache & Gharib, 1991[25] and Wang *et al.*, 2000[12] to be very effective.

1.2. Thermal effects for mixed convection

The forced convection regime occurs at a low level of heating. On the contrary, at a higher level of heating buoyancy effects are added to the viscous phenomena and a mixed convection flow occurs. The vortex shedding frequency can be basically altered. Typically, the Strouhal number increases with the Grashof number. However, the vortex shedding can also be suppressed, which is denoted as a "breakdown of the von Kármán vortex street" (Michaux-Leblond & Bélorgey, 1997[26]; Chang & Sa, 1990[27]). For not too high heat inputs the vortex street can be deflected (Kieft *et al.*, 1999[28]), and the 2D wake flow can be turned into 3D structure (Maas *et al.*, 2003[29]). Of course, all these mixed convection effects depend on the Grashof and Reynolds numbers (*Gr* and *Re* respectively), as well as on the orientation of the free stream with respect to the buoyancy force (buoyancy effects can be opposite or parallel or cross to the free stream). Different criteria for the mixed convection region to occur are suggested in the literature, all based on the ratio Gr/Re^s. A typical used value of the exponent s is within the range of 1.8 to 3. The value $s = 2$ is very common when the ratio of the Gr/Re^2 is called the Richardson number, *Ri*. The criterion for mixed convection to occur in the cross flow situation is $Ri > 0.5$, as used by Wang *et al.*, 2000[12] and by Wang & Trávníček, 2001[30]. Maas *et al.*, 2003[29] found that for water at $Ri = 0.3$

the flow becomes 3D. Other criteria are mentioned by Dumouchel *et al.*, 1998[16] and by Wang & Trávníček, 2001[30]. In fact, the maximum Ri value in the experiments by Dumouchel *et al.*, 1998[16] and by Wang *et al.*, 2000[12] were much lower, around $Ri \leq 0.012$ and 0.02, respectively, to avoid mixed convection in the laminar vortex shedding regime.

The main goals of the present study are: (1) Experimental identification and qualification of the thermal effects in water on the Reynolds-Strouhal number relation. (2) Comparison of the observed results for water to the results for air. (3) Verification of the effective temperature conception by means of comparisons with (a) the *St-Re* relationship for the isothermal case (e.g., the relationship proposed by Williamson and Brown, 1998[31]) and $St\text{-}Re_{eff}$ relationship for the non-isothermal case (Wang *et al.*, 2000[12]), and with (b) the relation derived theoretically from wake flow dynamics by Maršík *et al.*[1].

The measuring methods of and the experimental setup used to define the *St-Re* relation for water are briefly described in the following chapter. The construction of the towing tank and of the heated cylinder are described too. Possible sources of errors and inaccuracies of non-isothermal flow in water are also described here. One paragraph deals with the problems of parallel vs. oblique vortex shedding. The results of the experiments are presented in chapter 3. These results are used here to prove (a) the conception of the "effective temperature", and (b) the theoretical derivation by Maršík *et al.*[1].

2. The Experimental Facilities and Techniques

The experiments were carried out in a towing tank installed at Eindhoven Technical University (a detailed description of the structure is given by Kieft, 2000[32]). Main sizes and arrangement of the towing tank are schematically shown in Fig. 1. A towing mechanism enables movement of the cylinder with a speed range 0÷2cm/s through the tank which corresponds to a Reynolds number interval $Re = 0 \div 90$ with the use of a cylinder with diameter $d = 4.5$mm. The heated cylinder was designed from a copper tube with an external diameter $d = 4.5$mm, as is schematically shown in Figs. 2, 3. The cylinder was equipped with end cylinders from Plexiglas with a diameter of 10 mm on both ends. The cylinder together with the end cylinders were attached between the end plates (detail in Fig. 2) that are tightly mounted to the solid frame of the towing device. The presence of end cylinders and end plates, as were proposed by Eisenlohr & Eckelmann, 1989[23] (where the diameter of end cylinders is recommended in the range of $D = 1.8 \div 2.2d$ and the length of end cylinders should be at least $l = 5d$) should ensure parallel vortex shedding during the experiment. The free length of the cylinder between these both end

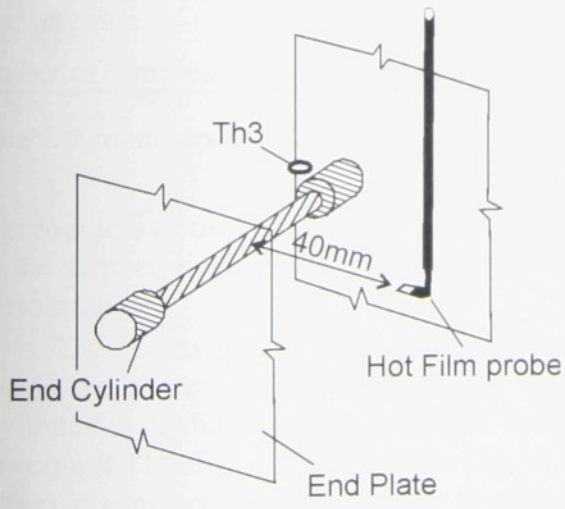

Fig. 2 – Construction of the end cylinders and the end plates. Position of the thermocouple Th. 3.

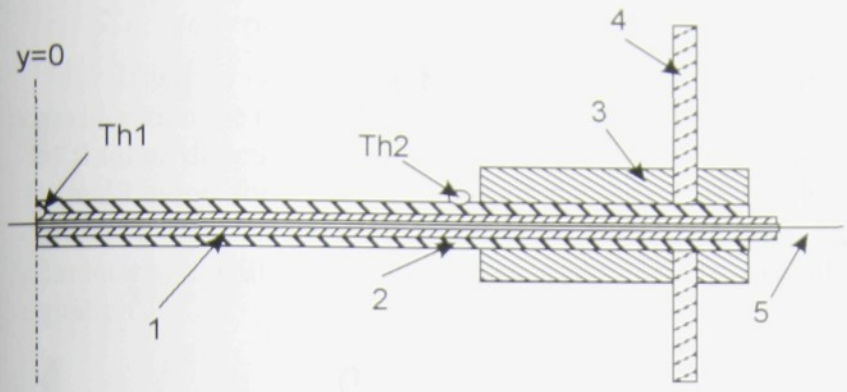

Fig. 3 – Construction of the heated cylinder and positions of the thermocouples Th. 1 and Th. 2; 1, ceramic capillary; 2, copper cylinder; 3, end cylinder; 4, end plate; 5, to the power supply.

cylinders was l=250 mm (this corresponds to the aspect ratio $\lambda = l/d = 56$).

The constr uction of the heating element is depicted in Fig. 3. Heating is provided by a manganin resistance wire with a length of 250 mm and an electric resistance of 21Ω, which is placed in a ceramic capillary. When the electrical load is as high as possible it can produce approximately 80W. This is sufficient enough to overheat the surface of the cylinder with more than ΔT = 5K in slowly moving water; the range of the temperature differences ΔT was from 0 to 2.8K for all experiments.

The experiments carried out in the water are very sensitive to the temperature of the liquid. That's why special attention was dedicated to precise measuring of this temperature during the experiments. The form of heating of the cylinder corresponds to a boundary condition of constant heat flux, and that's why it was necessary to carry out a temperature calibration before the actual experiment started. That means that we had to define the characteristic: $\Delta T = T_w - T_\infty = f(Re, I)$, where I is the value of amperage through the resistant wire. To measure the temperature on significant places, Alumel–Chromel thermocouples with diameter 0.076 mm were used. The first thermocouple to measure the temperature inside the cylinder was placed between the copper tube and the ceramic capillary (Th. 1 in Fig 3). This thermocouple was used to define a steady state of the system. Experiments started only after the temperature on this thermocouple settled on a constant value. The second thermocouple

Overheat ratio	0.12	-
Over temperature	40	°C
Offset	2.766	-
LP filter	0.3	kHz
Sampling rate	0.05	kHz
Number of samples	8192	-

Table 1. Parameters of CTA bridge

(Th. 2) was placed on the cylinder surface. During the calibration, Th. 2 was placed in the center of the cylinder span; after that Th. 2 was replaced at the end of the cylinder to avoid wake disturbances during experiments (see Fig. 3).. The third thermocouple (Th. 3 in Fig 2) has been placed 30mm in front of the cylinder to measure the free stream temperature T_∞. It is possible to presume that relative error in the temperature measuring didn't exceed 1%.

2.1. Temperature calibration

If we do not take the heat flow to the end desks and to the end cylinders into consideration we can consider the value of heat flow from the surface of the cylinder to the fluid as directly proportional to the current flow through the resistant wire. During the calibration for a known value of the Reynolds number and a selected value of current I, the temperature difference $\Delta T = T_w - T_\infty$ was measured. The calibration characteristic will be deduced from the following overall convective heat transfer equation:

$$Q = \alpha A \Delta T , \tag{4}$$

where α is the mean heat transfer coefficient and A is the overall surface of the exposed body.

The heat transfer for forced convection *for a moderate temperature loading* can be expressed by the following non-dimensional form:

$$Nu = (\mathrm{A} + \mathrm{c}\, Re^{\mathrm{n}})\, Pr^{\mathrm{m}}, \tag{5}$$

where Nu is the Nusselt number ($Nu = \alpha d/\lambda$), Pr is the Prandtl number, λ is the kinematic viscosity, and A, c, n, m are experimentally determined constants.

Evidently, heat transfer varies predominantly with the Reynolds and Prandtl numbers and many other parameters affect the process such as temperature loading, boundary conditions, aspect ratio (end effects), blockage effects due to the wind tunnel and wakes, and free-stream turbulence. It is worth noting here that the overall heat transfer in general form should include the so called temperature loading factor – see, e.g. discussion by Wang & Trávníček, 2001[30]. However, as the temperature differences in the present experiments are relatively small, the so called temperature loading factor is neglected in Eq.(4).

The material properties of water (heat conductivity, kinematic viscosity and Prandtl number) as function of temperature can be expressed in the following forms:

$$\lambda = \lambda_0 \left(\frac{T}{T_0}\right)^{\varpi 1} \qquad \nu = \nu_0 \left(\frac{T}{T_0}\right)^{\varpi 2} \qquad Pr = Pr_0 \left(\frac{T}{T_0}\right)^{\varpi 3} \tag{6}$$

where T_0 is the reference temperature, $T_\infty \le T_0 \le T_w$.

Taking into account Eqs. (4 and 5), the Ohm's law (which gives $Q = RI^2$, where R is the resistance), and presuming that $A \ll cRe^n$ in Eq.(5) (in the investigated Re - range), the calibration function can be expressed as

$$I = [(1/R)(\lambda/d) c Re^n Pr^m A(T_w - T_\infty)]^{1/2}. \tag{7}$$

For the specific resistance of the wire used (R), the cylinder used (d, A), the use of water as the working fluid (Pr, λ), and postulating that Eq.(5) is valid for material properties Pr, λ matching T_∞ (this postulate is possible for the present relatively small temperature differences in water), Eqs. (6 and 7) yield:

$$I = CRe^{n/2}(T_\infty/T_0)^{\Omega}(T_w - T_\infty)^{1/2}, \quad (8)$$

where $\Omega = (\omega 1 + m\ \omega 3)$.

The purpose of the calibration was to find the values for the constants C, Ω, m, and n so that function (8) would correspond to values measured during the calibration.

For selected values of Re and ΔT, the value of heater current I was set before each experiment. Real temperature values $T_{\infty,r}(t)$ and $T_{w,r}(t)$ were measured during the experiment. The mean value of the actual temperature difference $\Delta T_r = \frac{1}{t}\int (T_{w,r} - T_{\infty,r})dt$ was calculated from these temperatures. Consecutively, the error of measuring $\varepsilon = \Delta T - \Delta T_r$ was evaluated. If this error was smaller than 0.1K the results were used for further processing.

The aim of the experiment was to carry out measurements in the forced convection range. The value of the Richardson number didn't exceed the value of $Ri = 0.15$ ($Re_\infty = 56.3$, $Gr = 483.53$). According to Wang *et al.*, 2000[12] the influence of buoyancy effects can then be considered as minor.

Two experimental methods have been used to identify the velocity field behind the heated cylinder.

2.2. Visualization

Ions of tin were used for visualization. A tin wire (actually four wires formed into a grid) with diameter 0.6mm was used as an anode. More information about the method can be found in Maas *et al.*, 2003[29]. It was noticed during the experiments that the grid formed by the wires as well as the tin wire itself influence the results of the experiments too much and that it led to a decrease of the frequency of vortex shedding. That is why the results of the visualization were used only to study the structure of the flow, mainly to show the parallelism of vortex shedding. The frequency results extracted from the visualization experiments were not taken into consideration in the final results.

2.3. Frequency measurement using CTA

Even though there were problems mainly due to the low velocity of the water flow (approx. 10-20mm/sec) and transfiguration of the velocity field (parallel versus oblique vortex shedding), the Constant Temperature Anemometer (CTA) with a film probe proved suitable to find *St-Re* dependence correctly even for the non-isothermal flow.

A "hot film" probe (type P55R36), and StreamWare system together with the software StreamLine produced by DANTEC were used to perform experiments. The parameters of the CTA circuit were adjusted as shown in Table 1. The probe was placed in the axis of the cylinder at a downstream distance of 40–50mm during the experiments as shown in Fig. 2.

Even though the perfect acquirement of the velocity is not important for the present study on the *St-Re* relationship, the calibration $E = E(U)$ was carried out. The probe was fixed to the towing appliance and it was towed with known velocity through the tank. Fig. 5 shows typical time line record of the voltage over the CTA Bridge.

2.4. Discussion of experimental uncertainties

Before we evaluate the results it is necessary to point out several errors that were made while using CTA, and possible solutions to eliminate them. It is necessary to evaluate the time line record of the development of the velocity field with regard to the following factors.

2.4.1. Parallel vortex shedding

It is a well known fact that vortex shedding from a circular cylinder is influenced by the so called end effects, which are related with transition to oblique vortex shedding modes, thus with discontinuities in the *St-Re* relationship (Williamson, 1989[21], Eisenlohr & Eckelmann, 1989[23]). Parallel vortex shedding is related to the continuous *St-Re* curve.

Initially, after the start of the cylinder motion in the towing tank, the shedding pattern is parallel. However, if the end effects change the mode of shedding at the cylinder ends, these changes diffuse over the whole cylinder span. This time development is demonstrated in Figs. 4 and 5.

Fig. 5 demonstrates a response of the parallel and nonparallel vortex shedding.

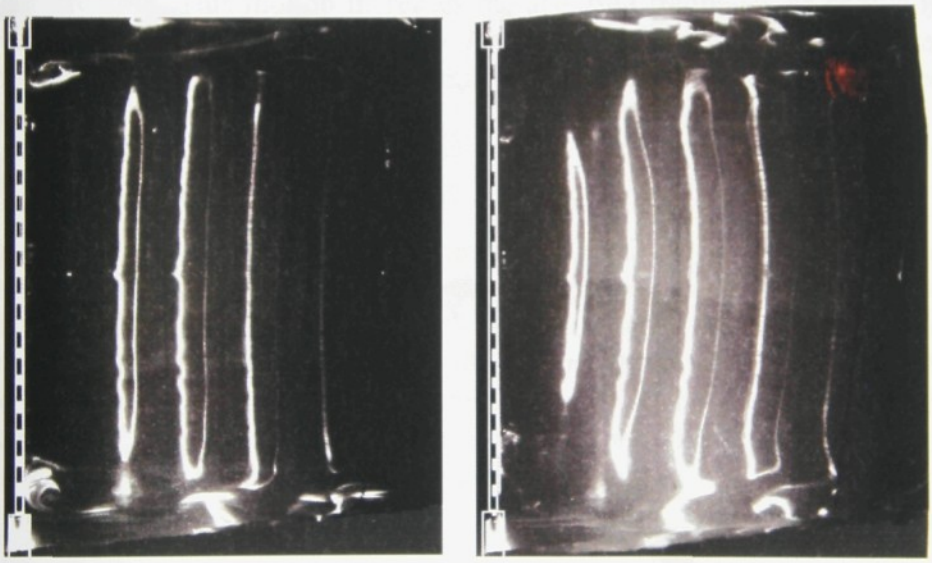

a) b)

Fig. 4 – Parallel and oblique regimes of vortex shedding at Re = 70, ΔT = 1.4 K. Pictures past (a) 7s i.e. 25*d* and (b) 63s i.e. 225*d* from the beginning of the experiment.

The nonparallel (oblique) vortex shedding is characterized by the decrease of recorded frequency on the time line record. The distortion of the vortex street always appeared after a certain period during the experiments and the regime of shedding was no longer possible to be considered parallel.

The results of the flow field visualization showed parallel vortex shedding along almost the whole length of the cylinder for different temperatures of the wall – see Fig. 4. The effect of the end cylinders is clearly visible behind them. If the movement of the cylinder lasts longer the influence of the end effects appears and the flow is no longer parallel. To make a comparison, Fig. 4 shows the velocity field after the cylinder was moved $25d$ and $225d$ from the beginning of the experiment.

Parallel vortex shedding was confirmed on the base of visualization (an example is shown in Fig. 4) and only the data obtained under the parallel vortex shedding were collected for evaluation. Parallel vortex shedding was also proved in the spanwise direction by CTA measuring. Typical results of CTA and visualization, obtained at the same parameters, are shown in Fig. 7. This demonstrates that the frequency along the span was practically constant except in the vicinity of the cylinder end ($y = 100$ mm), where a decrease of the frequency has been found. This end-effect agrees very well with a spanwise measurement of the vortex shedding frequency, which is known from literature (e.g., Williamson, 1996[11]; König, Eisenlohr, and Eckelmann, 1990[33]).

2.4.2. "Motion" of wake due to the large structures in the tank

The presence of the large structures in the tank leads to a motion of the wake in the vertical direction. This motion increases the acquired frequency as shown in Fig. 6. This effect has the biggest influence at low *Re* numbers. The presence of the secondary flow is the most important reason for difficult detection of the critical *Re* number in the towing tank.

2.4.3. Disturbances in the towing tank

In comparison with similar experiments carried out in air, several problems complicate the experiments in water. Obviously, precise measurements require well stabilized flow and temperature fields in the standing water of the towing tank. Fluid flow in the tank is practically stabilized after a long time when the experiment was carried out – it was necessary to wait approximately for two hours between experiments. On the other hand, large eddy structures are formed during this time which undermines the experiments (this effect complicates an evaluation of the frequency – see the

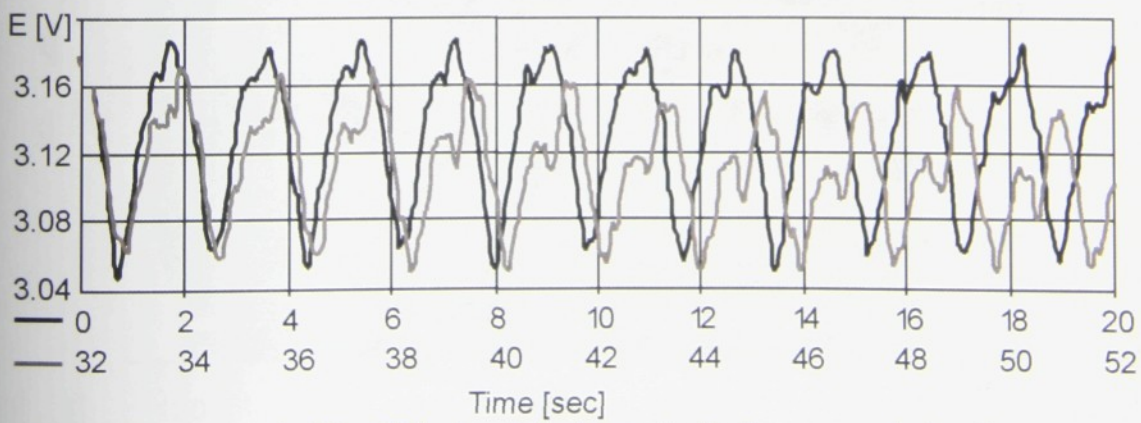

Fig. 5 – Time record of the CTA signal. A change in the frequency during the experiment results from the change from the parallel to oblique modes of vortex shedding. Recorded at $Re = 71$, $\Delta T = 0$, at the beginning (0-20 s – black line) and at the end (32-52 s – grey line) of the experiment.

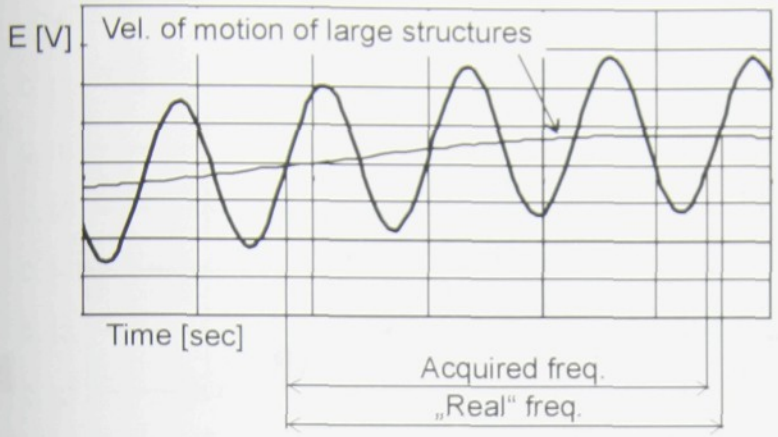

Fig. 6 – Error due to the motion of the large structures

previous paragraph 2).

Another significant complication which has to be mentioned is a non-uniformity of the temperature field. To avoid this non-uniformity, the tank was filled up at least one day before the experiment to ensure an equalization of the water temperature with the laboratory temperature. However, the temperature uniformity cannot be ideal – residual thermal drifts, which are partly connected with the large eddy structures and partly with a natural thermal stratification, remain permanently. A maximum difference between the highest and the lowest temperature of the water in the tank during one experiment of $T_{\infty,max}$-$T_{\infty,min}$ = 0.2K was measured during the experiments. Inaccuracies caused by the non-uniformity of the temperature field influence the experimental results by changing the thermo-physical quantities of the fluid. It is good to point out that in contrast with air (with relatively weak temperature dependencies of the thermo physical properties) the differences in the kinematic viscosity of water are much bigger. For example, a rather small temperature increase 1K from 290K to 291K decreases the kinematic viscosity by 2.5%.

Taking into account all these experimental difficulties, the uncertainty of the *St* number based on the CTA measurement was estimated within 1% (this deviation is shown in Fig. 9).

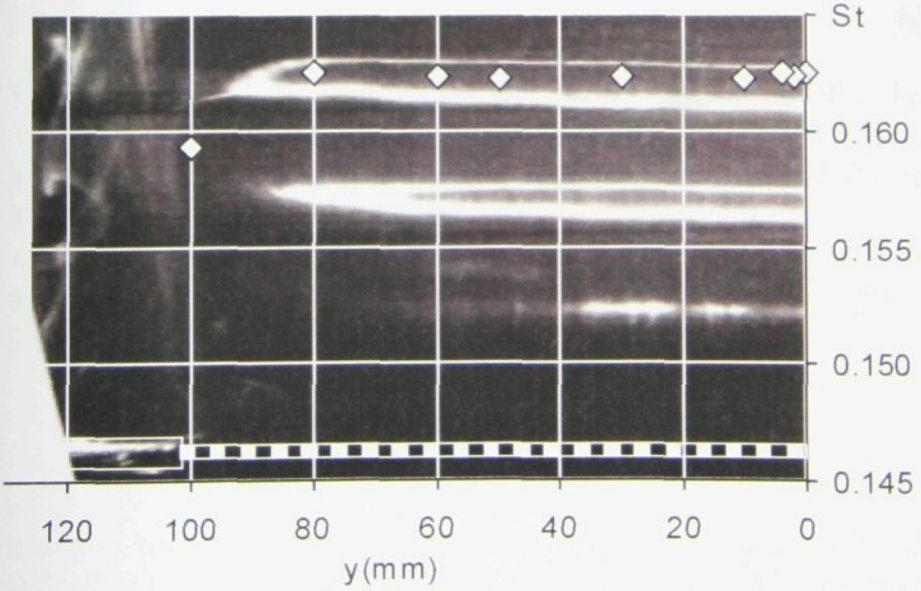

Fig. 7 – Variation of *St* in lengthwise direction; *Re* = 87; T_w/T_∞ = 1.0072. Corresponding visualization is shown on the background; flow is oriented bottom-up.

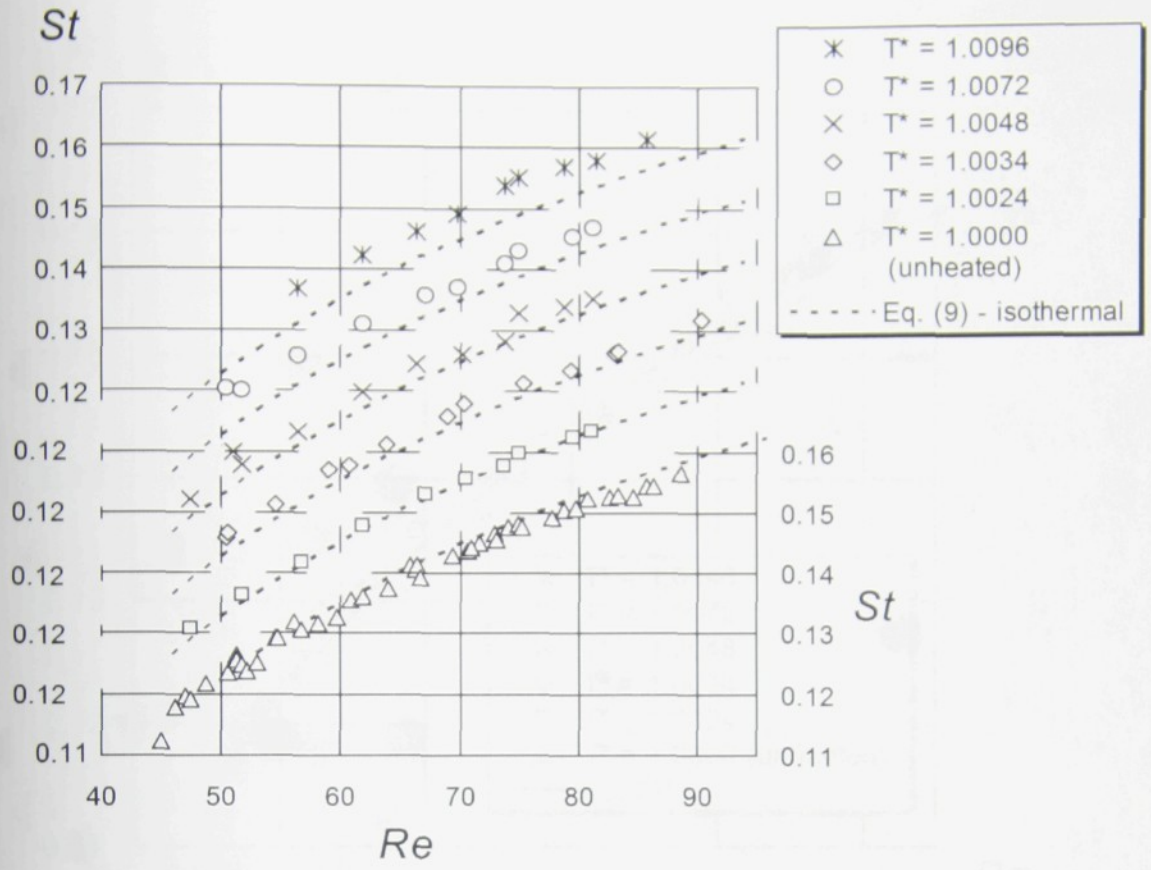

Fig. 8 –The St-Re relationship of the unheated and heated cylinder in the water flow. Comparison of the measured data (points) with the reference unheated cylinder by Eq.(9) – Williamson and Brown, 1998[31].

3. The Results

3.1. St-Re relationship

Fig. 8 presents an example of results: *St-Re* relationships for the unheated cylinder ($T_w/T_\infty = 1.0000$) and for several heated cylinders ($T_w/T_\infty = 1.0024$ to 1.0096). The scale on the vertical axis is shifted by $St = 0.01$ for each of the temperature differences to make the chart well-arranged.

For comparison purposes, the curve corresponding to the unheated cylinder according to Williamson and Brown, 1998[31] is drawn to each of the data series. This curve is considered the reference one for the isothermal case; its form is[31]

$$St = 0.2665 - \frac{1.0175}{\sqrt{Re}}. \qquad (9)$$

It is noteworthy here that the "universal" (i.e. valid for both heated and unheated cylinders) St–Re_{eff} relationship defined by Eq.(3)[12] gives practically the same results in the isothermal case where $Re_{eff} = Re$ and the maximum deviation of Eqs.(3 and 9) is less than 0.23% – see Wang *et al.*, 2000[12].

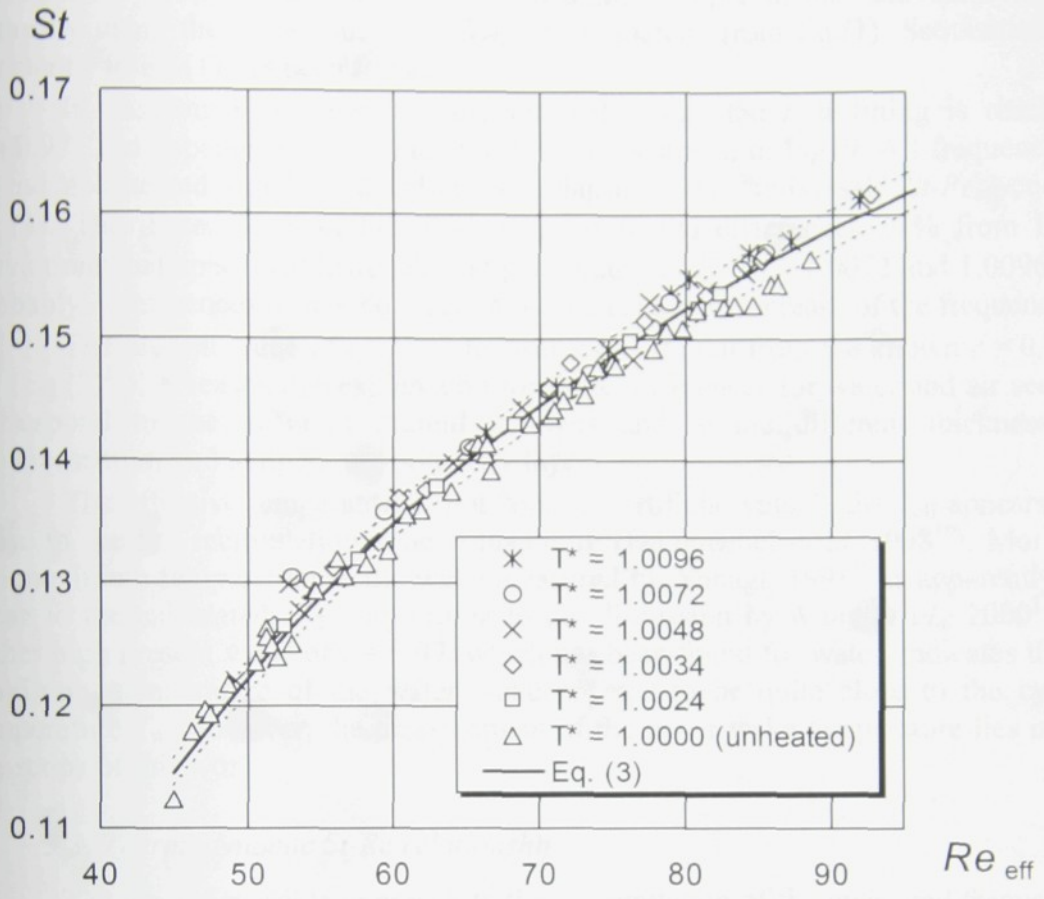

Fig. 9 – The *St-Re*$_{eff}$ relationship of the unheated and heated cylinder in the water flow; *Re*$_{eff}$ was evaluated from Eq. (1) with $c = 0.97$. Smooth line represents correlation Eq. (3)[12], dotted lines correspond to 1% error from it.

Fig. 8 confirms the expected thermal effect in water: cylinder heating causes an increase in frequency. The perturbation of the data does not exceed 1.5%, which can be considered a satisfactory result corresponding to the good arrangement of the present experimental facilities.

Quantification of the thermal effect is discussed in the following two paragraphs (3.2) and (3.3) by means of (3.2) the effective temperature concept[12] and (3.3) the thermodynamic derivation of the *St-Re* relationship[1].

3.2. Effective temperature and St-Re$_{eff}$ *relationship*

The idea of the effective temperature presumes flow similarity at the onset of vortex shedding. An original construction of the effective Reynolds number presumes that critical effective Reynolds numbers are the same for both unheated and heated cases (Lecordier *et al.*, 1991[15], Dumouchel *et al.*, 1998[16], Wang *et al.*, 2000[12]). However, the present T_{eff}- evaluation could not use the mentioned approach. It has been impossible to find the critical *Re* exactly at different ΔT because of the experimental limits mentioned above. Therefore, the definition of the effective temperature was based on the whole *St-Re* curve instead of the critical *Re* number only. In other words, instead of the commonly used approach[15,16,12], which postulated that the critical effective Reynolds number is independent of temperature, we postulated that all the present data

for different temperature ratios (ΔT = 0 to 0.28) collapse to the "universal" St-Re_{eff}-curve by using the Re_{eff}-concept, if T_{eff} is computed from Eq.(1). Sequentially, the constant c in Eq.(1) has been found.

It was found out from the measured data that the best fitting is reached at $c = 0.97$. The dependence of St-Re_{eff} for $c = 0.97$ is shown in Fig. 9. All frequency data of the non-heated and heated cylinders collapse to the "universal" St-Re_{eff}-curve of Eq.(3). The dotted lines in Fig. 9 correspond to the differences ±1% from Eq.(3). Deviations that appears at lower Re and particularly at $T_w/T_\infty = 1.0072$ and 1.0096 point probably at influences of free convection, which causes an increase of the frequency.

The present value of $c = 0.97$ for water is different from the known $c = 0.28$ for air (Eq.(2)[12]). A reasonable explanation for these differences for water and air seems to correspond to the different Prandtl numbers and to the different thicknesses of the momentum and temperature boundary layers.

The effective temperature is not "only an artificial value", the T_{eff} appears to be close to the hot recirculation zone temperature (Dumouchel *et al.*,1998[16]). Moreover, the maximum temperature in the wake measured by Yahagi, 1998[19] is apparently very close to the calculated T_{eff} – according to the discussion by Wang *et al.*, 2000[12]. The rather high present value of $c = 0.97$, which has been found for water, indicates that the maximum temperature of the water wake appears to be quite close to the cylinder temperature T_w. However, the measurement of the water wake temperature lies outside the scope of this work.

3.3. Thermodynamic St-Re relationship

The second possible approach to the interpretation of the measured frequency is

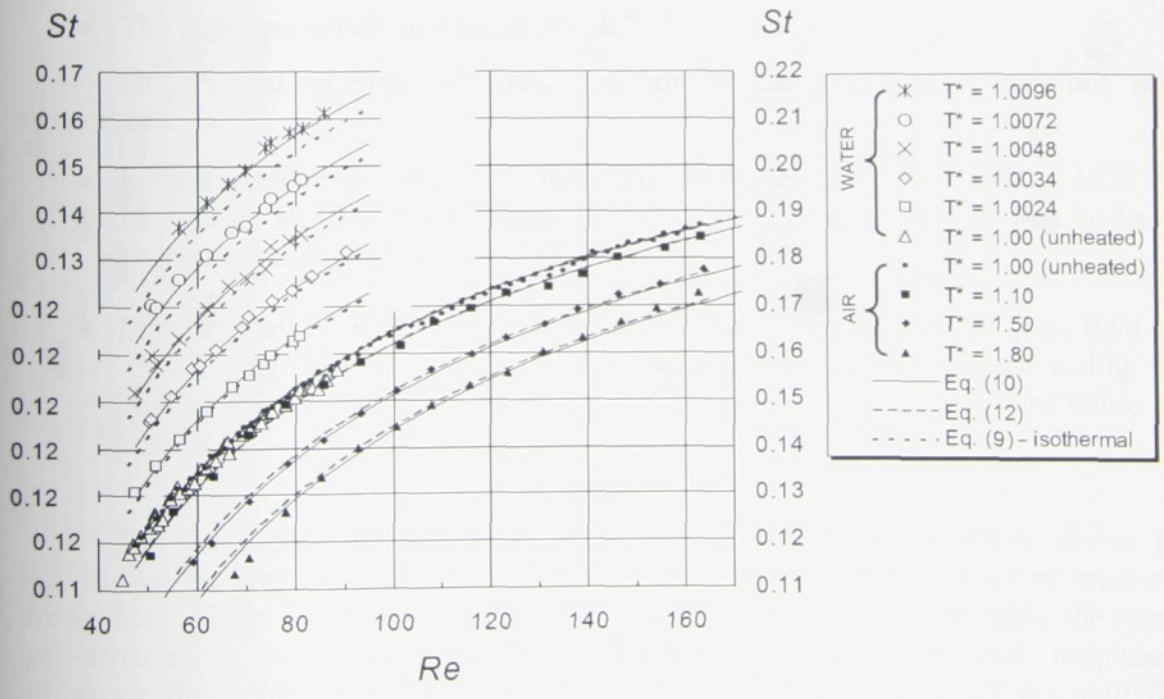

Fig. 10 - The *St-Re* relationship of the unheated and heated cylinder in air and water. Comparison of the experimental data (open symbols denote the present experiments in water, full symbols denote experiments in air by Wang *et al.*, 2000[12]) with the reference unheated cylinder (Eq.(9)[31]), with the correlation based on the experiment in air (Eq. (12)[35]) , and with the theory (Eq. (10)[1]).

based on the thermodynamic derivation of the *St-Re* relationship by Maršík *et al.*[1]. This approach, contrary to the effective temperature concept, is based on the detailed analysis of the velocity and temperature fields. The derivation takes into account the physical properties of various fluids. The resultant equation, which constants 0.2665 and 1.0175 match Eq. (9) (i.e. the isothermal case by Williamson and Brown, 1998[31]), has the following form:

$$St(\mathrm{Re}_\infty, T^*, \mathrm{Pr}_\infty) = 0.2665 - \frac{1.0175}{\sqrt{\mathrm{Re}_\infty}}\left(T^*\right)^{\frac{\omega}{2}}\sqrt{1+\frac{0.227\,(1-T^*)}{\mathrm{Pr}_\infty^{1/3}(2T^*-1)}} \tag{10}$$

where T^* is the temperature ratio $T^* = T_w/T_\infty$, and ω is the exponent in the dependence of the viscosity on temperature defined as

$$m = m_0\left(\frac{T}{T_0}\right)^{\omega} \tag{11}$$

where μ and μ_0 are molecular (dynamic) viscosities at temperatures T and T_0.

Eq. (10) is valid for various fluids, and their different material properties are embodied through their different ω and Pr_∞. The exponent ω for water and air was discussed by Maršík *et al.*[1]:

- For water in the temperature range of 15–30°C, the exponent ω was found from data by Gebhart, 1993[34] in the temperature range $T \in (10; 30)$°C as $\omega = -7.00$.
- The exponent for air was taken $\omega = 0.7774$.

The Prandtl number of water and air at the atmospheric pressure and temperature T_∞:

- Prandtl number of water monotonically decreases from $Pr = 7.99$ at 15°C to $Pr = 5.39$ at 30°C (by Gebhart, 1993[34]). The curves plotted in Fig. 10 have been evaluated at $Pr_\infty = 7.053$ ($T_\infty = 20$°C).
- Prandtl number of air monotonically decreases from 0.71 at 20°C to 0.68 at 300°C (e.g., by Hilsenrath and Touloukian, 1954[36]); curves plotted in Fig. 10 have been evaluated at the common approximation by the constant value of 0.7.

The comparison of the present experimental data with Eq.(10) is shown in Fig. 10. All the present experimental data are plotted in *St-Re* coordinates (the scale on the vertical axis is shifted by $St = 0.01$ for the experiments in water to make the chart well-arranged – similarly as in Fig. 8. Because the temperature and frequency differences in air are much bigger, the data of the experiments in air are not shifted). Moreover, available data of the heated cylinder in air by Wang *et al.*, 2000[12] are plotted into the same graph too.

For the comparison purpose, an expansion of the St-Re_{eff} relationship for air[12] (i.e. Eqs.(2 and 3)) into the St-Re domain was made according to the derivation by Trávníček *et al.*, 2002[35], which yielded the following formula:

$$St = 0.2660 - \frac{1.0160}{\sqrt{Re}}\left(0.72 + 0.28\frac{T_w}{T_\infty}\right)^{0.8887} \tag{12}$$

Moreover, the different thermal effect in two different fluids (water an air) can be elucidated in Fig. 10: Cylinder heating in water increases the vortex shedding frequency thus it destabilizes the wake flow. On the other hand, cylinder heating in air causes the frequency decrease thus the wake flow is stabilized.

4. Conclusions

This paper is concerned with vortex shedding behind a heated circular cylinder in water and air. The first experimental step related to an adjustment of the parallel vortex shedding mode was performed using the flow visualization in water. Sequentially, the hot-wire anemometry in water was used for St-Re data acquisition.

- It has been confirmed that the frequency of vortex shedding is changed with the temperature gradient in the boundary layer. It has been found out that the cylinder heating in water increases the frequency (thermal effect in water). This increase has been measurable even for a relatively small temperature difference $\Delta T = T_w - T_\infty$.

- The effective temperature (T_{eff}) concept has been used for processing of the St-Re data from the hot-wire measurement. The present evaluation of the T_{eff} has been based on the fitting of all St-Re data onto one St-Re_{eff} curve (instead of a commonly known evaluation by means of the flow similarity at the onset of vortex shedding). The resultant effective temperature in water has been found as $T_{eff} = T_\infty + 0.97(T_w - T_\infty)$.

- The present results confirm that the concept of the effective temperature, originally suggested for heated cylinders in air, is suitable and extendable for the heated cylinders in water. The validity of the universal St-Re_{eff} correlation equation has been confirmed.

The results of measuring were also compared to thermodynamic St-Re equation derived by Maršík *et al.*[1], which has the form of $St = f(Re_\infty, T^*, Pr_\infty)$, and which is valid for various fluids. The present experimental data for waterflow have been completed with available data for the heated cylinder in airflow. A satisfactory agreement between St-Re equation by Maršík *et al.*[1] and experimental data for both fluids was achieved.

Acknowledgements

We gratefully acknowledge the support by the Eindhoven University of Technology, by the Grant Agency AS CR (No. IAA200760504), and by the Grant Agency CR (No. 202/04/1341).

References

1. Maršík F., Trávníček Z., Yen R. H., Wang A. B. Fluid dynamics concept for the critical Reynolds number of a heated/cooled cylinder in laminar crossflow (in preparation)
2. Schlichting H., Gersten K. (2000) Boundary-Layer Theory, 8th ed., Springer-Verlag, Berlin.
3. Incropera F.P, DeWitt D.P. (1996) Introduction to Heat Transfer. 3rd. ed, John Wiley & Sons, New York.
4. Zdravkovich M. (1997) Flow around circular cylinders, Vol. 1, Oxford University Press.
5. Monkewitz P.A., Williamson C.H.K., Miller G.D. (1996) Phase dynamics of Kármán vortices in cylinder wakes, Phys.Fluids, Vol.8, 91-96.
6. Mi J., Antonia R.A., (1994) Temperature distribution within vortices in the wake of a cylinder. Int. J. Heat Mass Transfer, Vol. 37, No.6, pp. 1048-1050.
7. Kovasnay L.S.G., (1949) Hot-wire investigation of the wake behind cylinders at low Reynolds numbers, Proc.R.Soc.London, Ser. A 198, 174-190.
8. Collis D.C., Williams M.J. (1959) Two–dimensional convection from heated wires at low Reynolds numbers, J. Fluid Mechanic, 6, 357-384.
9. Lange C.F., Durst F., Breuer M. (1998) Momentum and heat transfer from cylinders in laminar crossflow at $10^{-4} \leq Re \leq 200$, Int. J. Heat Mass Transfer, 41, 3409-3430.
10. Fey U., König M., Eckelmann H., (1998) A new Strouhal–Reynolds–number relationship for the circular cylinder in the range $47<Re<2 \times 10^5$, Phys. Fluids, 10, 1547-1549.
11. Williamson C.H.K. (1996) Vortex dynamics in the cylinder wake, Annual. Rev. Fluid. Mech., 28, 477-539.
12. Wang A–B., Trávníček Z., Chia K–C. (2000) On the relationship of effective Reynolds number and Strouhal number for the laminar vortex shedding of a heated circular cylinder. Physics of Fluids, Vol. *12*, No. 6, pp.1401-1410
13. Yu M-H, Monkewitz P.A. (1990) The effect of nonuniform density on the absolute instability of two-dimensional inertial jets and wakes. Physics of Fluids A, Vol.2, 7, pp. 1175-1181.
14. Herwig H., Wickern G. (1986) The effect of variable properties on laminar boundary layer. Wärme und Stoffübertragung, 20, p, 47-57.
15. Lecordier J.C., Hamma L., Paranthoën P. (1991) The control of vortex shedding behind heated circular cylinders at low Reynolds numbers, Exp. Fluids, 10, No.4, 224-229.
16. Dumouchel F., Lecordier J.C., Paranthoën P. (1998) The effective Reynolds number of a heated cylinder, Int. J. Heat Mass Transfer, 41, No.12, 1787-1794.
17. Shi J.-M., Gerlach D., Breuer M., Biswas G., Durst F. (2004) Heating effect on steady and unsteady horizontal laminar flow of air past a circular cylinder. Phys. Fluids, 16, (12), pp. 4331–4345.
18. Lecordier J.C., Browne L.W.B., Le Masson S., Dumouchel F. , Paranthoën P., (2000): Control of vortex shedding by thermal effect at low Reynolds numbers, Experimental Thermal and Fluid Science, Vol. 21, 4, pp. 227-237.
19. Yahagi, Y. (1998) Structure of two-dimensional vortex behind a highly heated cylinder, Trans. JSME B, 64, 209-215.
20. Roshko A. (1954) On the drag and shedding frequency of two-dimensional bluff bodies, NACA TR 1191.

21. Williamson C.H.K. (1989) Oblique and parallel modes of vortex shedding in the wake of a circular cylinder at low Reynolds numbers, J. Fluid Mech., 206, 579-627.
22. Sabanca M., Durst F. (2003) Flow past a tiny circular cylinder at high temperature ratios and slight compressible effects on the vortex shedding. *Phys. Fluids*, 15, (7), pp. 1821–2003.
23. Eisenlohr H., Eckelmann, H. (1989) Vortex splitting and its consequences in the vortex street wake of cylinders at low Reynolds number, Phys. Fluids A, 1, No. 2, 189-192.
24. Miller G.D., Williamson C.H.K. (1994) Control of three-dimensional phase dynamics in a cylinder wake, Exp. Fluids, 18, 26-35.
25. Hammache D., Gharib M., (1991) An experimental study of the parallel and oblique vortex shedding from circular cylinder, J. Fluid Mech. (232) pp. 567-590.
26. Michaux-Leblond N. , Bélorgey, M. (1997) Near-Wake Behavior of a Heated Circular Cylinder: Viscosity-Buoyancy Duality, Experimental Thermal and Fluid Science, Vol. 15, 2, pp. 91-100
27. Chang K-S, Sa J-Y., (1990) The effect of buoyancy on vortex shedding in the near wake of a circular cylinder, J. Fluid Mech, 220, pp. 253-266.
28. Kieft R.N., Rindt C.C.M, van Steenhoven A.A. (1999): The wake behaviour behind a heated horizontal cylinder, Experimental Thermal and Fluid Science, Vol. 19, Issue 4, pp. 183-232.
29. Maas W.J.P.M., Rindt C.C.M., Steenhoven van A.A.,(2003) The influence of heat on the 3D-transition of the von Karman vortex street, Int. J. Heat Mass Transfer, 46 (16), 3069-3081.
30. Wang A–B., Trávníček Z (2001) On the linear heat transfer correlation of a heated circular cylinder in laminar cross flow by using a new representative temperature concept. Int. J. Heat Mass Transfer, 44, No. 24, pp. 4635-4647.
31. Wiliamson C.H.K., Brown G.L, (1998): A series in $1/\sqrt{Re}$ to represent the Strouhal–Reynolds number relationship of the cylinder wake. Journal of Fluids and Structures, Vol. 12, No. 8, November 1998, pp. 1073-1085.
32. Kieft R.N., (2000) Mixed convection behind a heated cylinder. (PhD. Thesis) Eindhoven University of Technology.
33. König M., Eisenlohr H., Eckelmann H. (1990) The fine structure in the Strouhal-Reynolds number relationship of the laminar wake of a circular cylinder, Phys. Fluids A 2, No.9, pp. 1607-1614.
34. Gebhart B., (1993) Heat conduction and Mass Diffusion, McGraw-Hill, Inc.,New York.
35. Trávníček Z., Wang A.-B., Maršík F.: Flow visualization of the laminar vortex shedding behind a cooled cylinder. In: Int. Symposium on Experimental Mechanics ISEM (CD–proceedings), Ed.: W-C.Wang, Dec. 28-30, 2002, Taipei, R.O.C., C209.
36. Hilsenrath J, Touloukian Y.S. (1954) The viscosity, thermal conductivity, and Prandtl number for air, O_2, N_2, NO, H_2, CO, CO_2, H_2O, He, and A, Trans. ASME , Vol. 76, pp. 967-985.

CHAPTER 5

SYNTHETIC JET

Authors: P. Dančová[a,b], Z. Trávníček[b], T. Vít[a,b]

[a] *Faculty of Mechanical Engineering, Technical University in Liberec, Hálkova 6, 461 17 Liberec, Czech Republic*
[b] *Institute of Thermomechanics, Academy of Sciences of the Czech Republic, Dolejškova 5, 182 00 Prague 8, Czech Republic*

Published in:

Engineering mechanics 2007, pp. 35-36, Svratka(ČR), 14.5.-17.5.2007,
ISBN 978-80-87012-06-2

Summary

Equipments which work on principle of SJ should be found in aerospace industry, in automotive industry, in design of pumps and ejectors, for cooling and heating applications, or for intensification of mixing in chemical reactors. The main advantage of these applications is relative simplicity of SJ equipment. This article introduces the most important works in SJ field. Out of short description of basic mechanism of SJ principle, main part of article is devoted to various field of SJ usage, as is jet vectoring, flow control in external and internal aerodynamics, intensification of heat transfer.

1. Introduction

At the 2006 Geneva Motor Show the new sporty estate by Renault the Altica was presented. Most of studies like this are the demonstration of the virtuosity and professional skills of designers as usual, but this Renault Altica shows many new technical solutions as well. One of these solutions is application of equipment, which works on principle of so-called Synthetic Jet (SJ), for reduction of drag force and thereby decreasing fuel consumption. This SJ equipment, what consists of slot for air outflow and air sucking from surroundings, is inbuilt near to the trailing edge on the roof of the car Renault Altica. Authors of this car concept presume very

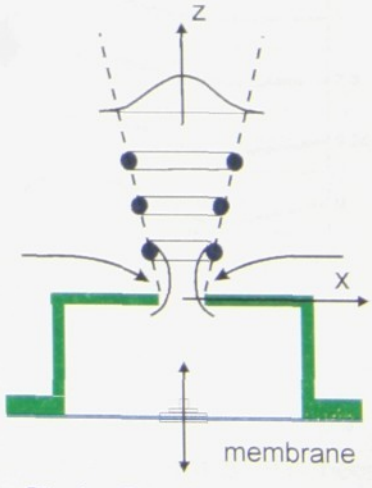

Fig.1 Principle of SJ

optimistic value of fuel consumption reduction of about 15 percent, whereas the SJ equipment power requirement is only 10W (!) [1].

However the Renault Altica is only a pilot project likely never lunched into the series production lines, it shows clearly possibility of outcomes application from present fundamental research.

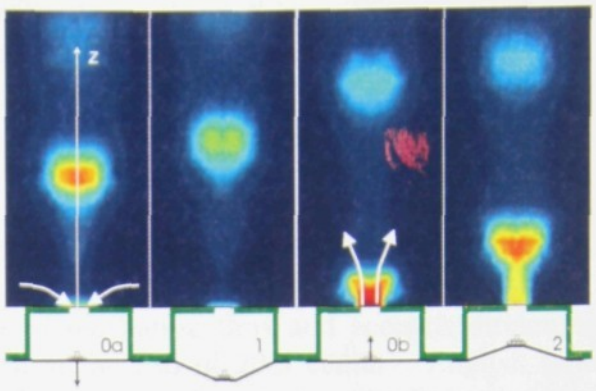

Fig.2 One of working cycle of SJ. Experimental results measured by CTA method with X-wire probe. 2→0a→1 suction; 1→0b→2 extrusion

An example of similar application is a concept of Korean car company Kia Motors Corp. [2], when the car rear bumper is furnished by many circular nozzles which generate SJ (this idea hasn't been presented in Europe up to the present days). Both of these concepts seem to be futurological at least but it has not been refused or neglected.

Equipments which work on principle of SJ should be found not only in automotive industry, but also in aerospace industry (where it helps to increase the lift force or to reduce aerodynamic drag), in design of pumps and ejectors, for cooling (electronics or gas turbine) and heating applications, or for intensification of mixing in chemical reactors. The main advantage of these applications is relative simplicity of equipment because there is no need neither of external flow source (e.g. compressor or fanner) nor incoming piping. It is pity that by missing communication between scientists and engineers these equipments are not used much more in the practical applications.

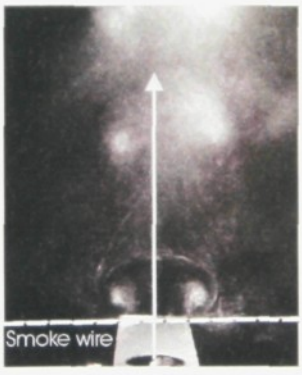

↑Fig.3 Creation of wortex rings by fluid extrusion from cavity of an actuator. Results of „Smoke wire" visualization →Fig.4 Development of flow in nozzle axis during one cycle

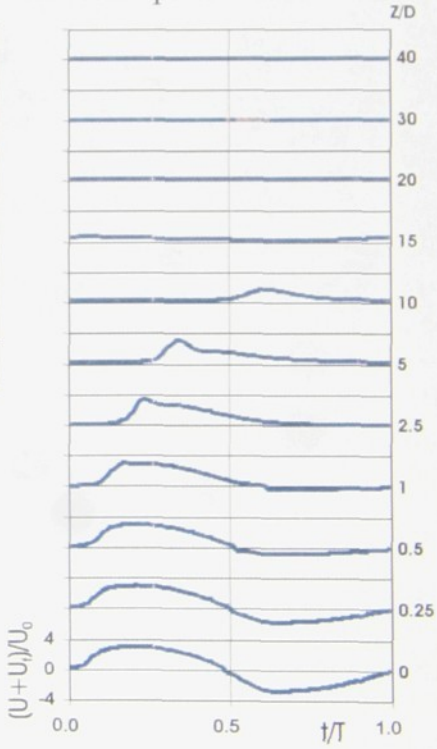

2. History and Present of SJ Research

The first pilot works about problems of SJ are older than the term SJ has been established. One of the first successful applications was already described 50 years ago: Dauphinee [3] used the oscillating diaphragm for the air jet creation in the calibration

equipment for temperature probe. The heat transfer on the wall in presence of SJ and the boundary layer control using SJ are described in the articles [4 and 5].

The creation of fluid jets by means of pulsating pistons was published by e.g. Mednikov and Novitskii [6] or Tesař [7, 8]. Some special applications as so-called "acoustic streaming" (see Meissner [9] and Lighthill [10]), flow caused by oscillating body (Stuart [11]; Davidson and Riley [12]), flow created by acoustic wave – whether stationary (Ingard [13]) or progressive wave (Lebedeva [14]) relate very closely to problems mentioned above.

Research connected with problems of oscillating flow and acoustic streaming has become a theme for intensive research at the end of 20th century. English term „Synthetic Jet" was defined by Smith and Glezer in their paper *The formation and evolution of synthetic jets* in 1998 [15].

There has been extensive research in many important world laboratories at the beginning of the 21st century. For example we can mention some of the largest SJ research centers and some of their significant papers.

USA:	Georgia Institute of Technology [15–20, 57, 64]
	Georgia Technical Research Institute [16, 17, 19]
	Univ. of Wyoming [17]
	Boeing Comp. [17]
	Los Alamos National Laboratory [18, 21, 25]
	Utah State Univ. [21, 23, 25, 30]
	Univ. of Florida [22, 23, 28]
	George Washington University [23, 28]
	Univ. of Texas at Austin [24]
	Texas A&M Univ. [26, 27]
	NASA Langley Research Center [29]
	Auburn Univ. [31]
	Univ. of Washington [32]
Australia:	Univ. of Technology Sydney [33]
	Univ. of New South Wales, Sydney [34]
	Monash University, Melbourne [35, 36]
New Zealand:	Univ. of Auckland [37]
England:	Univ. of Manchester [38, 39]
	Univ. of Sheffield [39, 40, 55]
France:	CNRS [41, 42]
Italy:	Politecnico di Torino [43]
Japan:	National Aerospace Laboratory of Japan [44]
	National Institute of advanced Industrial Science & Technology [44]
Taiwan:	National Taiwan University [53, 58, 59, 67]
South Korea:	Seoul National University [45, 56]

Summary of institutions listed above should not be complete. There is a wide range of possible applications of SJ and there are many more research and industrial organizations which attend to problems of SJ.

Research of SJ whose quality can be compared to the top world research centers is also made in Czech Republic. Valuable research is made at the Institute of Thermodynamics AS CR since 2001. For example the article Trávníček & Tesař [48] is one of the first two known publications dealing with application of SJ for cooling. Other institutions which make research about SJ are e.g. Technical University of Liberec or Czech Technical University in Prague.

The term "Synthetic jet" is translated to the Czech language like "Syntetizovaný proud". This term was presented in 2002 [47] for the first time.

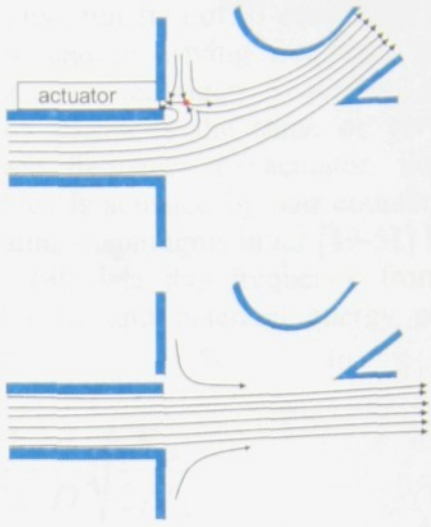

Fig.5 Fluid flow vectoring by SJ, A/ activated SJ, B/ closed SJ

3. Basic Principle of SJ

Synthetic Jets are jets of fluid, which are generated by periodic pulsations of fluid. The oscillating force pushes and pulls this fluid through an orifice (nozzle) from cavity of an actuator. Vortex rings are formed at the lip of the orifice. These rings move with the velocity U_0 that must be high enough to prevent interaction with suction in the orifice. Vortex rings develop and dissipate and SJ has a character of free jet when it is far enough from the end of the orifice. The main advantage of SJ is the zero-net-mass-flux jet that eliminates the requirement of piping for the fluid inlet. Though the nozzle works with zero-net-mass-flux, the momentum in z direction is non-zero. The equipments for SJ can have different design, but the main mechanism and principle is mostly the same. Fig.1 shows simplest setting: There is some orifice on one end of the actuator, whereby the fluid is periodically sucked/exhausted to/from an actuator cavity. The pulsation generator of the fluid can work on principle of loudspeaker, piezo crystal, electromagnet, piston or other equipment. It is necessary to choose an optimal type and construction of actuator in relation to supposed working frequency range, working temperature, kind of working medium and required load of the unit.

Fig.2 shows the working cycle of SJ. Working cycle starts with diaphragm motion from zero position (position 0a) in $-z$ direction. This motion causes fluid sucking into actuator cavity. If the diaphragm deviation is maximum (position 1), the fluid is extruded from orifice of actuator. The biggest velocity of extrusion is in zero deviation of diaphragm (position 0b). Then the diaphragm moves in $+z$ direction to position 2. If the diaphragm achieves position 2, the fluid is sucked again and the cycle is repeated.

Fig.3 shows the vortex rings which are formed at the end of the orifice by fluid extrusion (2D case – there are formed counter-rotating vortex pairs, [15]). Fig.4 shows the development of flow in z direction.

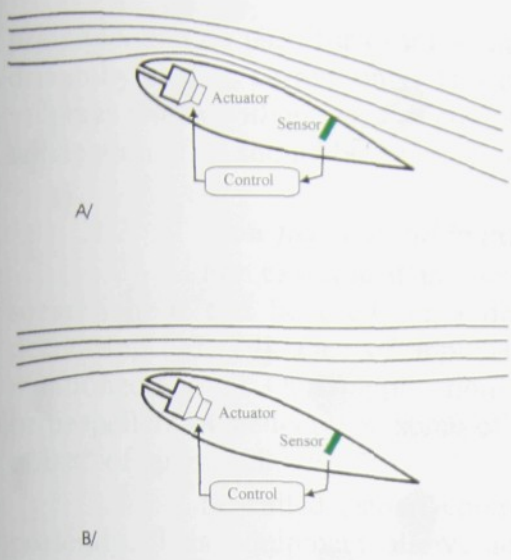

Fig.6 Using of SJ for lift force increasing on wing profile, A/ activated SJ, B/ closed SJ

For optimal function of SJ equipment it is important to choose driving frequency to work in resonance, i.e. eigen frequency of pulsating fluid column is the same or very close like eigen frequency of actuator. For equipment, which is actuated by pair counter-rotating oscillating diaphragms in air [49-51] it is possible to calculate this frequency from equality for kinetic and potential energy of equipment like:

$$f = \frac{1}{2\pi}\frac{d}{D}\sqrt{\frac{K_p}{2\rho L_e}}$$

d is an orifice diameter, K_p is stiffness of loudspeaker diaphragm [N/m^3], D is diaphragm diameter and L_e is „equivalent length" of fluid column (see [49]).

Equipment, which works at these conditions, will have the highest amplitude with the same power requirement (i.e. mass flow is the maximum by given power requirement).

There are some advantages of SJ: flow generation without requirement of manifold for operating medium. Even thought the time-mean mass flux through the nozzle is zero the momentum and the mass flux in the sufficient distance from the nozzle is non-zero. This feature of SJ helps us to place sources of fluid flow anywhere we want without the need of piping.

Another advantage, which is used in different applications, is a high value of turbulence intensity of generated fluid flow. This property is used mainly for heating or cooling.

4. Application

SJ has many significant applications and the number of application is increasing all the time. The most important applications can be divided into two main groups:

A) The main (primary) flow control

B) Using of stand-alone SJ or systems of them

A) The main (primary) flow control

A.1 Jet vectoring [18, 30]:

This category of applications includes the control of flow, which is parallel or perpendicular to the driving jet. Fig.5 shows the principle of jet vectoring. Fig.5a shows the case with activated SJ when the main flow is deflected from direct course and falls into so-called collector whereby leaves away. If the SJ is inactive main flow is not affected by SJ and has direct course (fig.5b). The equipment, which works on this

principle, can be used for example in air distributors. In this case the SJ equipment is driven by electric current only. This equipment which is able to vector substantial flow volumes works without need of complicated mechanical components. Details about this application of SJ should be found in [18] or [30].

A.2. Flow field control in external aerodynamics:

For example it is control of turbulence and control of boundary layer separation. It can be used for a drag reduction, increasing lift force or for noise decreasing [17, 19]. One of applications is concept of Renault Altica [1] (which is mentioned above). Other applications of SJ are possible to find on airfoils [44] (Fig.6) or propellers of helicopters, some of these examples are inscribed as „virtual shaping effect" of airfoil [28, 29].

So-called „smart control" of the airfoil shape is intensively discussed presently. This equipment allows adapting of main characteristics of the airfoil to instantaneous conditions in the boundary layer or to the requirements of external control unit. It is possible to improve airfoil parameters and the system maneuverability or to simplify or completely remove mechanical control systems on wings. These technologies are a special perspective in small and very small pilotless planes (Micro Air Vehicle MAV, Unmanned Aerial Vehicle UAV), eventually in analogous underwater vehicles (Autonomous Underwater Vehicle [53]).

The other perspective application of SJ is focused on improvement of wind power plant propellers characteristics (presently analyzed at IT CAS). The main objective of this research is to increase lift to drag ratio and to decrease aerodynamic noise [54,55].

Example of SJ flow influence on aerodynamic drag of "bluff body" is described in [56]. Fig.7 shows results of numerical simulation of flow past a bluff body, which has nozzles at the trailing edge. These nozzles alternately push and pull flow of fluid. This figure shows flow field past rectangular bluff body in case a/ nozzles don't work, b/ nozzles work in phase, i.e. nozzles push fluid at once and pull fluid at once, c/ nozzles work in antiphase, i.e. if one of nozzles push the fluid, the second pull the fluid and conversely. Results show ability to decrease drag coefficient for about 25 percent with application of this equipment. It is necessary to regulate frequency and power of SJ in relation to fluid velocity to achieve optimal drag reduction. The rectangular profile should represent a car model in this case.

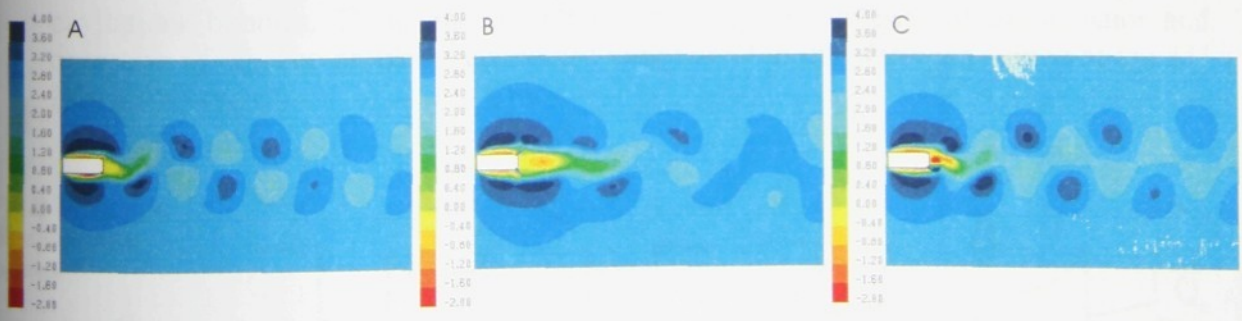

Fig.7 Wake past bluff body (numerical simulation), A/ without SJ, B/ SJ nozzles work in phase, C/ SJ nozzles work in phase opposition

A.3. Flow field control in internal aerodynamics:

Turbulence control and control of boundary layer separation is another typical example of SJ application. Fluid flow through wide-open diffuser, which is susceptible to separate from the wall, can be stabilized by SJ [42]. Suppression of undesirable flow separation increases efficiency effectively and decreases power loss.

A.4. Increase of mixing intensity

Increase of mixing intensity has importance in many chemical processes, such as in combustion [42]. Typical setting is numerically solved in paper [57]: The air and fuel flows move into combustion chamber where SJ improves their mixing. It is possible to improve parameters of the combustion equipment, e.g. to increase power, to decrease Noxious emissions, or to decrease overall dimensions eventually.

A.5. Increasing of heat transfer due to main flow control:

Very interesting example of application of SJ is cooling of electronics with very small dimensions [34] (Micro-Electro-Mechanical Systems, MEMS). In these small dimensions there is often laminar flow and heat transfer is unacceptably small. Numerical study [34] simulates intensification of electronic processor's cooling: the laminar airflow is heated from one-side and affected by SJ from other side. Laminar flow is disturbed by SJ (authors discuss pseudo-turbulence). For proper setting and for proper flow parameters the study [34] shows how it is possible to improve processor cooling.

B) Using of stand-alone SJ or systems of them

B.1. Action of force for control of motion, e.g. for autonomous vehicle in the water and in the air.

Recently, there were developed new generations of SJ generators, in particular hybrid SJ and double-acting SJ [58-62] (IT CAS, TU Liberec, Univ. Sheffield a National Taiwan Univ.). The purpose of these works has been improvement of SJ, in particular on the field of electronics cooling. In addition to the improved geometry of SJ generator can be used for nozzle design for autonomous underwater vehicle (AUV).

Function of SJ in the water is specific. Though SJ in the water works in relati low frequency (some tens of Hz by macroscopic scale of centimeters), gases dissolved in the fluid are released, cavitation increases due to considerable acceleration of fluid on actuator surface. The decrease of the pressure in the actuator leads to the formation of cavitations bubbles. These bubbles affect adversely the stiffness of the actuator and operation of SJ. The problems connected with the SJ in the water are solved at the TU Liberec nowadays.

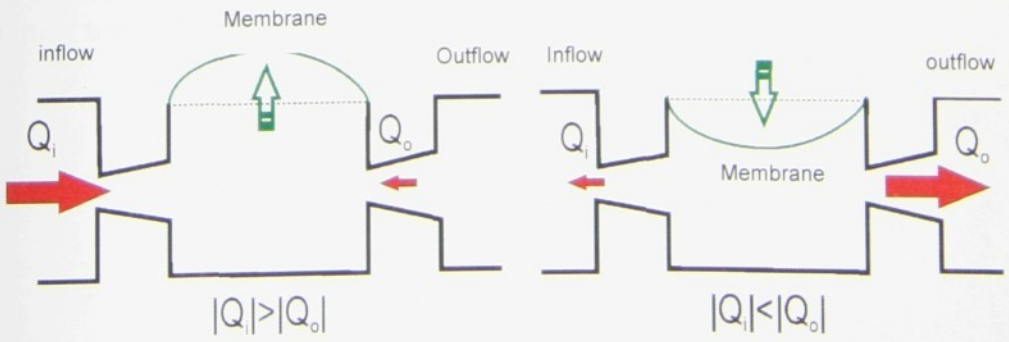

Fig.8 Principle of valveless pump

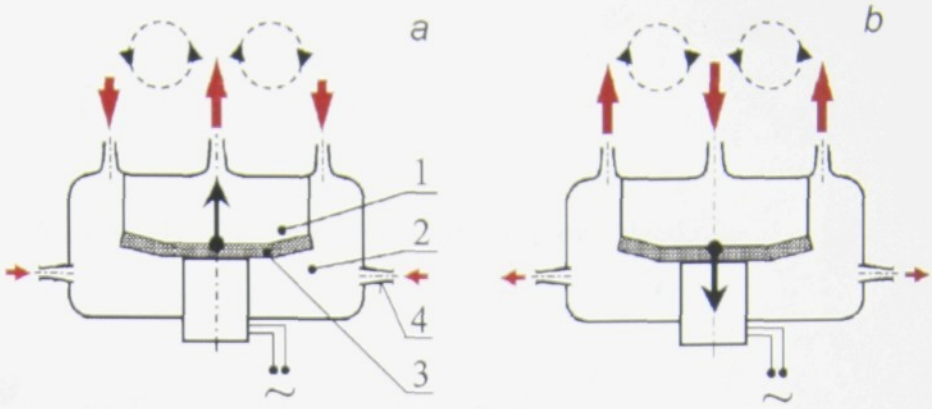

Fig. 9. Double-acting hybrid synthetic jet actuator

B.2 SJ used for intensification of the heat transfer

This group of applications contains cases as impact SJ [4, 20, 48, 50, 51] and cases of complex fluid fields generated by SJ only [64]. A pulsation of the jet together with the high level of turbulence intensity leads into the strong increase of the heat transfer coefficient when the equipment is designed properly and the heated or cooled surface is placed in the right position. Due to this advantage there is a wide range of applications in the field of cooling of heavy thermally loaded parts in electronics or for cooling of blades in combustion turbines. More details about these questions are possible to find in e.g.[50, 51, 58-62]

Combination of SJ with pump or ejector brings other options. Fig.8 shows an example of valve-less pumps design [65]. This valve-less pump consists of two diffusers and of chamber with actuator. Diffusers are optimalized to have bigger drag in one direction than in the opposite direction. Periodic motion of actuator produces sucking of fluid by first of diffusers and extrusion by second of diffusers. This equipment is able to have very heavy duty by very small size. Improvement in particular is by MEMS systems.

An idea to combine SJ and valve-less pump led to design of hybrid synthetic jet actuator [66]. Fig.9 shows a design of double-acting hybrid synthetic jet actuator. Fig.9a shows period of extrusion from front chamber (1), if the fluid is sucked simultaneously in back chamber (2). Opposite period (sucking into front chamber) is shown on fig.9b. Resulting flow has time-mean mass flow of fluid in actuator non-zero – it enables to achieve better results in noted applications [58,59].

5. Conclusion

Equipments, which work on SJ principle, have simple construction and many advantages. It depends on ingenuity and confidence of designers and managers if they resolve to use new technologies in their products.

6. Acknowledgment

Grant support of GAČR No. 101/05/2681 is gratefully acknowledged.

7. References

1. Renault Altica: 44MPG Diesel Concept with Active Airflow Management, http://www.greencarcongress.com/2006/02/renault_altica_.html
2. K.G. Hyeon, Rear bumber for vehicle by using synthetic jet and reducing drag. Patent KR2003041242, Kia Motors Corp., May 27, 2003.
3. Dauphinee T.M., Acoustic air pump, The Review of Scientific Instruments, 28, No. 6, (1957) 456.
4. Y. Yassour, J. Stricker, M. Wolfshtein, Heat transfer from a small pulsating jet, Proceedings of the 8th International Heat Transfer Conference, Vol. 3, Hemisphere Publ., San Francisco, USA, 1986, pp. 1183–1186.
5. Meier H.U., Zhou M-D., The development of acoustic generators and their application as a boundary layer transition control device. Exp. Fluids 11 (1991) 93-104.
6. E. P. Mednikov and B. G. Novitskii, Experimental study of intense acoustic streaming, Sov. Phys. Acoust., 21 (1975) 152–154.
7. Tesař V., 1982, Fluidic Jet–Type Rectifier: Experimental Study of Generated Output Pressure, Fluidics Quarterly, Ann Arbor U.S.A, Vol. 14, Nr. 4.
8. Tesař V., 1991, Entrainment action of an alternating inflow into and outflow from a nozzle. Acta Polytechnica- Práce ČVUT v Praze 1, (II, 1), pp. 43-61, (in Czech).
9. Meissner, Über piezo–elektrische Kristalle bei Hoch–frequenz, Zeitschrift für technische Physik, Vol.7, No. 12, (1926) pp. 585-592.
10. M. J. Lighthill, "Acoustic Streaming," J. Sound Vib., 61, 391-418 (1978).
11. J. T. Stuart, "Double boundary layers in oscillatory viscous flow," J. Fluid Mech., 24, 673-687 (1966).
12. B. J. Davidson and N. Riley, "Jets induced by oscillatory motion," J. Fluid Mech., 53, 287 (1972).
13. Ingard, U., On the theory and design of acoustic resonators, J. Acoustical Soc. of America, Vol. 25, No. 6, 1953, pp. 1037–1060
14. V. Lebedeva, "Experimental study of acoustic streaming in the vicinity of orifices," Sov. Phys. Acoust., 26, 331 (1980).
15. Smith, B.L., Glezer, A., The formation and evolution of synthetic jets (Physics of Fluids 10 2281 – 2297, 1998.
16. Glezer A., M. Amitay, "Synthetic jets," Annu. Rev. Fluid Mech. 34, (2002) 503–529.
17. M. Amitay, D. R. Smith, V. Kibens, D. E. Parekh, A. Glezer, Aerodynamic flow control over an unconventional airfoil using synthetic jet actuators. AIAA J. 39 (2001) (3) 361 – 370.
18. B.L. Smith and A. Glezer, "Jet vectoring using synthetic jets," J. Fluid Mech. 458, 1–34 (2002).
19. M. Amitay and A. Glezer, "Controlled transients of flow reattachment over stalled airfoils," Int. J. Heat Fluid Flow 23, 690–699 (2002).
20. D.S. Kercher, J.-B. Lee, O. Brand, M.G. Allen, and A. Glezer, "Microjet cooling devices for thermal management of electronics," IEEE Trans. Compon. Packaging Technol. 26 (2), 359–366 (2003).
21. B.L. Smith and G.W. Swift, "Power dissipation and time-averaged pressure in oscillating flow through a sudden area change," J. Acoust. Soc. Am. 113 (5), 2455–2463 (2003).
22. Q. Gallas, R. Holman, T. Nishida, B. Carroll, M. Sheplak, and L. Cattafesta, "Lumped element modeling of piezoelectric-driven synthetic jet actuators ," AIAA J. 41 (2003) (2), 240–247.
23. R. Holman, Y. Utturkar, R. Mittal, B.L. Smith, and L. Cattafesta, "Formation criterion for synthetic jets," AIAA J. 43, (10) 2110–2116 (2005).

24. C.Y. Lee and D.B. Goldstein, "Two-dimensional synthetic jet simulation,"AIAA Paper 2000-0406, (2000).
25. B.L. Smith and G.W. Swift, "A comparison between synthetic jets and continuous jets," Exp. Fluids 34, 467–472 (2003).
26. J.L. Gilarranz, L.W. Traub, and O.K. Rediniotis, "A new class of synthetic jet actuators—Part I: Design, fabrication and bench top characterization," J. Fluids Eng.-T. ASME 127, 367–376 (2005).
27. J.L. Gilarranz, L.W. Traub, and O.K. Rediniotis, "A new class of synthetic jet actuators—Part II: Application to flow separation control," J. Fluids Eng.-T. ASME 127, 377–387 (2005).
28. R. Mittal and P. Rampunggoon, "On the virtual aeroshaping effect of synthetic jets," Phys. Fluids 14, 1533–1536 (2002).
29. F-J. Chen and G.B. Beeler, "Virtual shaping of a two-dimensional NACA 0015 airfoil using synthetic jet actuator," AIAA Paper 2002-3273, (2002).
30. Bettridge, M.W., Spall R.E., Smith B.L., Aerodynamic Jet Vectoring Using Steady Blowing and Suction, 42nd AIAA Aerospace Sciences Meeting, January 5-8, 2004, Reno, NV, AIAA 2004-0921.
31. A. Ahmed, Z. Bangash, Axisymmetric coaxial synthetic jets, AIAA 40th Aerospace Sciences Meeting & Exhibit No. 2002–0269, 2002.
32. Liang Y., Kuga Y., Taya M., Design of membrane actuator based on ferromagnetic shape memory alloy composite for synthetic jet applications. Sensors and Actuators A 125 (2006) 512–518.
33. S.G. Mallinson, J.A. Reizes, and G. Hong, "An experimental and numerical study of synthetic jet flow," Aeronaut. J. 105 (1043), 41–49 (2001).
34. Timchenko V., Reizes J.A., Leonardi E., Stella F., Synthetic jet forced convection heat transfer enhancement in micro-channels. In.: Proc. 13th International Heat Transfer Conference IHTC-13, Sydney, NSW Australia, Aug. 13-18, 2006, Eds. G. de V. Davis and E. Leonardi, MIC-21.
35. J.E. Cater and J. Soria, "The evolution of round zero-net-mass-flux jets," J. Fluid Mech. 472, 167–200 (2002).
36. M. Gordon and J. Soria, "PIV measurements of a zero-net-mass-flux jet in cross flow," Exp. Fluids 33 (6), 863–872 (2002).
37. Sharma R.N.,An Analytical Model for Synthetic Jet Actuation. 3rd AIAA Flow Control Conference, June 5-8, 2006, San Francisco, California. AIAA 2006-3035.
38. A. Crook, N.J. Wood, Measurement and visualizations of synthetic jets, AIAA Paper 2001-0145.
39. V. Tesař and S. Zhong, "Efficiency of synthetic jets generation," Trans. Aeronaut. Astronaut. Soc. Rep. China 35 (1), 45–53 (2003).
40. V.Tesař, Z. Trávníček, (2005), Review: Pulsating and synthetic impinging jets. Journal of Visualization, Vol. 8, No. 3, pp. 201-208.
41. J. Tensi, I. Boué, F. Paillé, and G. Dury, "Modification of the wake behind a circular cylinder by using synthetic jets,"J. Visual. 5, (1), 37–44 (2002).
42. M. Ben Chiekh, J.C.Bera, and M. Sunyach, "Synthetic jet control for flows in a diffuser: vectoring, spreading and mixing enhancement," J. Turbulence 4, No. 032 (2003).
43. Cicca G.M., Iuso G., Viviano A., Onorato M., Spazzini P.G, Malvano R., PIV study of synthetic jets. 7th Int. Symp. on Fluid Control, Measurement and Visualization FLUCOME 2003, Sorrento.
44. Nishizawa, A. et. al., Toward smart control of separation around a wing-Active separation control systém part 2, Proc 5th Symp. Smart Control of Turbulence, Univ Tokyo, February 29-March 2, 2004, pp. 7-14.
45. Kim S.H., Kim C., Separation control on NACA23012 using synthetic jet, 3rd AIAA Flow Control Conference, June 5-8, 2006, San Francisco, California.
46. Trávníček Z., 2001, Anulární impaktní proud s akustickým buzením (visualizace proudového pole a přestup hmoty na obtékané stěně). Výzkumná zpráva ÚT AV ČR, Praha, Z-1310/01.
47. Trávníček Z., 2002, Příklady použití kouřové visualizace proudění v experimentální mechanice tekutin. VVI (Vytápění větrání instalace), Vol. 11, No. 5, pp. 230-233.
48. Z. Trávníček and V. Tesař, Annular synthetic jet used for impinging flow mass–transfer, Int. J. Heat Mass Transfer 46, 3291–3297 (2003).
49. Z. Trávníček, F.Maršík, T.Vít, P. de Boer, Synthetic jet actuation at the resonance frequency, In: Proc. XXI International Congress of Theoretical and Applied Mechanics (ICTAM), August 15-21, 2004, Warsaw, Poland, p. 113.

50. Z. Trávníček , J. Vogel, T. Vít, and F. Maršík, "Flow field and mass transfer experimental and numerical studies of a synthetic impinging jet," In: Proc. 4th International Conference on Heat Transfer, Fluid Mechanics and Thermodynamics (HEFAT2005), Cairo, Egypt, No. ZT4 (2005).
51. Trávníček Z., Hyhlík T., Maršík F., (2005), Synthetic jet impingement heat/mass transfer. Journal of Flow Visualization and Image Processing, Vol. 13, 2006, in press.
52. Uruba V., Flow control using synthetic jet actuators. Engineering Mechanics 12 (1) (2005) 41-62.
53. Chen C-C., Chou C.C., Hsu S-S., Wang A-B, Visualization of new synthetic jet actuator for underwater vehicles. In: Proc. 12th Inter. Symp. on Flow visualization ISFV-12, Sept. 10-14, 2006, Göttingen, Germany, No. 86.4.
54. Tesař V., Fluidics applied to flow control by synthetic jets, In: Topical Problems of Fluid mechanics 2006,Feb. 22-24, 2006, Institute of Thermomechanics, Prague, 171-174.
55. Tesař V., Hung C.-H., and Zimmerman W.B., "No-moving-part hybrid-synthetic jet actuator," Sensors and Actuators A 125 (2), 159–169 (2006).
56. Choi H., Active control of flows over bluff bodies for drag reduction. In: 6th Symposium on Smart Control of Turbulence, March 6-9, 2005. National Maritime Research Institute 6-38-1, Shinkawa, Mitaka, Japan. http://www.turbulence-control.gr.jp/index_e.html, www.nmri.go.jp/turbulence/PDF/symposium/FY2002/Choi.pdf.
57. Wang. H., Menon S., Fuel-air mixing enhancement by synthetic microjets. AIAA J. 39 (12) (2001) 2308-2319.
58. Z. Trávníček, A.I. Fedorchenko, and A-B. Wang, "Enhancement of synthetic jets by means of an integrated valve-less pump, Part I: Design of the actuator," Sensors and Actuators A 120 (1), 232–240 (2005).
59. Z. Trávníček, V. Tesař, and A-B. Wang, "Enhancement of synthetic jets by means of an integrated valve-less pump, Part II: Numerical and experimental studies," Sensors and Actuators A 125 (1), 50–58 (2005).
60. Z. Trávníček, T. Vít, V. Tesař, Hybrid synthetic jet as the non-zero-net-mass-flux jet, Physics of Fluids, 18 (8) (2006).
61. Trávníček Z., Vít T., Hybrid synthetic jet intended for enhanced jet impingement heat/mass transfer. In.: Proc. 13th International Heat Transfer Conference IHTC-13, Sydney, NSW Australia, Aug. 13-18, 2006, Eds. G. de V. Davis and E. Leonardi. JET–15.
62. Trávníček Z., Vít T., Hyhlík T., Maršík F., Heat/mass transfer of the pulsatile impinging jets. In: Proc. 5th International Symposium on Turbulence, Heat and Mass Transfer (THMT-5), Dubrovnik, Croatia, Sept. 25-29, 2006, Eds. K.Hanjalič, Y.Nagano, and S.Jakirlič, pp. 437–440.
63. Dančová P., Studie proudění typu „Synthetic Jet", Diplomová práce, FS-TU Liberec, 2005.
64. Mahalingam R., Glezer A., An Actively cooled heat sink integrated with synthetic jets, In: Proc. 35th National Heat Transfer Conference, June 10-12, 2001, Anaheim, California, USA, NHTC2001-20025.
65. Olsson A., Stemme G., Stemme E., A valve-less planar fluid pump with two pump chambers, Sensors and Actuators A 46-47 (1995) 549-556.
66. Trávníček Z., Tesař V., Hybridní syntetizované proudy. In: Anotace významných výsledků pracovišť AV ČR za rok 2005, I. Oblast věd o neživé přírodě, 2. sekce aplikované fyziky, 2.16. http://www.cas.cz/anotace_txt.php?ID=89#2.16

CHAPTER 6

SYNTHETIC JET ACTUATION AT THE RESONANCE FREQUENCY

Authors: Z.Trávníček[a], F.Maršík[a], T.Vít[b], P.de Boer[c]

[a] *Institute of Thermomechanics, Academy of Sciences of the Czech Republic, Dolejškova 5, 182 00 Prague 8, Czech Republic*
[b] *Faculty of Mechanical Engineering, Technical University in Liberec, Hálkova 6, 461 17 Liberec, Czech Republic*
[c] *Energy Technology Division, Department of Mechanical Engineering, Eindhoven University of Technology, WH-3.127, P.O. Box 513, NL-5600 MB Eindhoven, Netherlands*

Published in:

21 International Congress of Theoretical and Applied Mechanic (ICTAM 2004), pp.113,Warszawa, Poland, 2004, ISBN 83-89687-01-2

Summary

An air round jet was generated by a zero–net–mass–flux actuator. A satisfactory jet synthesis was confirmed experimentally by smoke visualization and hot-wire anemometry. The choice of suitable operating frequency was found near the resonance by means of theoretical as well as experimental approach. In the far field, the streamwise decay of the time-mean velocity is comparable with a conventional (steady) jet.

1. Introduction

Synthetic jets are generated by an oscillating force which pushes and pulls a fluid through an orifice (or nozzle) from a cavity [1]. The synthetic jets have many perspective applications such as control of primary flows [1, 2] and a valuable alternative for cooling applications [3].

The synthetic jets are characterized by two length scales: The length scale of the output orifice (diameter D), and the "stroke length" L_0 [1]; another name is the "equivalent extruded (fluid) column length", [2]; the L_0 is defined by integration of the the orifice velocity over the extrusion (discharge) stroke [1]. The Strouhal number is an only slightly modified ratio of the length scales D and L_0: e.g., at harmonic actuation $St = (1/\pi)\, f\, D/U_0 = (1/\pi)\, D/L_0$ [2], where f is frequency, U_0 is the time–mean orifice velocity during the extrusion stroke, i.e. $U_0 = L_0/T$, and T is the time period, i.e. $T = 1/f$.

There are many possible definitions of the Reynolds number, one of them sounds as $\mathrm{Re} = U_0 D/\nu$, [1].

2. Results and Discussion

The present actuator consists of a sealed cavity, which is equipped with an actuating pair of diaphragms $D_D = 66.5$ mm in diameter, and with an emitting orifice $D = 8.0$ mm in diameter. The jet is oriented vertically upwards, a sinusoidal current feeds the actuator. An initiation step of the experiments was made by flow visualization by the smoke–wire technique. Further, the velocity distribution was measured by a hot–wire anemometer (DANTEC: CTA Bridge 56C17, Mean Value Unit 56N22, StreamLine 90N10 Frame, and CA-1000) in the constant temperature mode.

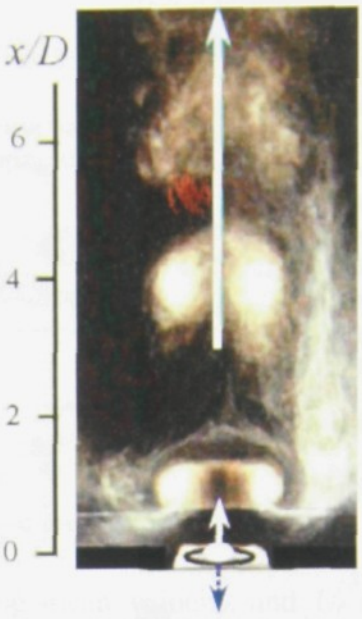

Fig. 1
Synthetic jet visualization, $f = 30$ Hz, $L_O/D = 3.2$.

Analysis: resonance frequency of the actuator

From the point of view of energy transformation, the potential energy of the pair of diaphragms is transformed into the kinetic energy of fluid during each period. The oscillating diaphragms are assumed as harmonic motion, and the relationship between the velocities of the actuating diaphragms and the flow in the orifice satisfied the continuity equation (incompressible flow). In the top/bottom dead centers of the diaphragms, the kinetic energy of fluid is zero and the potential energy is maximum. On the other hand, in the neutral position of the diaphragms, the kinetic energy is maximum. The potential energy of the diaphragms can be written as for linear springs, and the resonance frequency can be derived as:

$$f = \left(\frac{1}{2\pi}\right)\left(\frac{D}{D_D}\right)\sqrt{\frac{K_P}{2\rho L_e}} \tag{1}$$

where K_P is the diaphragm (spring) constant (it was evaluated by an auxiliary experiment), ρ is fluid (air) density, and L_e is the "fluid column length" which captures the kinetic energy. For the present geometry, Eq. (1) gives $f = 78.5$ Hz.

The *"nominal operating frequency"* has been refined according to the experimental results as $f = 75.0$ Hz.

Experimental results: Flow visualization and hot-wire measurement

Fig. 1 presents the visualization of the typical synthetic jet obtained using multiple exposures at low frequency actuation (30Hz) during 1s, (it means, 30 superimposed frames were exposed). Fig. 1 shows the so–called "short L_0" (or "high St") synthetic jet, which was generated at $L_0/D = 3.2$, i.e. $St = 0.10$, and $Re = 400$, i.e. $U_0 = 0.78$ m/s.

Counter-rotating vortex pairs are formed at the nozzle exit, and they are distinguishable during their upward motion from the nozzle. According to Fig. 1, the streamwise distances from the nozzle to the first and second vortex pairs are

approximately $1D$ and $4D$, thus the average pitch of the train of individual vortex pairs is approximately $\Delta x_V = 3D$. This Δx_V – value is rather well comparable with the "equivalent extruded column length" $L_0 = 3.2$ D. Fig. 2 shows results of hot-wire measurements of the "long L_0" (or "low St") synthetic jet, which was generated at the "nominal operating point": $f = 75$ Hz, $L_0/D = 14.3$, i.e., $St = 0.022$, and $Re = 4400$, i.e., $U_0 = 8.7$ m/s. Fig. 2 shows the centerline velocities during the actuating cycle namely the phase averaged velocity; U is the time–mean velocity and U_f is the periodic component. This plotting demonstrates a formation of the pulsatile jet when fluid "puff" travels downstream, thus the velocity amplitude moves downstream, and the velocity oscillations gradually diminish. The time–mean velocity U along the centerline is plotted as well. The maximum velocity in the orifice is approximately $3.05U_0$. Behind the orifice, the maximum velocity increases slightly at first, mainly because of the velocity profile formation there; the highest value is nearly 3.5 U_0 at $x = 2.5D$. From $x/D = 3.75$, the maximum velocity starts to decrease. In fact, a periodic character of the jet is clearly distinguishable approximately up to $x/D_0 = 20$. Further downstream, the initially pulsatile jet remains a conventional (steady) fluid jet with a constant monotonically decreasing streamwise velocity. The streamwise decay of the centerline time-mean velocity of the investigated (originally pulsatile) jet was evaluated as $U \sim x^{-1.04}$. It is very close to the well known proportionality $U \sim x^{-1.0}$ of conventional axisymmetric fully developed turbulent jets.

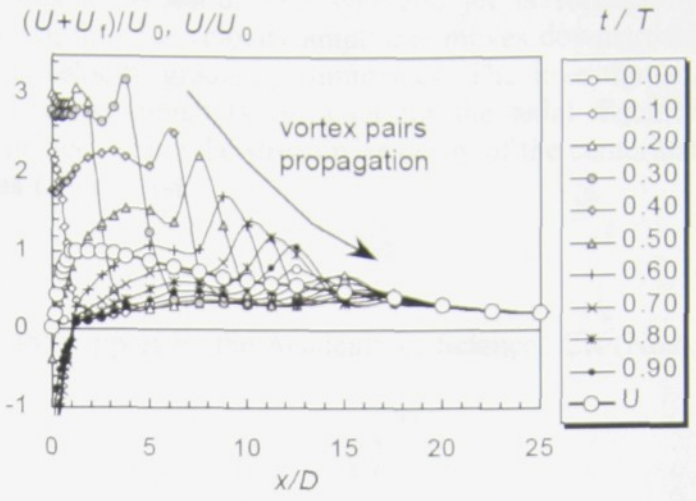

Fig. 2 Phase averaged centerline velocity.

3. Conclusion

A round air jet was generated (synthesized) by means of a zero–net–mass–flux actuator from a train of counter-rotating vortex pairs. The choice of suitable operating frequency was found by means of both theoretical as well as experimental approach: The resonance frequency of the actuator was derived theoretically. In addition, the hot-wire measurement revealed a relationship between the time-mean velocity and the driving frequency. The chosen "nominal operating frequency", $f = 75.0$ Hz, agrees very well with both the theoretical and experimental results.

The expected function of the actuator has been tested experimentally by smoke visualization (using phase–locked multi–expositions) and hot-wire anemometry. The hot-wire data were processed using the phase-averaged technique, and the velocity was decomposed into the time–mean velocity, periodic and fluctuation components. The experiments have confirmed a satisfactory function of the "fluid jet synthesis". Two typical synthetic jets have been presented here, namely the "long–" and "short–extruded columns L_0" cases. The maxima of the centerline local and the time–mean velocities reached approximately 27 m/s and 8.7 m/s, respectively; it was occurred at the "nominal operating point" which produces the "long L_0" synthetic jet.

The maximum Reynolds number was $Re = 4400$. The synthetic jet is formed by travelling of fluid "puffs" downstream, thus the velocity amplitude moves downstream and the periodic component of the velocity gradually diminishes. The investigated, originally pulsatile jet resembles a conventional (steady) jet for the axial distance greater than 20 diameters from the orifice, where the streamwise decay of the centerline time-mean velocity was evaluated as $U \sim x^{-1.04}$.

Acknowledgement

We gratefully acknowledge the support by the Academy of Sciences CR (No.6, IT No. 50026).

References

1. Smith B.L., Glezer A.: The formation and evolution of synthetic jets, Phys. Fluids 10 2281–2297, 1998.
2. Tesař V., Zhong S.: Efficiency of synthetic jets generation, Transactions of the Aeronautical and Astronautical, Society of the Republic of China 35 (1) 45–53, 2003.
3. Trávníček Z., Tesař V.: Annular synthetic jet used for impinging flow mass–transfer, Int. J. Heat Mass Transfer, 46 3291–3297, 2003.

CHAPTER 7

ANALYSIS OF A SYNTHETIC JET

Authors: Petra DANČOVÁ, Tomáš VÍT

Technical University of Liberec, Department of Power Engineering Equipment Studentská 2, 461 17 Liberec 1, Czech Republic, Phone:+ (420) 485 353 406 Fax: + (420) 485 353 433 Email: petra.dancova@tul.cz
Institute of Thermomechanics of the ASCR, v. v. i., Dolejškova 5, 182 00 Prague, Czech Republic

Published in: Journal of Applied Science in Thermodynamics and Fluid Mechanics, Vol. 2, No. 1/2008

Abstract

This paper focuses on research into the properties of a Synthetic Jet operating in water. It presents the design of a unique experimental setup and the results of various experiments and numerical simulations.

Also presented are results of visualizations via an electrolytic precipitation method – a so called Tin ions visualization, results of experiments achieved by Hot-wire Anemometry and numerical simulations carried out by means of the Finite Volume Method. The Hot-wire Anemometry experiments were focused on determining the nominal frequency of the actuator and on measuring different velocity profiles.

Based on the presented results, a parametric experimental investigation is planned for the future.

1 Introduction

A Synthetic Jet (SJ) is generated (synthesized) by interactions within a train of vortex rings or counter-rotating vortex pairs in axi-symmetric or two-dimensional geometry, [1, 2]. The main advantage of a SJ is a flow without fluid supply – specifically, the SJ actuator has zero-net-mass-flux (ZNMF). ZNMF eliminates the need for piping to accommodate a fluid inlet.

A SJ has many significant applications, of which the number is increasing continuously. The most important applications can be divided into two main groups:

1) The main (primary) flow control:
   A SJ is used for jet vectoring, flow field control in external and internal aerodynamics and for increasing the intensity of mixing.

2) Use of a stand-alone SJ or systems including a SJ:
A SJ is used for intensification of heat transfer.

2 Synthetic Jet Parameters

A SJ is characterized by various parameters. The main parameters are:

- The actuator orifice diameter D
- The "stroke length" L_0

$$L_0 = \int_0^{T/2} u_0(t)dt \tag{1}$$

where $u_0(t)$ is the periodical axial orifice velocity, and T is the time period.

- The time-mean orifice velocity U_0 is defined as the axial orifice velocity on the axis over the extrusion (discharge) stroke as:

$$U_0 = \frac{L_0}{T} = L_0 \cdot f \tag{2}$$

where f is the actuator frequency.

- The Reynolds number of a SJ is defined as:

$$\mathrm{Re} = \frac{U_0 \cdot D}{\nu} \tag{3}$$

- The Strouhal number is defined with the use of eq. (2) as:

$$St = \frac{1}{\pi}\frac{f \cdot D}{U_0} = \frac{1}{\pi}\frac{D}{L_0} \tag{4}$$

- The nominal frequency of a SJ actuator had to be established. Frequency can be calculated theoretically as:

$$f = \frac{3}{2\pi}\frac{D}{D_i}\sqrt{\frac{k_p}{\rho \cdot L_e}} \tag{5}$$

where D is the actuator orifice diameter; D_i is the inner diameter of the actuator; k_p is the stiffness of the actuator (latex membrane and loudspeaker membrane), $k_p = 2901628 \mathrm{N/m^3}$; ρ is the density of the working fluid, $\rho = 1000 \mathrm{kg/m^3}$ for water; L_e is the equivalent length of the orifice, $L_e = 6.74 \mathrm{mm}$.

The theoretically evaluated nominal frequency (eq.(5)) in the studied case is $f = 30.1 \mathrm{Hz}$.

3 Experimental Setup and Methods

The actuator (Fig. 1) consisted of an actuating part – loudspeaker (ARN-226-03/4Ω), cavity and nozzle. The actuator cavity was constructed from two aluminum

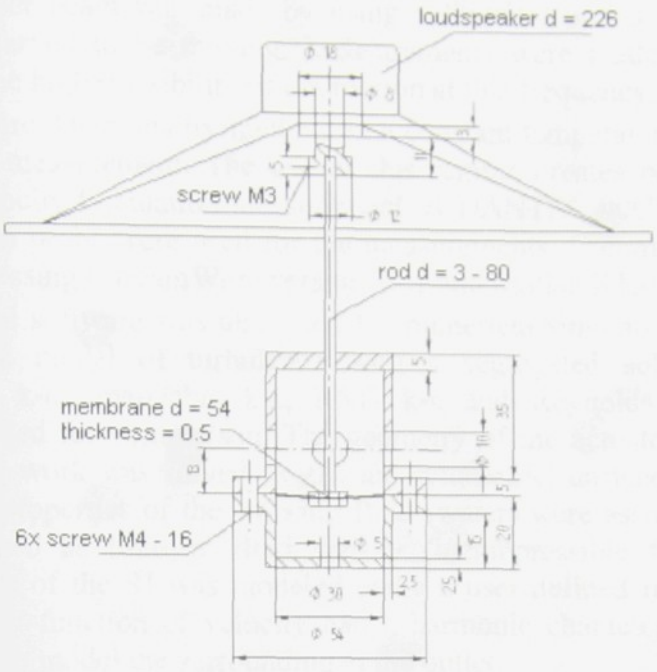

Figure 1: Schematic view of the actuator – actuating part and nozzle

components with an inner diameter of D_i = 30mm and a wall thickness of s = 2.5mm. Both of these components were furnished with flanges. A latex membrane, with a thickness of 0.5mm was placed between the flanges. This latex membrane was connected by an aluminum rod (d = 3mm, length=80mm) to the loudspeaker membrane. There were four holes with diameters of 8mm in the upper aluminum part - above the latex membrane. These four holes facilitated water flow and thereby, a partial compensation of hydrostatic pressure differences on the latex membrane. For a SJ measurement in water, the actuator (nozzle) orifice was oriented vertically downwards to the bottom of the tank. The inner dimensions of the tank were 1000mm x 1000mm x 1000mm.

The entire setup was connected together with the aluminum profiles. The positioning system was attached to these aluminum profiles. The equipment was secured on the upper edge of the tank.

The SJ was actuated by moving the latex membrane, which was connected to the loudspeaker membrane.

The loudspeaker was fed an amplified sinusoidal signal. All experiments were conducted with a constant electrical charge of P = 2.48W. The temperature of the water was uniform throughout the tank. It fluctuated slightly during the experiments within a range of 18°C to 22°C. It was approximately the same as the ambient air temperature in the laboratory.

For a first impression of the SJ, a Tin ions visualization was made. This method is based on the transfer of tin ions from an anode (a tin wire with a diameter of d = 5mm) to a cathode (copper plate) in an electrolytic solution (a mixture of water and common salt). The SJ actuator was placed into the electrolytic solution and a tin wire was fixed across the opening of the orifice. The tin ions detached from the anode after the wire was connected to a direct voltage source. These particles were visible as

a white "smoke". An ND:YV04 continuous wave laser was used for lighting. A laser sheet from the laser beam was made by using cylindrical optics. In this laser sheet, the ions were observed to be moving. Measurements were made at a frequency of f = 10Hz, due to the higher visibility of ion motion at this frequency.

The Hot-wire Anemometry method, in a constant temperature regime, was used for flow velocity measurement. The use of this regime creates better conditions for velocity and a velocity fluctuation measurement. A DANTEC 90C10 anemometer and Dantec 55R36 film probe were used for the measurements. Commercial software was used for data processing (StreamWare version 3.01 and Matlab R13).

Commercial software was also used for numerical simulations (Fluent 6.1.22). The Standard k-ε model of turbulence with a segregated solver was used for calculations. The k-ω, realizable k-ε, RNG k-ε and Reynolds Stress models of turbulence were used for comparison. The geometry of the actuator was generated in Gambit 2.1.6. The work was solved as 2D, axi-symmetric, unsteady. Mechanical and thermodynamical properties of the working fluid (water) were assumed to be constant and were prescribed as follows: fluid density (incompressible fluid) and dynamic viscosity. The inlet of the SJ was modeled using a user defined function of velocity. The time dependent function of velocity had a harmonic characteristic. The constant pressure was used to model the surrounding at the outlet.

4 Results and Discussion

4.1. Tin ions visualization

An Olympus E20P camera was used to photograph the "white smoke". Figure 2 shows the vortex ring formation near the orifice, as well as the second vortex, which has wafted from the orifice. Also visible is the decay of the third vortex. As noted above, the frequency for the visualization was f = 10Hz in order to make the structures visible.

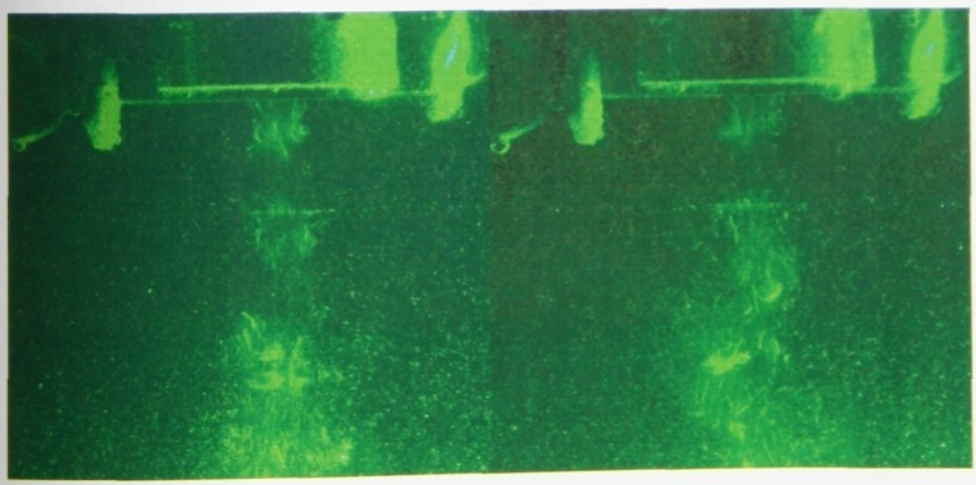

Figure 2: Tin ions visualization

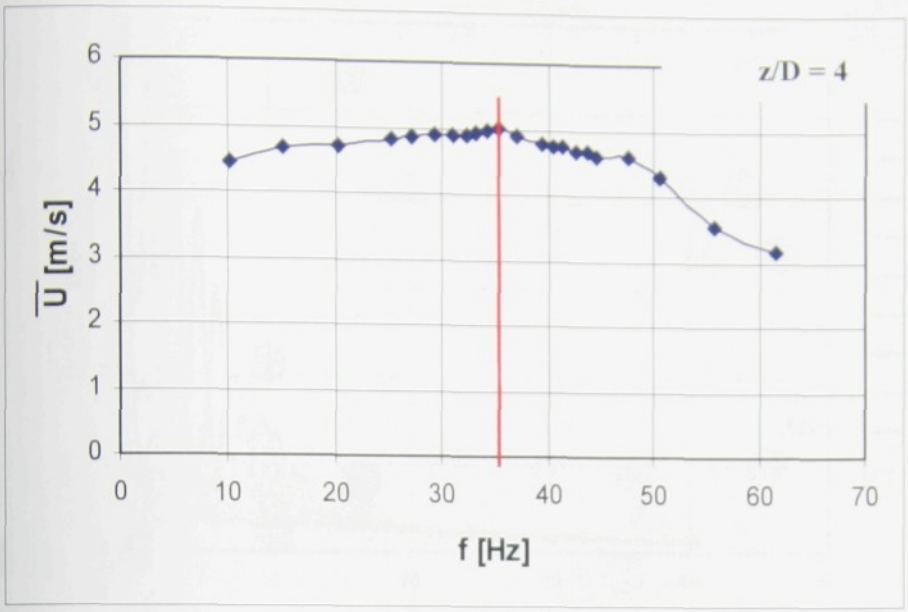

Figure 3: The dependence of the time-mean component of velocity on actuator frequency

4.2. Hot-wire Anemometry

As previously noted, the Constant Temperature regime of HWA was used for measurements. The nominal (resonance) frequency was scanned in a range from 10 to 65 Hz on the orifice axis. Figure 3 shows the measured values at a distance of z/d=4 at 2.48W of electrical power. The highest time-mean velocity (time-mean voltage) was found to exist at a frequency of f = 36 Hz.

Figure 4 shows the change in time-mean velocity $\bar{U}$ as a function of the distance z from the nozzle.

Figure 5 shows the time change in average velocity and time-mean velocities in

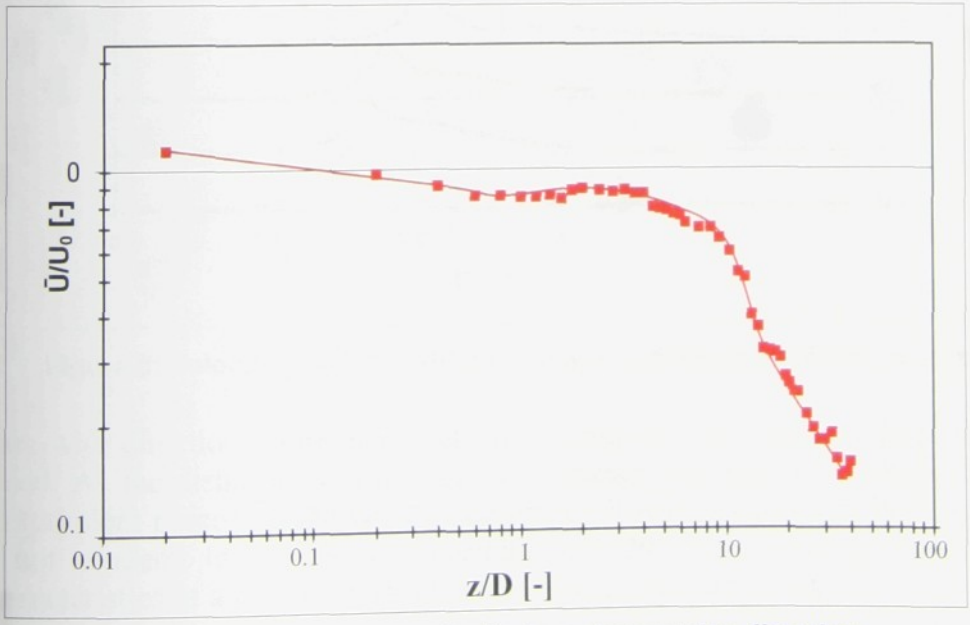

Figure 4: Change in time-mean velocity in a stream-wise direction (logarithmic scale)

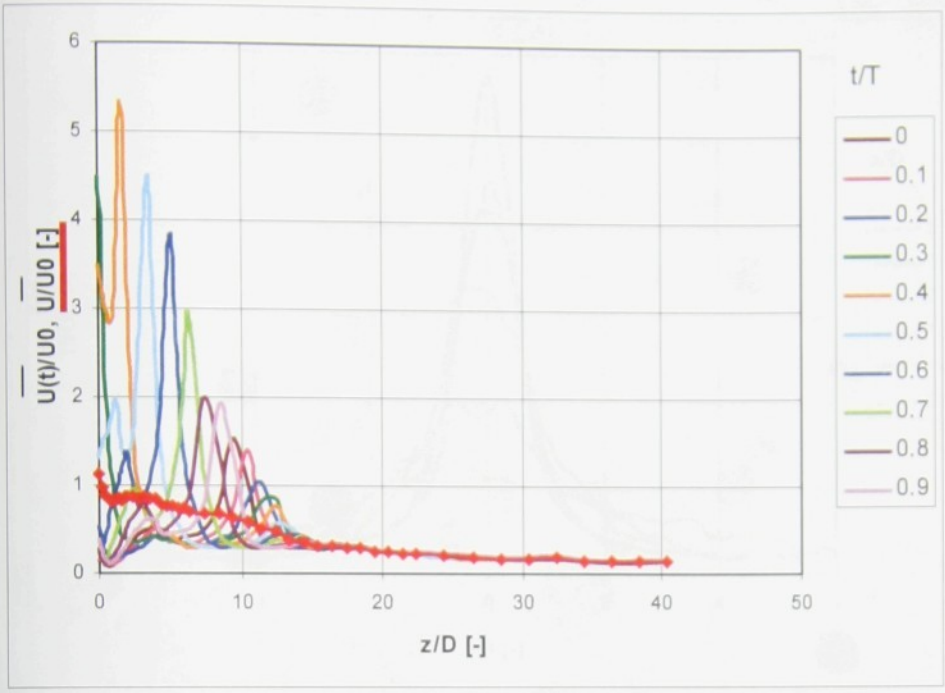

Figure 5: Dependence of average velocity in different times and time-mean velocity in a stream-wise distance

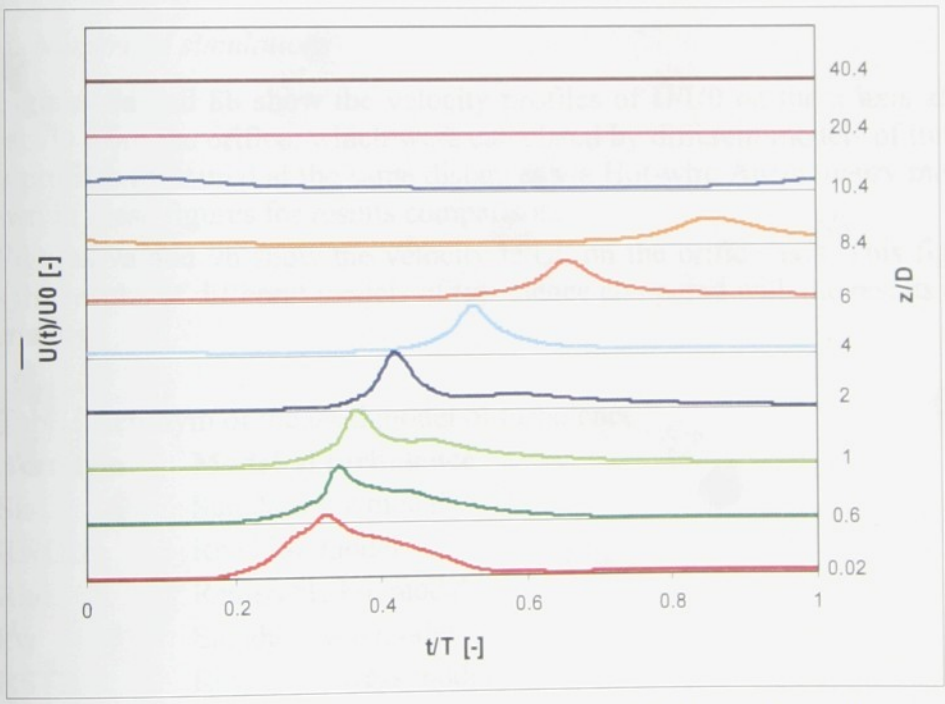

Figure 6: Velocity profiles at different times and distances from the nozzle

a stream-wise direction. Time-mean velocity decreased as the distance from the orifice increased. As the distance from the orifice increased, the vortex structures dissipated due to turbulent processes and velocity decreased It was obvious that flow oscillations were not evident in distances exceeding z/D=20. The existing flow took on the characteristics of a free jet from this point onward (see figure 6).

Velocity profiles were measured on the x axis at distances z/D = 2, 4, 7, 10 and 20 from the orifice. A comparison of time mean velocities $\bar{U}$ is shown on figure 7.

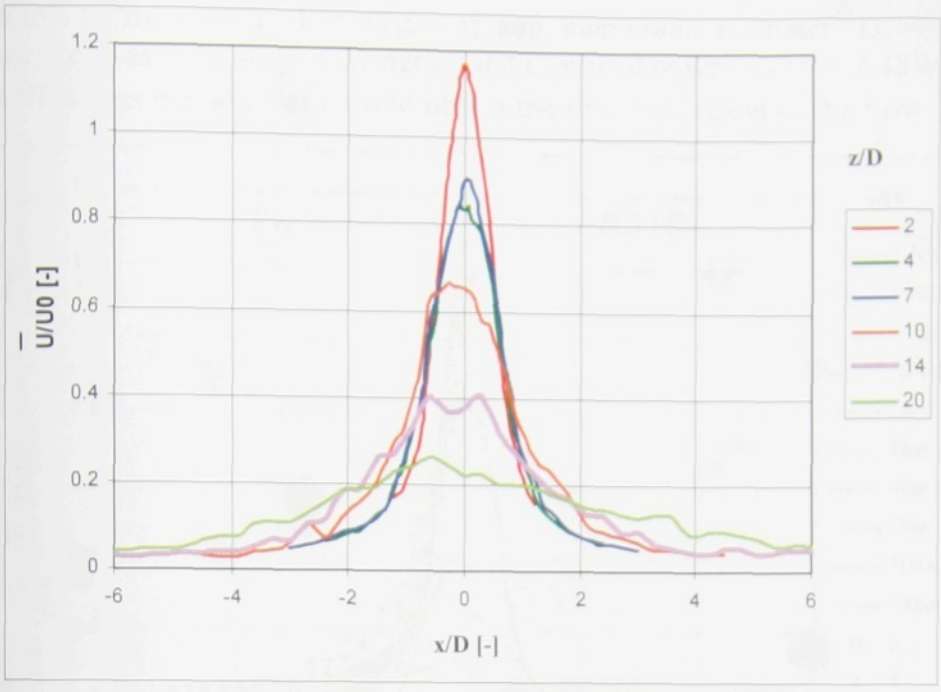

Figure 7: Velocity profiles $\bar{U}/U_0$

4.3. Numerical simulations

Figures 8a and 8b show the velocity profiles of Ū/U0 on the x axis at various distances z/D from the orifice, which were calculated by different models of turbulence. Velocity profiles measured at the same distances via Hot-wire Anemometry method are also shown in these figures for results comparison.

Figures 9a and 9b show the velocity Ū/U0 on the orifice axis. This figure also presents the results of different models of turbulence compared with the results of HWA measurements.

Tab.1: Acronym of the used model of turbulence

Acronym	**Model of turbulence**
Ske	Standard k-ε model
RNGke	RNG k-ε model
Rke	Realizable k-ε model
kw	Standard k-ω model
RSTR	Reynolds Stress model

5 Conclusions

The characteristics of a Synthetic Jet in water were investigated in this paper. A unique experimental setup was designed, and multiple experiments were conducted.

The actuator consisted of an actuating part - loudspeaker and actual nozzle. The main parameters of the nozzle were: orifice diameter, D = 5mm; distance from

the membrane to the orifice, l = 17.5mm; and membrane diameter, D_l = 30mm. The loudspeaker was fed a sinusoidal signal, and electrical power was P = 2.48W.

The Tin ions method was used to obtain the first impression of the flow. During

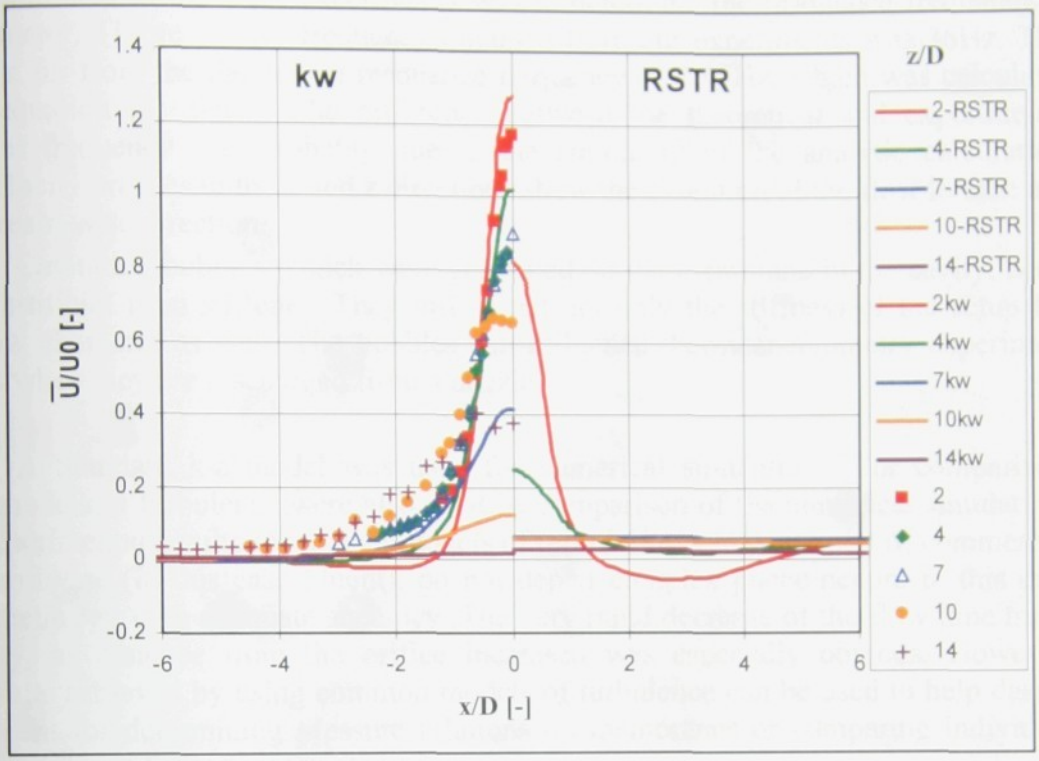

Figure 8a: Velocity profiles. Points correspond to measured values

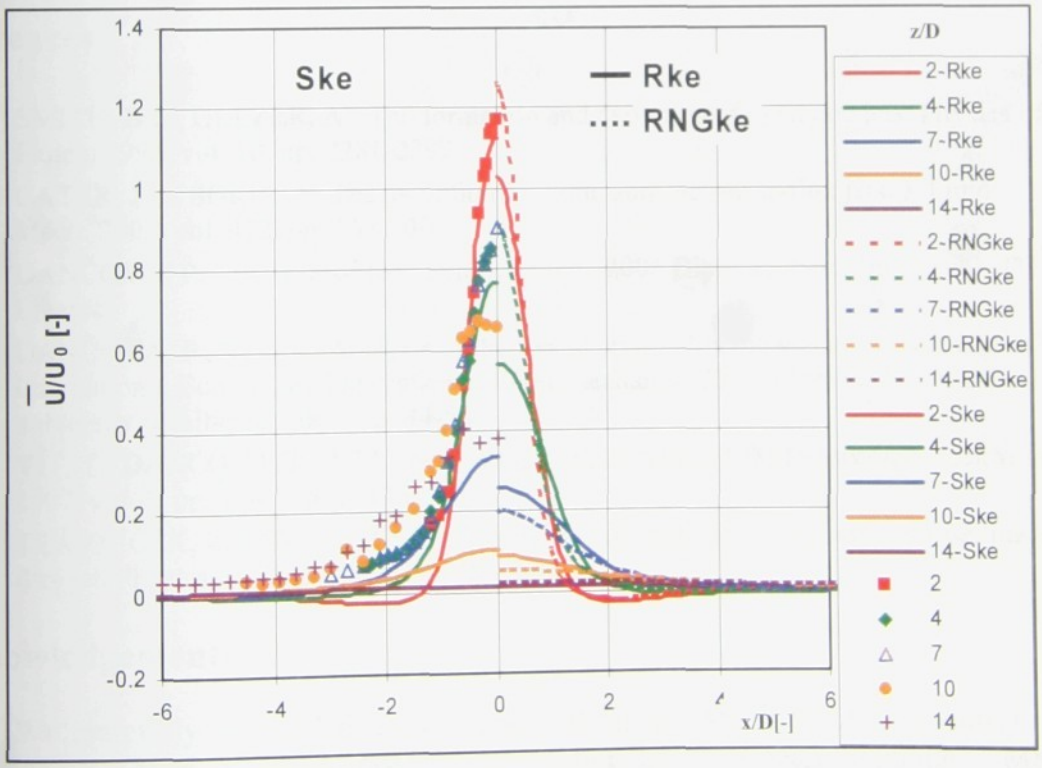

Figure 8b: Velocity profiles. Points correspond to measured values

the experiments it became clear that a Tin-ions visualization was not useful for velocities exceeding 0.5 m/s.

A thermoanemometry measurement revealed the velocity field in detail. The initial step of the CTA experiments was to determine the resonance frequency of the actuator. The resonance frequency obtained from our experiments was 36Hz. This was not far from the theoretical resonance frequency of 30.1Hz, which was calculated from equation (5) above. The difference between the theoretical and experimental nominal frequency was probably due to the simplicity of the analytic calculation. The velocity profiles in the x and z directions show the evolution of the flow in time and in a stream-wise direction.

Cavitation bubbles, which were generated on the membrane in the cavity, acted as an artificial fluid stiffener. They influenced not only the stiffness of the setup but the flow character as well. The bubbles can influence thermoanemometry experiment results when they are discharged from a nozzle.

A Standard k-ε model was used for numerical simulations. For comparison, other models of turbulence were also used. A comparison of the numerical simulations and experimental results shows that models of turbulence, which are part of commercial CFD software (in this case Fluent), do not depict complex phenomenon, in this case a Synthetic Jet, with adequate accuracy. The very rapid decrease of the flow time mean velocity, as distance from the orifice increased was especially obvious. However, the results achieved by using common models of turbulence can be used to help design equipment for determining pressure relations on membranes or comparing individual construction variants of an actuator.

References

1. SMITH, B.L., GLEZER, A.: The formation and evolution of synthetic jets. Physics of Fluids. 1998, vol. 10, pp. 2281-2297
2. CATER, J.E., SORIA, J.: The evolution of round zero-net-mass-flux jets. J. Fluid Mech. 2002, vol. 472, pp. 167-200
3. DANČOVÁ, P.: Analysis of the "Synthetic Jet". 2006 Diploma thesis (in Czech), TU Liberec
4. DANČOVÁ, P., VÍT, T.: Analysis of the "Synthetic Jet" in the water. Proceedings of International Conference Experimental Fluid Mechanics 2007. Liberec: Technical university of Liberec, 2007. pp. 44-50.
5. VÍT, T., DANČOVÁ, P., TRÁVNÍČEK, Z.: Synthetic Jet. MM Průmyslové spektrum. 2007, vol. 3, pp. 104-106 (In Czech)
6. TRÁVNÍČEK, Z., VÍT, T., TESAŘ, V.: Hybrid synthetic jet as the non-zero-net-mass-flux jet. Physics of Fluids. 2006, vol. 8, pp 1701-1–1701-4

Acknowledgements

We gratefully acknowledge the support of the GAASCR (IAA200760801) and the Research Target of the Ministry of Education of the Czech Republic - MSM 4674788501.

CHAPTER 8

HYBRID SYNTHETIC JET INTENDED FOR ENHANCED JET IMPINGEMENT HEAT/MASS TRANSFER

Authors: Z. Trávníček [a] T. Vít [b]

[a] *Institute of Thermomechanics, Academy of Sciences of the Czech Republic, Dolejškova 5, 182 00 Prague 8, Czech Republic*
[b] *Faculty of Mechanical Engineering, Technical University in Liberec, Hálkova 6, 461 17 Liberec, Czech Republic*

Published in:

In.: 13th International Heat Transfer Conference IHTC-13, Sydney, NSW Australia, Aug. 13-18, 2006, JET–15. Book of Abstracts, Begell House Inc. Publ.; CD-Conference Proceedings IHTC 13, Eds. G. de V. Davis and E. Leonardi, ISBN 1-56700-225-0 / CD 1-56700-226-9

Abstract

A possibility to enhance the "synthetic jet" has been studied. Instead of the typical zero-net-mass-flux synthetic jets, the non-zero-net-mass-flux hybrid synthetic jet was proposed. An additional volume rate is entrained (pumped) through a pair of auxiliary channels into the actuator cavity. Not any fluid supply is added from any external source (neither blower nor compressor are needed).

Three variants are experimentally studied, namely (a) the synthetic (zero-net-mass-flux) jet, (b) hybrid synthetic (non-zero-net-mass-flux) jet, and (c) continuous jet. Flow visualization, hot-wire measurement, and mass transfer measurement using the naphthalene sublimation technique have been performed.

The present experiments confirmed that the hybrid synthetic jet achieves higher extrusion volume flow rate in comparison with the common synthetic jets. An appreciable enhancement of the impingement heat/mass transfer was achieved. The main reason for the heat/mass transfer enhancement is the speedup of the time-mean flow by means of higher extrusion volume flow rate.

Nomenclature

CJ	continual (steady) jet
D	jet orifice diameter, D = 8 mm, (see Figure 1)
D_n	mass diffusion coefficient of naphthalene vapor in air
f	actuating frequency, Hz

h local heat transfer coefficient, W/m^2K

h_m local mass transfer coefficient, m/s

H orifice-to-wall spacing, (see Figure 1)

HSJ hybrid synthetic (non-zero-net-mass-flux) jet

L_{0A} extruded fluid column length, $U_{0A} T$

Nu local Nusselt number

Re_{SJ}, Re_{HSJ} Reynolds numbers of SJ and HSJ, respectively; $U_{0A} D/\nu$

Re_C Reynolds number of the continual jet, $U D/\nu$

Sh local Sherwood number, $h_m D/D_n$

St Strouhal number of the harmonic actuation, $(1/\pi)D/L_{0A}$

SJ synthetic (zero-net-mass-flux) jet

t time

T time period, $1/f$

T_E extrusion time

T_w wall temperature, K

$u_0(t)$ orifice velocity

U time-averaged velocity

U_f periodic component of the velocity

U_0, U_{0A} time-averaged orifice velocities, (see equations (1 and 2), respectively)

x axial coordinate, (see Figure 1)

1. Introduction

Impinging jets have been widely studied from the heat/mass transfer point of view. The most important results are collected in monographs, such as the outstanding book by Dyban and Mazur (1982), and the distinguished work by Martin (1977). Theoretical, experimental and numerical research of the topic has continued up to the present time – as presented, e.g., in the recent review by Garimella (2000) (who discussed his own results as well as 122 relevant references).

Despite the fact that continual (steady) impinging jets can achieve very high heat transfer onto exposed walls, utilization of pulsations can intensify the transport process even more. (However, the jet pulsations cannot enhance heat transfer automatically, the effect can be sometimes increasing, sometimes decreasing or little – see Herman (2000)). A promising alternative focusing on heat transfer augmentation can be based on "fully" oscillating flows, i.e. on zero-net-mass-flux synthetic jets.

Synthetic jets (SJs) are generated (synthesized) by pushing and pulling of fluid through an orifice, by the interactions within a train of vortices – see Smith and Glezer (1998). A time-mean mass flux of the oscillatory flow in this orifice is zero, therefore the other common expression is the zero-net-mass-flux jet. A typical SJ actuator consists of a sealed cavity bounded on one end by a wall with an emitting orifice or nozzle and on the other end by an actuating diaphragm or piston. Contemporary experimental and numerical investigations concerning the basic principles and applications are being carried out in papers – see e.g. Cater and Soria (2002), Glezer and Amitay (2002), Holman *et al.* (2005), Lee and Goldstein (2000), Mallinson *et al.* (2001), Gordon and Soria (2002), and Tesař and Zhong (2003). Several studies which focus on various operational characteristics as well as on actuators design – see e.g. Smith and Swift (2003), Gallas *et al.* (2003), and Gilarranz *et al.* (2005a, 2005b). SJs have many perspective applications, which can be divided into two distinct groups:

- Control of primary flows. SJs can be used for fluid jet (thrust) vectoring – Smith and Glezer (2002), active control of turbulence or flow separation both in external ((Amitay and Glezer (2002), Tensi *et al.* (2002), Mittal and Rampunggoon (2002), and Chen and Beeler (2002)) and internal (Ben Chiekh *et al.* (2003)) aerodynamics. Many other possible applications involve control of turbulence, flow separation, mixing and fluid flow regime in a variety of cases.

- Use of stand-alone SJ (or system of SJs) without any primary flow; a typical promising application is for cooling. One of the first investigations was briefly described by Yassour *et al.* (1986), more recent studies are Trávníček and Tesař (2003), and Kercher *et al.* (2003).

A classical *reciprocating (diaphragm or piston) pump* consists of a cavity which is connected to inlet and outlet pipes through one-way valves. It is desirable to substitute problematic mechanical valves with elements without movable parts; the reciprocating pump without mechanical valves is called the *valve-less pump*. Of course, the essential *rectification (or streaming) function* of the one-way valve has to be fulfilled – it is particularly possible by means of fluidic principles.

There are several known types of fluidic elements with the *rectification function* – see, e.g., an earlier review by Yastrebova (1971), or the paper by Priestman and Tippetts (1985). The rectification elements are frequently called "fluid diodes" (or "dynamic passive valves" – see Gerlach and Wurmus (1995)).

Rectification elements can be shaped as convergent/divergent ducts – these diffuser/nozzle elements with rectification effects were first described by Stemme and Stemme (1993). The prevailing fluid flow direction of these elements corresponds to the divergent flow. Similar rectification elements, but in quite different regime (prevailing direction corresponds to convergent flow, because of much higher duct angle and governing flow separations), was proposed by Gerlach and Wurmus (1995). Another rectification element (the so called Tesla-type) was developed and optimized by Williams and Forster (2001).

Recently the synthetic jet principle was combined with a periodic fluid pumping through a valve-less displacement pump, and the so called „*hybrid synthetic jet* (HSJ)" was proposed by Trávníček *et al.* (2004a), and sequentially studied by Trávníček *et al.* (2005a, 2005b). HSJ is generated partly from a train of individual vortical "puffs" by means of the mechanism of a common zero-net-mass-flux synthetic jet and, partly by means of the pumping function of the actuator cavity. The resulting HSJ is basically a non-zero-net-mass-flux one, and its volume flow rate as well as fluid momentum can be higher in comparison with a pure (zero-net-mass-flux) synthetic jet.

Recently, a similar combination of synthetic jet actuator with a valve-less pump was proposed by Luo and Xia (2005) to design a new synthetic-jet-based micropump. Another type of an actuator was proposed by Tesař *et al.* (2006): a fluidic (self-excited) flow oscillator without any moving components, which is supplied by the mean-flow from a compressor.

The present paper focuses on an impingement heat/mass transfer between a surface and fluid. An oscillation character of SJs is used to enhance the heat/mass transport process. Moreover, a non-zero-net-mass-flux character of HSJs is used to improve transport effects even more. Three variants of round impinging air jets are experimentally studied in this paper: (a) zero-net-mass-flux SJ, (b) non-zero-net-mass-

flux HSJ, and (c) the continuous jet (CJ). Flow visualization, hot-wire measurement, and mass transfer measurement using the naphthalene sublimation technique have been performed.

2. Experimental investigation

The synthetic round jets are characterized by two length scales – the length scale of the output orifice (diameter D), and the "stroke length" L_{0A} – see Smith and Glezer (1998), another name is the "equivalent extruded (fluid) column length" – see e.g. Tesař and Zhong (2003)); L_{0A} is defined from the time-mean orifice velocity over the extrusion (discharge) stroke: $L_{0A} = U_{0A}T$, where T is the time period, i.e. $T = 1/f$, where f is frequency. The time-mean orifice velocity U_{0A} can be defined either from the axial orifice velocity on the axis – Smith and Glezer (1998):

$$U_0 = \frac{1}{T}\int_0^{T_E} u_0(t)dt \tag{1}$$

or from the cross-stream velocity – see e.g. Cater and Soria (2002), Holman *et al.* (2005), and Smith and Swift (2003):

$$U_{0A} = \frac{1}{T}\int_0^{T_E}\left(\frac{1}{A}\int_0^{A} u_0(t,r)\cdot dA\right)\cdot dt, \tag{2}$$

where T_E is the extrusion time ($T_E = T/2$ at the sinusoidal waveform), and A is the cross-section area of the actuator orifice. Alternatively, the time-mean orifice velocity can be defined from the mean momentum of each pulse at the orifice exit plane – see Cater and Soria (2002).

The Reynolds number can be typically defined as $Re_{SJ} = U_{0A}D/\nu$ – see Smith and Glezer (1998). The Strouhal number is a slightly modified ratio of the length scales D and L_{0A}; at harmonic actuation $St = (1/\pi)\, fD/U_{0A} = (1/\pi)\, D/L_{0A}$.

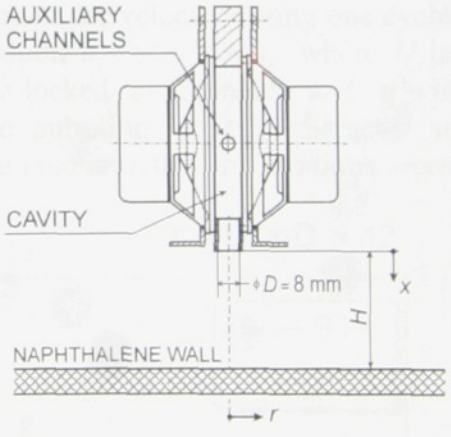

Fig. 1. The actuator and configuration tested in this study.

Figure 1 shows a schematic view of the present actuator and the configuration tested in this study. The actuator consists of a sealed cavity, which is equipped with an emitting orifice (diameter D = 8.0 mm) and with a pair of actuating diaphragms, running in the opposite direction. The orifice is oriented vertically downwards to the exposed wall 0.5 x 0.5 m in size. The working fluid is air. Instead of a typical SJ actuator design, the present actuator is equipped with a pair of auxiliary channels. They are perpendicular to the image plane of Figure 1, and their inner diameter is 5.0 mm. Due to this arrangement, one of three jets can be generated:

(a) zero-net-mass-flux SJ. For this purpose, the auxiliary channels are closed and SJ is generated similarly as in the previous studies by Trávníček *et al.* (2004b, 2005c,

2006). In the present study, the actuator was fed with sinusoidal current, and the input electrical power was kept constant 4.0 W.

(b) non-zero-net-mass-flux HSJ. The auxiliary channels are connected with the ambience via a pair of conical ducts to create the rectification effect. This idea was recently used to develop the coaxial HSJ actuator by Trávníček *et al.* (2004a, 2005a, 2005b). In the present study, the actuator was fed with sinusoidal current, and the input electrical power was kept constant 4.0 W (identically with SJ).

(c) The reference continual jet (CJ). The input electrical power into the actuator is zero, and the auxiliary channels are supplied by a compressor. The air flow passes through a flexible plastic tube, which is connected via T- adaptor to both auxiliary channels of the actuator. The flow rate is kept constant and measured by the rotameter. In the present study, the cross-stream velocity through the nozzle was $U = 9.9$ m/s (i.e. the Reynolds number $Re_C = UD/\nu = 4\,900$ and 5030 for the hot-wire and mass transfer experiments, respectively).

The smoke-wire technique was used for flow visualization Trávníček and Tesař (2003), Trávníček *et al.* (2005b). The phase-locked flow field pattern (streaklines, diffused because of the flow turbulence) were observed under stroboscope light synchronized with excitation frequency, and pictures were taken by digital camera (described in detail in Trávníček and Tesař (2003)).

The velocity distribution was measured by the hot-wire anemometer system DANTEC (StreamLine 90N10) in the constant temperature mode, by the single-sensor wire probe (55P11). The typical sampling frequency and number of samples were 15 kHz and 131 072, respectively. The phase averaging of the velocity during one cycle was carried out by means of the velocity decomposition $u = U + U_f + u'$, where U is the time-mean velocity, U_f is the periodic phase-locked component, and u' is the fluctuation component. Taking into account the pulsating velocity character at the actuator orifice, positive (extrusion) and negative (suction) flow orientations were assumed and the velocities during the suction stroke were inverted to reflect the flow direction (the same approach as Smith and Glezer (1998):

Local mass transfer was measured using the naphthalene sublimation method (Trávníček and Tesař (2003), Goldstein and Cho (1995)) and the local mass transfer coefficient was calculated from the sublimation depth as

$$h_m = \frac{\rho_n R_n T_w \Delta x}{p_{sat} \Delta t} \qquad (3)$$

where ρ_n is the density of solid naphthalene, R_n is the gas constant for naphthalene, T_w is

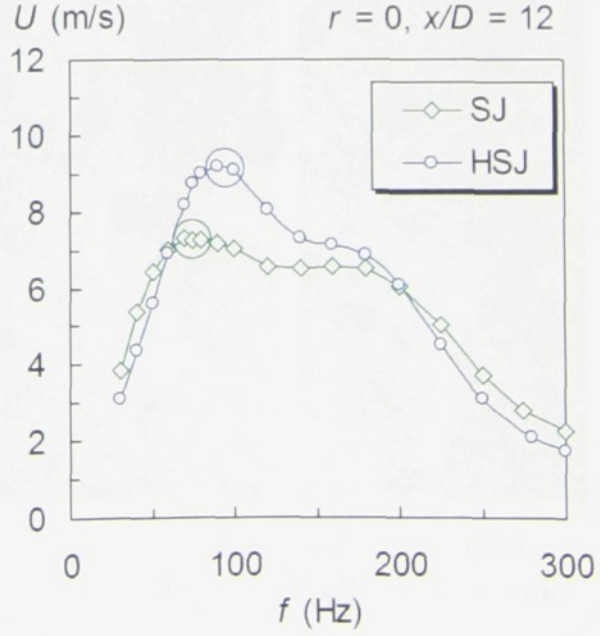

Fig. 2. Frequency characteristics.

the surface temperature, Δx is the net local sublimation depth, p_{sat} is the saturated vapor pressure of naphthalene at T_w (Goldstein and Cho (1995)), and Δt is the run duration.

The non-dimensional expression of the mass transfer coefficient is the Sherwood number, $Sh = h_m D/D_n$, where D_n is the mass diffusion coefficient of naphthalene vapor in air, calculated for measured temperature and pressure (Goldstein and Cho (1995)). Uncertainty analysis was performed according to Kline and McClintock's (1953) method for a single sample experiment. The uncertainty of the mass transfer coefficient and the Sherwood number is within 6% and 9%; more detailed description of the experimental method and uncertainties were written by Trávníček and Tesař (2003).

Mass transfer data can be transformed to predict the heat transfer using the *heat/mass transfer analogy* – see e.g. Dyban and Mazur (1982), and Goldstein and Cho (1995):

$$\frac{Sh}{Re^m Sc^n} = \frac{Nu}{Re^m Pr^n}, \tag{4}$$

where Nu, Pr and Sc are the Nusselt, Prandtl, and Schmidt numbers, respectively; h is the local heat transfer coefficient, and k is the thermal conductivity. The values of the exponents m and n, which are usually accepted at continuous impinging jets, range 0.5–0.8 and 0.33–0.42, respectively.

3. Results and discussion

Figure 2 shows the frequency characteristics of the actuator for SJ and HSJ generations. The hot-wire measurement was performed on the axis ($r = 0$). The measurement was made rather far from the actuator ($x/D = 12$), where the velocity is always positive, as is discussed below. The maximum time-mean velocity was achieved approximately at 75 Hz and 95 Hz for SJ and HSJ, respectively. The value 75 Hz of SJ agrees well with the recent theoretical prediction of the present SJ actuator resonance – see Trávníček *et al.* (2004b), the value 95 Hz of HSJ is in tune with the resonance derivation by Trávníček *et al.* (2005a). Hence, the *"nominal operating points"* of the present study were chosen 75 Hz and 95 Hz

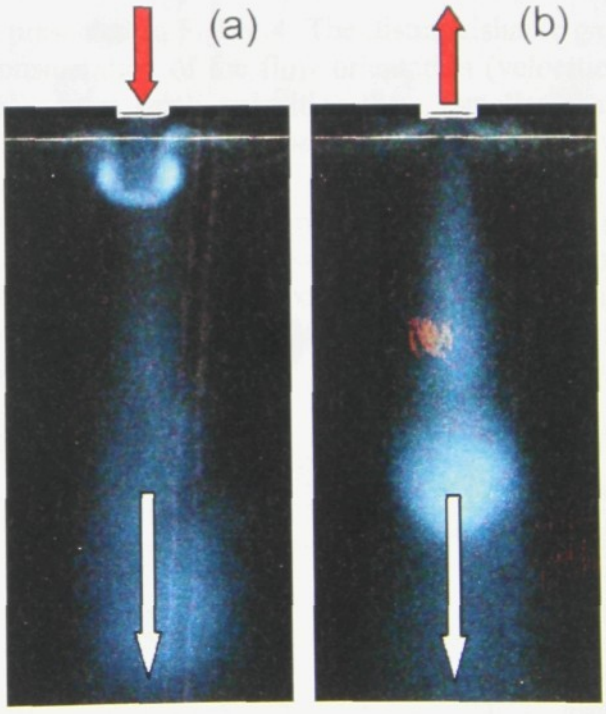

Fig. 3. Smoke visualization of SJ
a- displacement stroke, b- suction stroke.

for SJ and HSJ cases, respectively. These *"nominal operating points"* are presented in Figure 2 as two circles, and the measurements of flow field and mass transfer in the following text are performed at these frequencies.

A proper actuation was demonstrated using the flow visualization. Figure 3 demonstrates SJ at two typical patterns of the actuation period: the extrusion (displacement) and suction strokes, respectively (to smooth out the deviations of the individual cycles, Figure 3 shows multiple exposures of 75 pictures). An extrusion of fluid through the actuator orifice, and formation of the large vortex structure near the nozzle is well visualized in Figure 3(a). Later, this large vortex structure moves downstream independently of the local situation at the orifice, where the flow orientation is reversed – Figure 3(b) shows the suction of the external fluid from the vicinity of the orifice into the actuator cavity.

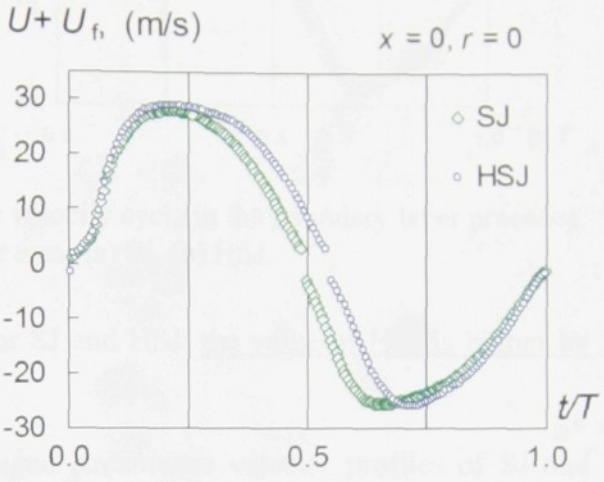

Fig. 4. Centerline phase averaged velocity during one cycle of SJ and HSJ.

Hot-wire measurement in the actuator orifice exit plane began with a preliminary traversing along two perpendicular diameters. Quite good axi-symmetry of the jet was concluded. Then the centerline velocity cycle was measured at $x = 0$, $r = 0$, and the results of the phase averaging (approximately 690 and 850 cycles for SJ and HSJ, respectively) are presented in Figure 4. The distinguishable gap around zero velocity results from the consideration of the flow orientation (velocities during the suction stroke were inverted), from small velocities there (smaller than the calibration range), and from high turbulence level (especially during the flow deceleration around $t/T = 0.5$).

Figure 4 demonstrates that the simplified consideration of sinusoidal actuation is rather far from the real situation. The real experimental waveform of the centerline velocity is not a precise sinusoidal function. Moreover, the extrusion times of SJ and HSJ are different from the half-period: $T_E/T = 0.49$ for SJ and 0.55 for HSJ. Integrations of this waveforms give the time-averaged orifice velocities; according to

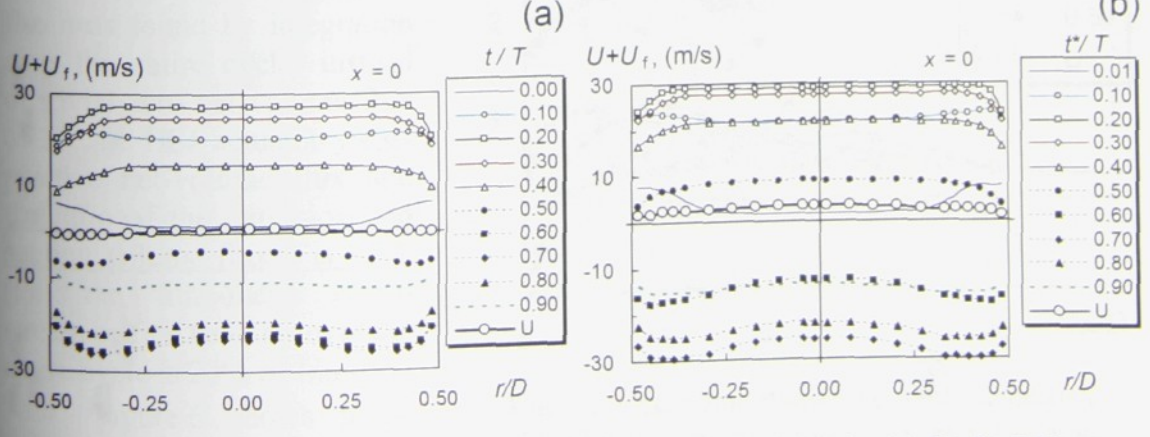

Fig. 5. Velocity profiles across the orifice exit during one cycle; (a) SJ, (b) HSJ.

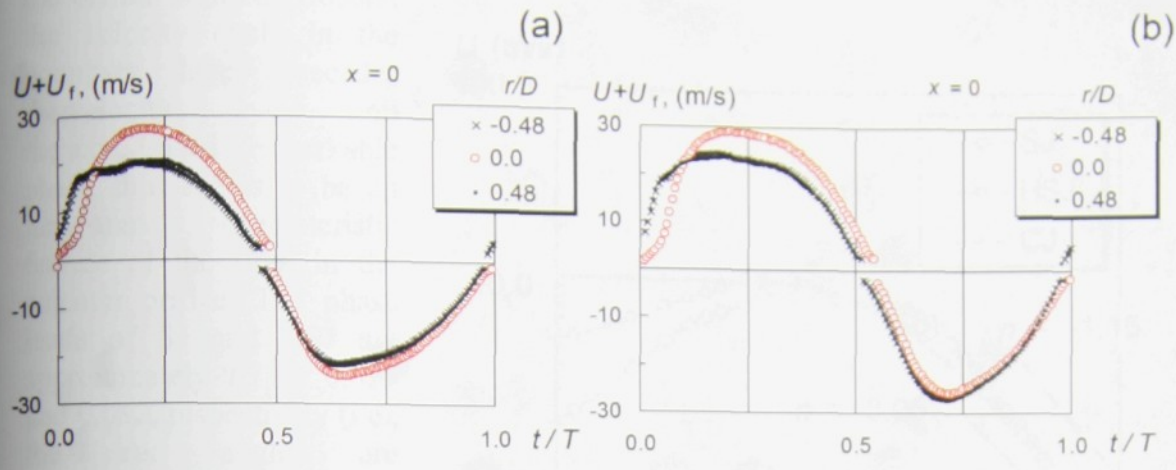

Fig. 6. Phase shift of the velocity cycles: the velocity cycle in the boundary layer precedes the velocity cycle on the axis; (a) SJ, (b) HSJ.

equation (1), U_0 = 8.9 m/s and 10.8 m/s for SJ and HSJ: the value of HSJ is higher by 22%.

Figure 5 compares the phase averaged streamwise velocity profiles of SJ and HSJ across the orifice exit. The time-mean velocity profile is also plotted in Figure 5. Evidently, the profiles are different from the simple quasi-steady model, when the common top-hat steady profiles are multiplied by a sinusoidal function in time. Integrations of the velocity profiles according to equation (2) give the time-mean cross-stream orifice velocities U_{0A} = 8.3 m/s and 10.4 m/s for SJ and HSJ: the value of HSJ is higher by 25% (!) Further relevant parameters are:

- for SJ: Re_{SJ} = 4 100, L_{0A}/D = 14.1, and St = 0.023,
- for HSJ: Re_{HSJ} = 5 100, L_{0A}/D = 13.8, and St = 0.023.

Further, the net-volume flux was found by integration over the entire cycle: instead of trivial zero net-volume flux of SJ, the HSJ actuator yields positive net-volume flux and the ratio of the extrusion and suction volume fluxes is 1.30, (i.e. the time-mean cross-stream orifice velocity over the entire cycle is 23% of U_{0A}).

Figure 6 shows phase averaged velocity on the axis and in the boundary layer at

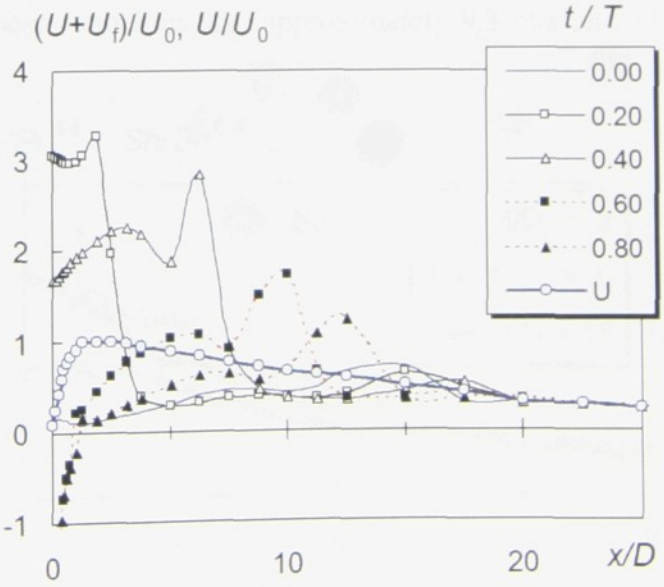

Fig. 7. Centerline phase averaged velocities of SJ during the actuating cycle, and the time-mean centerline velocity.

the orifice wall. Obviously, the velocity cycle in the boundary layer precedes the velocity cycle on the axis. This remarkable phase shift seems to be an important characteristic feature of the flow in the actuator orifice. The phase leads of SJ and HSJ are approximately $t/T = 0.025$ and 0.032, respectively (i.e., the lead angles are approximately 9.5° and 12°, respectively).

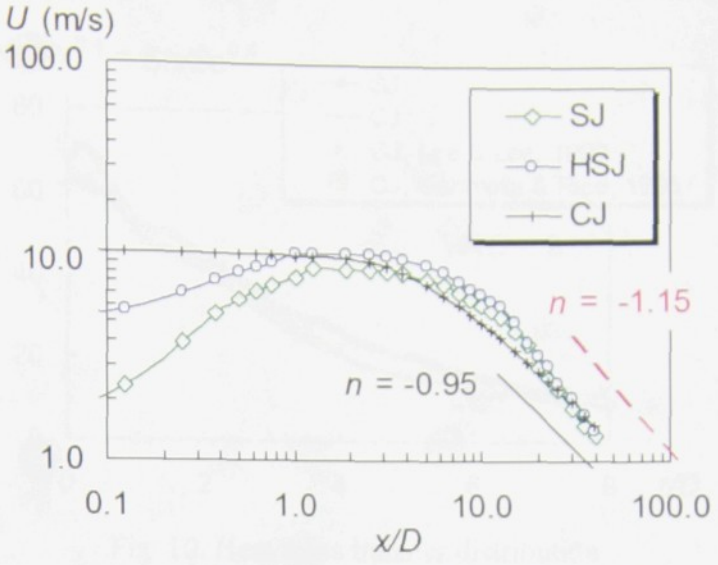

Fig. 8. Time-mean centerline velocity decay along the axis

Figure 7 shows the centerline phase averaged velocities during the actuating cycle of SJ; the time-mean velocity U is also plotted in Figure 7. The maximum velocity in the orifice was approximately $3.05U_0$, and the highest value was nearly $3.5U_0$ for $x/D = 2.5$. The range of the actuator suction was approximately $x/D = 1.1$, (further downstream only a positive orientation of the x velocity component exists during the cycle). The periodic character is clearly distinguishable approximately up to x/D=17–20. Further downstream, the initially pulsatile jet remains a conventional (steady) fluid jet with a monotonously decreasing streamwise time-mean velocity.

Figure 8 shows the streamwise variation of the time-mean velocity along the jet centerline. Firstly, the time-mean velocities of SJ an HSJ gradually increases from the actuator (from zero velocity of SJ, and from non-zero velocity of HSJ) – the jets are synthesized. The maximum time-mean velocities are approximately 9.3 m/s and 11.2 m/s for SJ and HSJ, respectively, at $x/D = 1$ to 3. Further downstream, the velocity gradually decreases. After a transition range and downstream $x/D > 15$–20, the velocity decays for SJ and HSJ fulfil the proportionality $U \sim (x/D)^n$ with the exponent approximately $n = -1.15$. The described results are in accordance with discussions of SJ from Trávníček *et al.* (2004b, 2005c): SJ from the present actuator starts to be

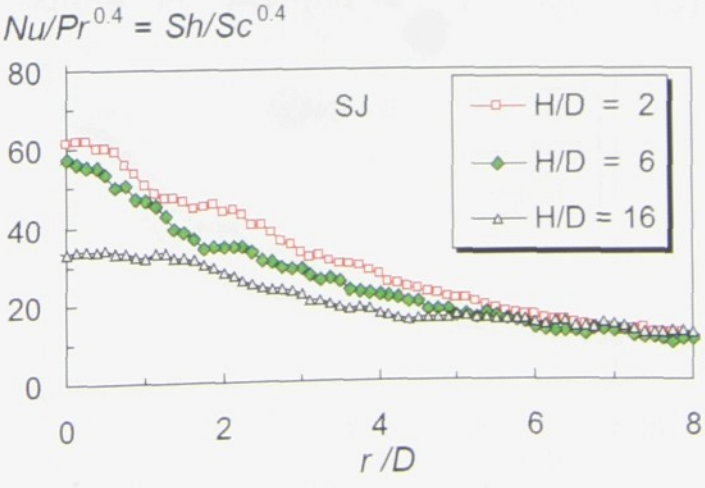

Fig. 9. Local heat/mass transfer onto exposed wall for SJ impingement

effectively non-periodic from $x/D > 15–20$.

The time-mean velocity of CJ starts at approximately 11.2 m/s at $x/D = 0$. This velocity very slowly decreases along the jet core up to 10.2 m/s at $x/D = 2.5$. More downstream the slope visibly increases; this behavior of CJ agrees with the well known streamwise velocity decay of the conventional (steady) axisymmetric fully developed turbulent jets with $U \sim x/D^{-1.0}$ (in fact, the present CJ exhibits a bit smaller slope with $n \sim -0.95$, which can manifest still not fully developed CJ).

Figure 9 presents three profiles of the mass transfer measurement at $H/D = 2$, 6 and 16 (because of the satisfactory symmetry, the curves were evaluated by averaging the two halves of each experimental profile). Following the heat/mass transfer analogy equation (4), the mass transfer data were recalculated into the ratio of $Nu/Pr^{0.4} = Sh/Sc^{0.4}$ to predict heat transfer distribution. According to our expectation, the highest heat/mass transfer occurs in the stagnation point on the axis, and increasing orifice-to-wall spacing H/D causes a reduction of the heat/mass transfer.

All three distributions from Figure 9 decrease monotonously with the radial distance

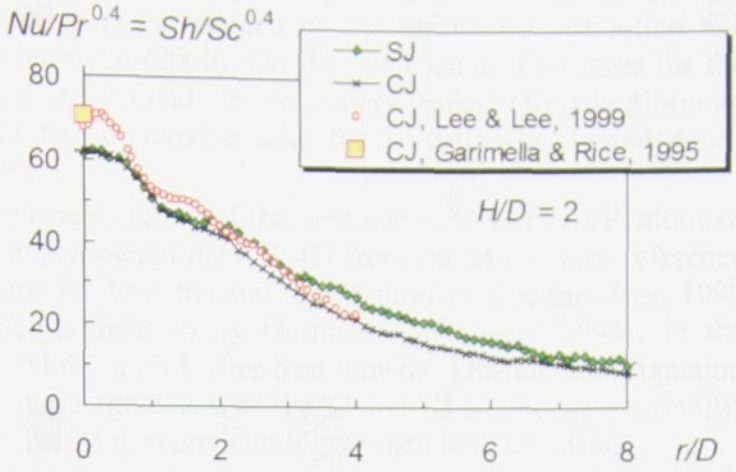

Fig. 10. Heat/mass transfer distribution - comparison with literature; $Re_{SJ} = 4200$, $Re_C = 5000$.

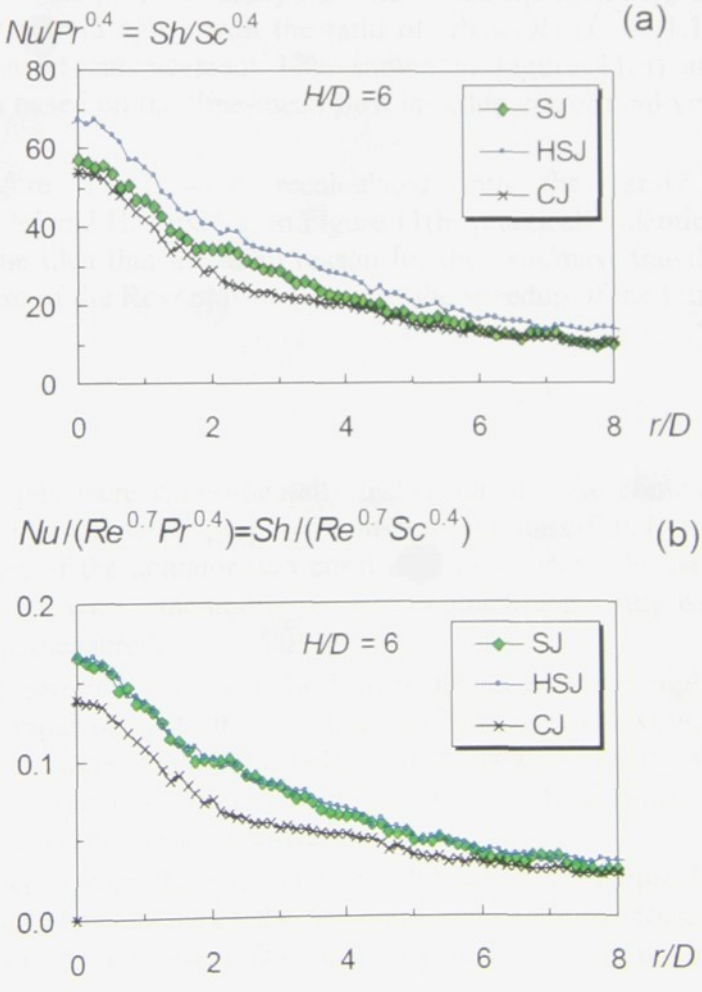

Fig. 11. Local heat/mass transfer distribution at $Re_{SJ} = 4200$, $Re_{HSJ} = 5300$, and $Re_C = 5000$.

from the stagnation point as bell-shaped curves. The so-called "secondary peaks" of the heat transfer distribution do not occur distinctly in Figure 9. It is in agreement with the literature: the secondary peaks may be reduced by the turbulence promotion and periodic excitations – see e.g. Garimella (2000). On the other hand, the curves for the orifice-to-wall spacing $H/D = 2.5$ and 6 trend the "secondary peaks" effect in places of radius $r/D \sim 2.0$, which could be comparable with the so-called "saturated zone" according to Lee and Lee, (1999).

Figure 10 compares the present results of the heat/mass transfer distributions of SJ and CJ at $H/D = 2$ with the experimental data for CJ from literature. Two reference experiments are plotted in Figure 10: heat transfer distribution by Lee and Lee, 1999 and the stagnation heat transfer correlation by Garimella and Rice (1995). In the stagnation area both references exhibit a bit higher heat transfer. Outside the stagnation area (for $r > 0.7D$), a relatively good agreement of the SJ and CJ can be stated; finally, in the wall-jet region for $r > 3D$, the SJ data are a bit bigger then both CJ- data.

Figure 11(a) compares the heat/mass transfer distributions of SJ, HSJ and CJ at $H/D = 6$. The highest heat/mass transfer was achieved by HSJ - the enhancement in the stagnation point of HSJ against SJ is 17 %. We can deduce that this enhancement results from the time mean-velocity increase: Taking into consideration the Reynolds number effect in a general form of the proportionality $Nu \sim Re^{0.7}$ (see equation (4)), the heat/mass transfer enhancement should agree with the ratio of $(Re_{HSJ}/Re_{SJ})^{0.7} = 1.17$. The experimental heat/mass transfer enhancement 17% shown in Figure 11(a) and the heat/mass transfer prediction based on the time-mean flow speedup correspond very well each other.

The results from Figure 11(a) were recalculated into the ratio of $Nu/(Re^{0.7}Pr^{0.4}) = Sh/(Re^{0.7}Sc^{0.4})$. SJ and HSJ exhibit in Figure 11(b) practically identical curves. It supported very well the idea that the main reason for the heat/mass transfer enhancement is really the increase of the Reynolds number, i.e. the speedup of the time-mean flow.

4. Conclusions

Two synthetic round air jets were experimentally tested, namely the common zero-net-mass-flux synthetic jet, and the newly proposed non-zero-net-mass-flux hybrid synthetic jet. The proper function of the actuator was confirmed experimentally using the flow visualization and hot-wire anemometry. For comparison purposes, the continual (steady) jet was also measured.

Hot-wire measurement confirmed that the hybrid synthetic jet achieves higher extrusion volume flow rate in comparison with the common synthetic jets. The volume flux increase results from the entrainment (pumping) effect of the actuator cavity and streaming effect of its auxiliary channels – not any fluid supply was added from any external source (neither blower nor compressor were needed).

Mass transfer measurement using the naphthalene sublimation technique has been performed. An appreciable enhancement of the impingement heat/mass transfer was achieved. Obviously, the enhancement results from the increase of the volume flow of the hybrid synthetic jet.

Acknowledgement

We gratefully acknowledge the support of the Grant Agency CR (projects no. 101/05/2681).

References

1. Amitay, M., and Glezer, A., 2002, Controlled transients of flow reattachment over stalled airfoils, Int. J. Heat Fluid Flow, 23, 690–699.
2. Ben Chiekh, M., Béra, J.C., and Sunyach, M., 2003, Synthetic jet control for flows in a diffuser: vectoring, spreading and mixing enhancement. J. Turbulence, 4, No. 032.
3. Chen, F-J., and Beeler, G.B., 2002, Virtual shaping of a two-dimensional NACA 0015 airfoil using synthetic jet actuator, AIAA Paper 2002-3273.
4. Cater, J.E., and Soria J., 2002, The evolution of round zero-net-mass-flux jets. J. Fluid Mech., 472, 167–200.
5. Dyban, E.P. and Mazur, A.I., 1982, Convection Heat Transfer in Impinging Jets (Konvektivnyj teploobmen pri strujnom obtekanii tel), 1st ed., Naukova dumka, Kiev, 1982 (in Russian).
6. Gallas, Q., Holman, R., Nishida, T., Carroll, B., Sheplak, M., and Cattafesta, L., 2003, Lumped element modeling of piezoelectric-driven synthetic jet actuators, AIAA J., 41, (2), 240–247.
7. Garimella S.V., 2000, Heat transfer and flow fields in confined jet impingement, Annu. Rev. Heat Transfer, XI, 413–494.
8. Garimella S.V., Rice, R.A., 1995, Confined and submerged liquid jet impingement heat transfer, Trans. ASME J. Heat Trans., 117, 871–877.
9. Gerlach, T., and Wurmus, H., 1995, Working principle and performance of the dynamic micropump, Sensors and Actuators A, 50, 135–140.
10. Gilarranz, J.L, Traub, L.W., and Rediniotis, O.K., 2005a, A new class of synthetic jet actuators – Part I: Design, fabrication and bench top characterization, Trans. ASME J. Fluids Eng., 127, 367–376.
11. Gilarranz, J.L, Traub, L.W., and Rediniotis, O.K., 2005b, A new class of synthetic jet actuators – Part II: Application to flow separation control, Trans. ASME J. Fluids Eng., 127, 377–387.
12. Glezer, A., and Amitay, M., 2002, Synthetic jets, Annu. Rev. Fluid Mech., 34, 503–529.
13. Goldstein, R.J., and Cho, H.H., 1995, A review of mass transfer measurements using naphthalene sublimation. Exp. Thermal Fluid Sci., 10, 416–434.
14. Gordon, M., and Soria J., 2002, PIV measurements of a zero-net-mass-flux jet in cross flow, Exp. Fluids, 33, (6), 863–872.
15. Herman, C., 2000, The impact of flow oscillations on convective heat transfer, Annu. Rev. Heat Transfer, XI, 495–562.
16. Holman, R., Utturkar, Y., Mittal, R., Smith, B.L, and Cattafesta, L., 2005, Formation criterion for synthetic jets, AIAA J., 43 (10) 2110–2116.
17. Kercher, D.S., Lee, J.-B., Brand, O., Allen, M.G., and Glezer, A., 2003, Microjet cooling devices for thermal management of electronics, IEEE Transactions on Components and Packaging Technologies, 26, (2), 359–366.
18. Kline S.J., and McClintock F.A., 1953, Describing uncertainties in single-sample experiments, Mechanical Engineering, 75, 3–8.
19. Lee, C.Y., and Goldstein, D.B., 2000, Two-dimensional synthetic jet simulation, AIAA Paper 2000-0406.
20. Lee, J., and Lee, S.J., 1999, Stagnation region heat transfer of a turbulent axisymmetric jet impingement, Exp. Heat Transfer, 12, (2), 137–156.
21. Luo, Z-B., and Xia, Z-X, 2005, A novel valve-less synthetic-jet-based micro-pump. Sensors and Actuators A, 122, 131–140.
22. Mallinson, S.G., Reizes, J.A., and Hong, G., 2001, An experimental and numerical study of synthetic jet flow, The Aeronautical Journal, 105, (1043) 41–49.

23. Martin, H., 1977, Heat and mass transfer between impinging gas jets and solid surfaces, Advances in Heat Transfer, 13, 1–60.
24. Mittal R., and Rampunggoon P., 2002, On the virtual aeroshaping effect of synthetic jets, Phys. Fluids, 14, 1533–1536.
25. Priestman, G.H., and Tippetts, J.R., 1985, Factors affecting the application of vortex diodes and throttles. In: Symposium Fluid Control and Measurement (FLUCOME), edited by M. Harada, Pergamon, Oxford, 241–246.
26. Smith, B.L. and Glezer, A., 1998, The formation and evolution of synthetic jets, Phys. Fluids, 10, 2281–2297.
27. Smith, B.L., and Glezer, A., 2002, Jet vectoring using synthetic jets, J. Fluid Mech., 458, 1–34.
28. Smith, B.L., and Swift, G.W., 2003, A comparison between synthetic jets and continuous jets, Exp. Fluids, 34, 467–472.
29. Stemme, E., and Stemme, G., 1993, A valve-less diffuser/nozzle-based pump, Sensors and Actuators A, 39, 159–167.
30. Tensi, J., Boué, I., Paillé, F., and Dury, G., 2002, Modification of the wake behind a circular cylinder by using synthetic jets, J. Visualiz., 5 (1) 37–44.
31. Tesař, V., Hung, C-H., and Zimmerman, W.B., 2006, No-moving-part hybrid-synthetic jet actuator, Sensors and Actuators A, 125, (2), 159–169.
32. Tesař, V., and Zhong, S., 2003, Efficiency of synthetic jets generation, Trans. Aeronaut. Astronaut. Soc. Repub. China, 35, (1), 45–53.
33. Trávníček, Z., Fedorchenko, A.I., and Wang, A-B., 2004a, An enhancement of synthetic jets by means of an integrated valveless pump. In: 10th Asian Congress of Fluid Mechanics (ACFMX), Ed. J. J. Wijetunge, May 17–21, 2004, Peradeniya, Sri Lanka; Book of Abstracts; full text is on the CD-ROM, 535–540.
34. Trávníček, Z., Fedorchenko, A. I., and Wang, A-B., 2005a, Enhancement of synthetic jets by means of an integrated valve-less pump, Part I: Design of the actuator, Sensors and Actuators A, 120, (1), 232–240.
35. Trávníček, Z., Hyhlík, T., Maršík, F., 2006, Synthetic jet impingement heat/mass transfer. Journal of Flow Visualization and Image Processing (in press).
36. Trávníček, Z., Maršík, F., Vít, T., and de Boer, P., 2004b, Synthetic jets actuation at the resonance frequency, In: 21st International Congress of Theoretical and Applied Mechanics (ICTAM), Eds. W.Gutkowski, T.A.Kowalewski, August 15-21, 2004, Warsaw, Poland; Book of Abstracts p. 113, extended abstract CD-ROM.
37. Trávníček, Z., and Tesař, V., 2003, Annular synthetic jet used for impinging flow mass–transfer, Int. J. Heat Mass Transfer, 46, 3291–3297.
38. Trávníček, Z., Tesař, V., and Wang, A-B., 2005b, Enhancement of synthetic jets by means of an integrated valve-less pump, Part II: Numerical and experimental studies. Sensors and Actuators A, 125, (1), 50–58.
39. Trávníček, Z., Vogel, J., Vít, T., and Maršík, F., 2005c, Flow field and mass transfer experimental and numerical studies of a synthetic impinging jet. In.: 4th International Conference on Heat Transfer, Fluid Mechanics and Thermodynamics (HEFAT2005), Eds. J.P. Meyer and A.G. Malan, Sep. 19 -22, 2005, Cairo, Egypt, No. ZT4.
40. Williams, B.E., and Forster, F.K., 2001, Micropump design for optimum pressure/flow characteristics. ASME Int. Mechanical Engineering Congress & Exposition IMECE2001/MEMS-23891, New York.
41. Yastrebova, E.V., 1971, Fluid diodes (review), Automatika i Telemechanika, 3, 101–106, (in Russian).
42. Yassour, Y., Stricker, J., and Wolfshtein, M., 1986, Heat transfer from a small pulsating jet, Proceedings of the 8th International Heat Transfer Conference, Vol. 3, Hemisphere Publ., San Francisco, USA, 1183–1186.

CHAPTER 9

HEAT/MASS TRANSFER OF THE PULSATILE IMPINGING JETS

Authors: Z. Trávníček[1], T. Vít[2], T. Hyhlík[3], F. Maršík[1]

[1] *Institute of Thermomechanics, Academy of Sciences of the Czech Republic, Dolejškova 5, 182 00 Prague 8, Czech Republic*
[2] *Faculty of Mechanical Engineering, Technical University in Liberec, Hálkova 6, 461 17 Liberec, Czech Republic*
[3] *Faculty of Mechanical Engineering, Czech Technical University in Prague, Technická 4, 166 07 Prague 6, Czech Republic, tomas.hyhlik@fs.cvut.cz*

Published in:

5th International Symposium on Turbulence, Heat and Mass Transfer (THMT-5), Dubrovnik, Croatia, Sept. 25-29, 2006, Book of extended abstracts 12.3., Eds. K.Hanjalič, Y.Nagano, and S.Jakirlič, Begell House Inc., New York., pp. 437–440; ISSN 961-91393-0-5

Abstract

The present study focuses on the pulsatile round impinging jets. To enhance impingement heat/mass transfer, a continual (steady) jet is combined with the synthetic (zero-net-mass-flux) jet. The resulting mixed pulsed jet exhibits a significant non-zero blowing component: the ratio of the extrusion and suction mass fluxes are approximately three in the actuator orifice exit. Measurements of the flow field velocity and mass transfer on the wall (using hot-wire anemometer and naphthalene sublimation technique) have been performed. An anticipated heat/mass transfer enhancement of the mixed pulsed jet was experimentally confirmed..

1. Introduction

Continual (steady) jets (CJs) can achieve very high heat transfer at their impingement onto walls [1–3]. The synthetic jets (SJs) are studied since the end of nineties [4] for a possible control of primary flows [5, 6] and for cooling applications [7–9]. The present paper focuses on an impingement heat/mass transfer. An oscillation character of SJs is used to enhance the transfer and, moreover, a non-zero blowing component is added to improve the transport processes even more.

2. Hot-wire and mass transfer experiments

The velocity distribution was measured by the hot-wire anemometer (DANTEC StreamLine 90N10) by the single-sensor wire probe (55P11). The phase averaging of the velocity during one cycle was carried out, and the velocity decomposition gives $u = U + U_f + u'$, where U is the time–mean velocity, U_f is the periodic phase-locked component, and u' is the fluctuation component (represented by the *rms* velocity fluctuations). Local mass transfer was measured using the naphthalene sublimation [7–9]. Three round (D=8.0 mm) air jets were studied:

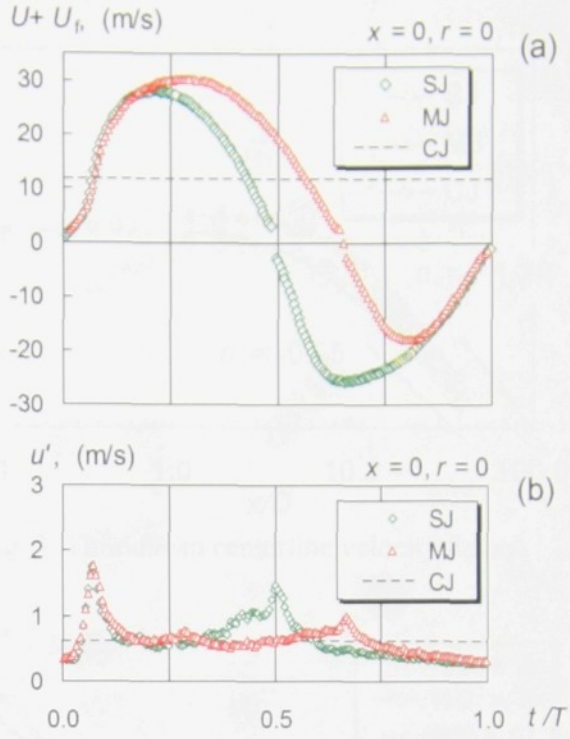

Fig. 1. Centerline velocity during one cycle of SJ and MJ; (a) phase averaged velocity, (b) rms velocity fluctuations.

(1) zero-net-mass-flux SJ without blowing component (purely alternating jet with zero mass-flux). The actuating frequency was f = 75 Hz, the input electrical power 4.0 W [8, 9]. The typical time-mean cross-stream orifice velocity (integrated over the extrusion stroke [4, 5]) was U_{0A} = 8.3 m/s (i.e. the Reynolds number $Re_{SJ} = U_{0A} D/\nu$ = 4 100).

(2) Mixed pulsed jet with an additional blowing component (MJ). The actuating frequency was f = 95 Hz, the input electrical power was identical with SJ. The actuator is supplied by the mean flow from a compressor, the added mean-flow cross-stream orifice velocity component was the same as the time-mean cross-stream orifice velocity of SJ (U = 8.3 m/s).

(3) Continual (steady) jet (CJ). The input electrical power into the actuator was zero; the jet was created solely from a compressor supply. The typical cross-stream velocity through the nozzle was U = 9.9 m/s (Reynolds number $Re_{CJ} = UD/\nu$ = 5 000).

Fig. 1 shows results of the hot-wire measurement in the actuator orifice (x = 0), on the axis (r = 0); the positive and negative velocities mean the extrusion and suction, respectively. The velocity cycle of SJ is nearly sinusoidal one.

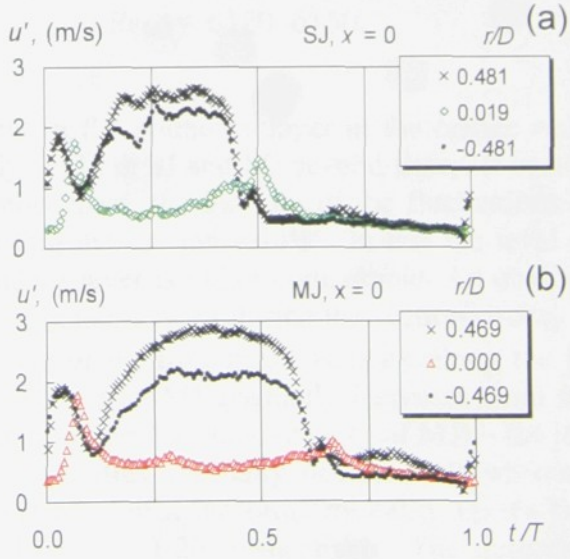

Fig. 2. rms velocity fluctuations during one cycle in the boundary layer and on the axis; (a) SJ, (b) MJ.

The additional blowing component of MJ causes an essential deformation of the cycle. Surprisingly, an increase of the maximum extrusion velocity of MJ is very small. The main effect of the blowing component is the extension of the extrusion stroke: the extrusion times of SJ and MJ are $T_E/T = 0.49$ and 0.66, respectively (where T is the time period, i.e. $T = 1/f$). The resulting time-mean cross-stream orifice velocity (integrated over the extrusion stroke [4, 5]) is $U_{0A} = 12.2$ m/s (Reynolds number $Re_{MJ} = U_{0A} D/\nu = 6\,100$), and the ratio of the extrusion and suction mass fluxes is 3.1.

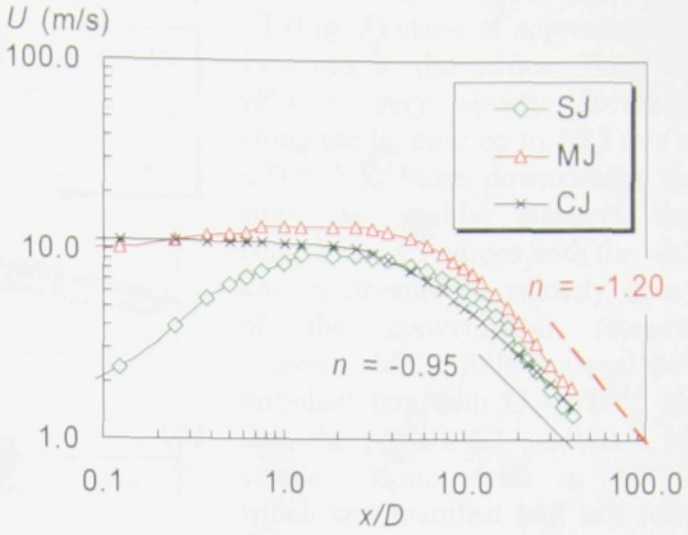

Fig. 3. Time-mean centerline velocity decay.

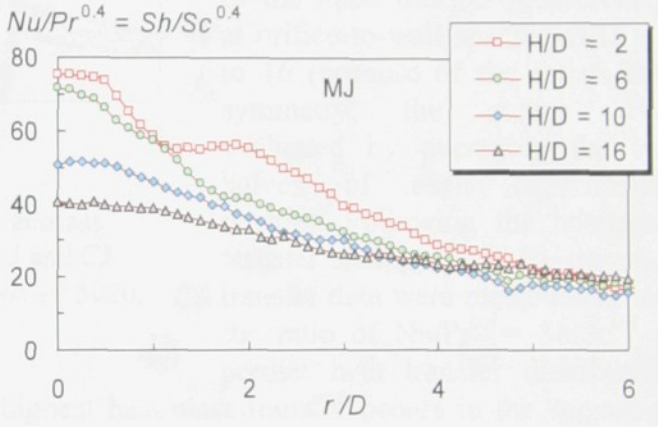

Fig. 4. Local heat/mass transfer onto exposed wall for MJ impingement, $Re_{MJ} = 6120–6150$.

Fig. 1(b) shows the *rms* velocity fluctuations. Both fluctuation curves have two maxima during the cycle: first maxima occur at t/T~0.07 – they are linked with the inflection point on the velocity curves; the second maxima are caused by the starts of the suction strokes, when the velocity changes the orientation (see Fig. 1(a)).

Fig. 2 shows that the rms velocity fluctuations are quite different in the boundary layer at the orifice wall, where the fluctuations increase dramatically for both SJ and MJ several times. It occurs during the extrusion stroke only. On the other hand, the increase of the fluctuations in the boundary layer is relatively smaller during the suction stroke – in fact the level of the fluctuation on the axis and in the boundary layer is rather comparable. An obvious reason is that the actuator draws in a relatively quiescent air during the suction stroke.

Fig. 3 shows the streamwise variation of the time-mean velocity along the jet centerline. Firstly, the time-mean velocities of SJ an MJ gradually increases from the actuator (from zero velocity of SJ, and from non-zero blowing velocity of MJ) – the jets are synthesized. Further downstream, the velocities gradually decrease: downstream $x/D > 15–20$, the velocity decays for SJ and MJ fulfill the proportionality $U \sim (x/D)^n$ with the exponent approximately $n = -1.15$ and -1.20, respectively. The described results are in accordance with discussions of SJ from Trávníček et al. [9]: SJ from the present actuator starts to be effectively non-periodic from $x/D > 15–20$.

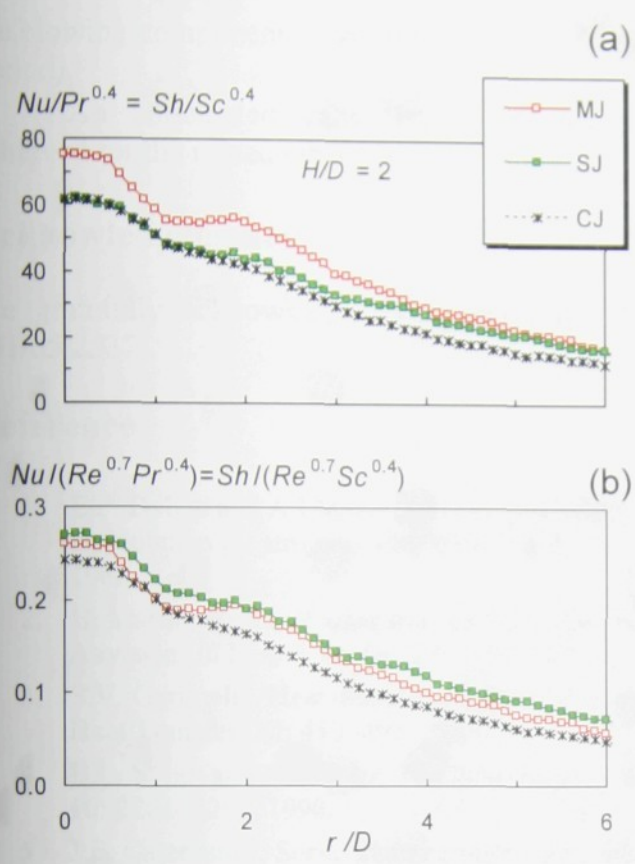

Fig. 5. Comparison of the heat/mass transfer distribution for SJ, MJ and CJ, Re_{SJ} = 4240, Re_{MJ} =6120, and Re_{CJ} = 5020.

The time-mean velocity of CJ (Fig. 3) starts at approximately 11.2 m/s in the orifice. Then the velocity very slowly decreases along the jet core up to 10.2 m/s at x/D = 2.5. More downstream the slope is visibly steeper; this behavior of CJ agrees with the well known streamwise velocity decay of the conventional (steady) axisymmetric fully developed turbulent jets with $U \sim x/D^{-1.0}$ (in fact, the present CJ exhibits a bit smaller slope with $n \sim -0.95$, which can manifest still not fully developed CJ).

Fig. 4 presents four profiles of the mass transfer measurement at orifice-to-wall spacing H/D = 2 to 16 (because of the satisfactory symmetry, the curves were evaluated by averaging the two halves of each experimental profile). Following the heat/mass transfer analogy [1, 8, 9], the mass transfer data were recalculated into the ratio of $Nu/Pr^{0.4} = Sh/Sc^{0.4}$ to predict heat transfer distribution. According to our expectation, the highest heat/mass transfer occurs in the stagnation point on the axis, and increasing orifice-to-wall spacing causes a reduction of the heat/mass transfer. It is worthy to note here that the so-called "secondary peaks" occur distinctly at H/D = 2, r/D = 1.9; other distributions decrease monotonously with the radial distance from the stagnation point as the bell-shaped curves.

Fig. 5 compares the heat/mass transfer distributions of MJ, SJ, and CJ at H/D = 2. The stagnation heat/mass transfer of SJ and CJ is practically identical, the highest value was achieved by MJ - the enhancement in the stagnation point is approximately 22 %. Obviously, this increase is partly caused by the higher Reynolds number Re_{MJ}.

To eliminate the Reynolds number effect and following the heat/mass transfer analogy [1, 8, 9], the results were recalculated into the ratio of $Nu/(Re^{0.7}Pr^{0.4}) = Sh/(Re^{0.7}Sc^{0.4})$. Fig. 5(b) shows that the highest heat/mass transfer

4. Conclusions

The hot-wire and naphthalene mass transfer experiments have been performed with three round air jets: (1) zero-net-mass-flux synthetic jet, (2) mixed pulsed jet with an additional blowing component, and (3) continual (steady) jet. It was shown that the additional blowing component causes an essential deformation of the velocity cycle: an increase of the maximum extrusion velocity of is rather small, the main effect of

the blowing component is the extension of the extrusion stroke (up to 0.66 of the time period).

An anticipated enhancement of the impingement heat/mass transfer was achieved for the mixed pulsed jet.

Acknowledgements

We gratefully acknowledge the support of GA CR (projects no. 101/05/2681 and 101/05/2537).

References

1. E.P. Dyban and A.I Mazur. Convection Heat Transfer in Impinging Jets (Konvektivnyj teploobmen pri strujnom obtekanii tel). 1st ed., Naukova dumka, Kiev (in Russian), 1982.
2. H. Martin. Heat and mass transfer between impinging gas jets and solid surfaces. Advances in Heat Transfer, 13: 1–60, 1977.
3. S.V. Garimella. Heat transfer and flow fields in confined jet impingement. Annu. Rev. Heat Transfer, XI: 413–494, 2000.
4. B.L. Smith and A. Glezer. The formation and evolution of synthetic jets. Phys. Fluids, 10: 2281–2297, 1998.
5. J.E. Cater and J. Soria. The evolution of round zero-net-mass-flux jets. J. Fluid Mech., 472: 167–200, 2002.
6. A. Glezer and M. Amitay. Synthetic jets. Annu. Rev. Fluid Mech, 34: 503–529, 2002.
7. Z. Trávníček and V. Tesař. Annular synthetic jet used for impinging flow mass-transfer. Int. J. Heat Mass Transfer, 46: 3291–3297, 2003.
8. Z. Trávníček, T. Hyhlík and F. Maršík. Synthetic jet impingement heat/mass transfer. Journal of Flow Visualization and Image Processing, (in press), 2006.
9. Z. Trávníček, J. Vogel, T. Vít and F. Maršík. Flow field and mass transfer experimental and numerical studies of a synthetic impinging jet. In 4th International Conference on Heat Transfer, Fluid Mechanics and Thermodynamics – HEFAT2005 (Edited by J.P. Meyer and A.G. Malan), Cairo, Egypt, No. ZT4, 2005.

CHAPTER 10

ANALYSIS OF A SJ PIEZO-CERAMIC PULSATION GENERATOR

Authors: P. Dančová[1,2], T. Vít[1,2], Z. Trávníček[2]

[1] *Faculty of Mechanical Engineering, Technical University of Liberec, Hálkova 6, 461 17 Liberec, Czech Republic*

[2] *Institute of Thermomechanics, Academy of Sciences of the Czech Republic, Dolejškova 5, 182 00 Prague 8, Czech Republic*

Published:

Developments in Machinary Design and Control, 11.-14.9.2007, Červený Kláštor

Abstract

This paper presents results of measurements based on the vibrometry principle: the results of an Eigen frequency measurement, a diaphragm motion velocity measurement, and an FEM simulation of piezoelectric element dynamics.

1. Basic Principle of a Synthetic Jet (SJ)

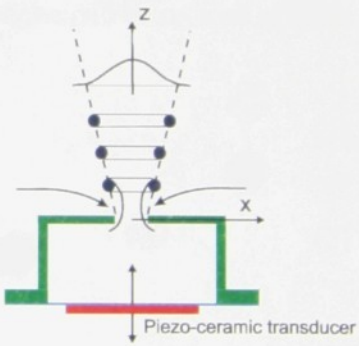

Fig.1 Basic principle of a SJ

Synthetic Jets are jets of fluid, which are generated by periodic pulsations of fluid. An oscillating force pushes and pulls this fluid through an orifice (nozzle) from the cavity of an actuator. Vortex rings form at the lip of the orifice. These rings move with the velocity U_0, which must be high enough to prevent interaction with any suction in the orifice. The vortex rings develop and dissipate, and the SJ takes on the characteristics of a free jet when it is far enough from the end of the orifice. The main advantage of a SJ is the zero-net-mass-flux jet which eliminates the necessity of piping for the fluid inlet. Though the nozzle works with zero-net-mass-flux, the momentum in direction z is non-zero. Equipment for a SJ can have various designs, but the main mechanism and principle is mostly similar.

The pulse generator for the fluid can work on the principle of a loudspeaker, piezo crystal, electromagnet, piston or other device. It is necessary to choose an optimal type and construction of an actuator in relation to the supposed working frequency and

amplitude range, working temperature, type of working medium and required load of the unit.

2. Piezoceramic Transducer Characteristics

Piezoceramic transducers (PCT) are used as actuators in many microelectronics or medical applications. Typical uses in microelectronics include miniature cooling devices or in medical applications as nebulizers or drug dosing devices.

Fig.2 The Piezoceramic Transducer

Use of a PCT as a pulse generator has many significant advantages, e.g. applicability in different fluids, in broad temperature ranges, and in heavy duty facilities. Other advantages of a PCT are a long operational lifetime and low power consumption.

It is necessary to know both static and dynamic characteristics of a PCT for a correct description of SJ function (behavior).

A PCT is composed of two basic layers – a piezoceramic layer and a metallic membrane. The piezoceramic material is usually based on the oxides of lead (Pb), zirconium (Zr) or titanium (Ti) solid solutions and is piezoelectrically active. The metallic membrane is piezoelectrically neutral. These two layers are fixed firmly together. A thin silver layer is coated on one side of the piezoceramic to form an electrode. The second electrode is mostly comprised of a piezoelectrically neutral metal plate.

A physical description of piezoceramic characteristics include the following equations, which describe the elastic (1), electric (2) and piezoelectric behaviors of state (3) and (4)

$$\nabla \cdot T = 0 \tag{1}$$

$$\nabla \cdot D = 0 \tag{2}$$

$$T_{ij} = c_{ijkl} S_{kl} - e_{ijk} E_k \tag{3}$$

$$D_k = e_{kij} S_{ij} + \varepsilon_{kj} E_j \tag{4}$$

where T, D, S, E, c, e and ε are stress tensor, vector of electric flux density, strain tensor, vector of electric field, elastic modulus tensor, piezoelectric coefficient tensor and permittivity tensor respectively.

The stated equations describe the interaction between elastic and electric properties of a structure.

Some parameters are in the form of elastic moduli tensor, piezoelectric coefficients tensor and permittivity tensor. When the axi-symmetry of piezoceramics is taken into account, these tensors can be written in a matrix form as follows:

$$c = \begin{pmatrix} c_{11} & c_{12} & c_{13} & 0 & 0 & 0 \\ c_{12} & c_{11} & c_{13} & 0 & 0 & 0 \\ c_{13} & c_{13} & c_{33} & 0 & 0 & 0 \\ 0 & 0 & 0 & c_{44} & 0 & 0 \\ 0 & 0 & 0 & 0 & c_{44} & 0 \\ 0 & 0 & 0 & 0 & 0 & c_{66} \end{pmatrix} \tag{5}$$

$$e = \begin{pmatrix} 0 & 0 & 0 & 0 & e_{15} & 0 \\ 0 & 0 & 0 & e_{15} & 0 & 0 \\ e_{31} & e_{31} & e_{33} & 0 & 0 & 0 \end{pmatrix} \tag{6}$$

$$\varepsilon = \begin{pmatrix} \varepsilon_{11} & 0 & 0 \\ 0 & \varepsilon_{11} & 0 \\ 0 & 0 & \varepsilon_{33} \end{pmatrix} \tag{7}$$

3. Vibrometry Measurement

The analysis of a PCT is based on the Laser Doppler Vibrometry principle. Laser Doppler Vibrometry (LDV) is a non-contact vibration measurement technique using the Doppler Effect. A LDV permits the measurement of hot, miniature or soft surfaces, even under water, without mass-loading.

A Laser Doppler Vibrometer is based on the principle behind the detection of the Doppler shift of coherent laser light that is scattered from a small area of a test object. The object scatters or reflects light from the laser beam, and the Doppler frequency shift is used to measure the component of velocity, which lies along the axis of the laser beam.

The Ometron VQ-1000-D (B&K 8338) Portable Digital vibrometer is used to measure precisely the velocity of the oscillating membrane. Below are the main parameters of the vibrometer:

Frequency range: 0.5 Hz - 22 kHz

Measurement ranges (full scale (peak-peak)): 20 mm/s, 100 mm/s, 500 mm/s

Spurious free dynamic range (SFDR): > 90dB

Best resolution: 0.02 μm/s/Hz0.5

The response of a PCT to a harmonic or square driving signal at different frequencies was measured. In both cases, the frequency of the driving signal was selected in a stepwise manner – 50, 60, 100, 200, 950 and 1200 Hz.

An Fast Fourier Transform (FFT) of the response of a single pulse was used to determine the eigenfrequencies of the piezoceramic transducer.

LabView software was used to acquire and analyze the signal obtained from the Ometron vibrometer.

4. Numerical Simulation

A numerical simulation was carried out to obtain information about the dynamic response to the driving electrical signal: to discover any deformation of the membrane at different frequencies (frequency analysis), to find eigenfrequencies, and to show modal shapes (Modal analysis). Numerical simulation of the piezoelectric element motion was carried out using the Finite Elements Method (FEM). An FEM simulation makes numerical simulations of such a complex phenomenon as a piezoceramics-actuator-fluid interaction possible.

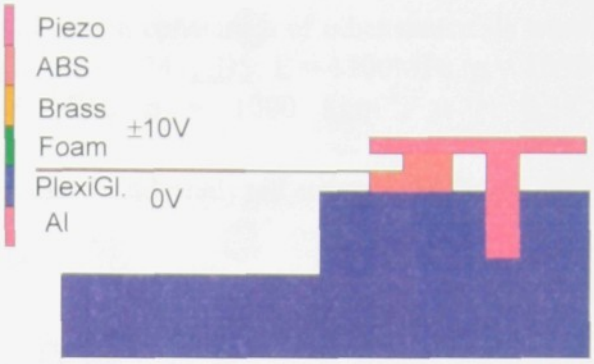

Fig. 3 Utilized materials and boundary conditions

It is necessary to set the boundary conditions and the material characteristics of the PCT to achieve correct simulation results. Utilized boundary conditions and materials are shown in Fig. 3.

The boundary conditions were as follows: the PCT was fixed on the perimeter; the piezoceramic was fed with a voltage of ±10V on the top surface, the voltage of the metallic membrane was kept constant at a value of 0V. No influence of the working fluid was modeled.

The material coefficients of the electromechanical characteristics, i.e. elastic (c), piezoelectric (e) and dielectric (ε) characteristics, are the tensors from section 2. For our PCT, the tensors can be written in the following form:

$$c = \begin{pmatrix} 5.1e+10 & 2.0e+10 & 2.0e+10 & 0 & 0 & 0 \\ 2.0e+10 & 6.4e+10 & 2.0e+10 & 0 & 0 & 0 \\ 2.0e+10 & 2.0e+10 & 6.4e+10 & 0 & 0 & 0 \\ 0 & 0 & 0 & 2.0e+10 & 0 & 0 \\ 0 & 0 & 0 & 0 & 2.0e+10 & 0 \\ 0 & 0 & 0 & 0 & 0 & 2.0e+10 \end{pmatrix} \tag{8}$$

$$e = \begin{pmatrix} 0 & 0 & 0 & 0 & 12.3 & 0 \\ 0 & 0 & 0 & 12.3 & 0 & 0 \\ -5.4 & -5.4 & 15.7 & 0 & 0 & 0 \end{pmatrix} \tag{9}$$

$$\varepsilon = \begin{pmatrix} 1.53174e-8 & 0 & 0 \\ 0 & 1.53174e-8 & 0 \\ 0 & 0 & 1.53174e-8 \end{pmatrix} \tag{10}$$

The Young modulus E, density ρ and Poisson constant μ of other materials were as follows: Brass: E = 100GPa, $\rho = 8600 kgm^{-3}$, $\mu = 0.34$; ABS: E = 4300MPa, $\rho = 1050 kgm^{-3}$, $\mu = 0.38$; Plexi Glass: E = 1000MPa, $\rho = 1000 kgm^{-3}$, $\mu = 0.38$; Foam: E = 4MPa, $\rho = 400 kgm^{-3}$, $\mu = 0.4$.

The simulations were prepared, processed and analyzed using MSC.Marc and Marc Mentat software.

5. Results

5.1. Determination of the PTC Eigenfrequency

The determination of the PCT eigenfrequency is the first step in conducting measurements. The PCT eigenfrequency is determined from the FFT response to a single pulse (see Fig. 4). It is evident that the first eigenfrequency of the PCT corresponds to a value of 960Hz.

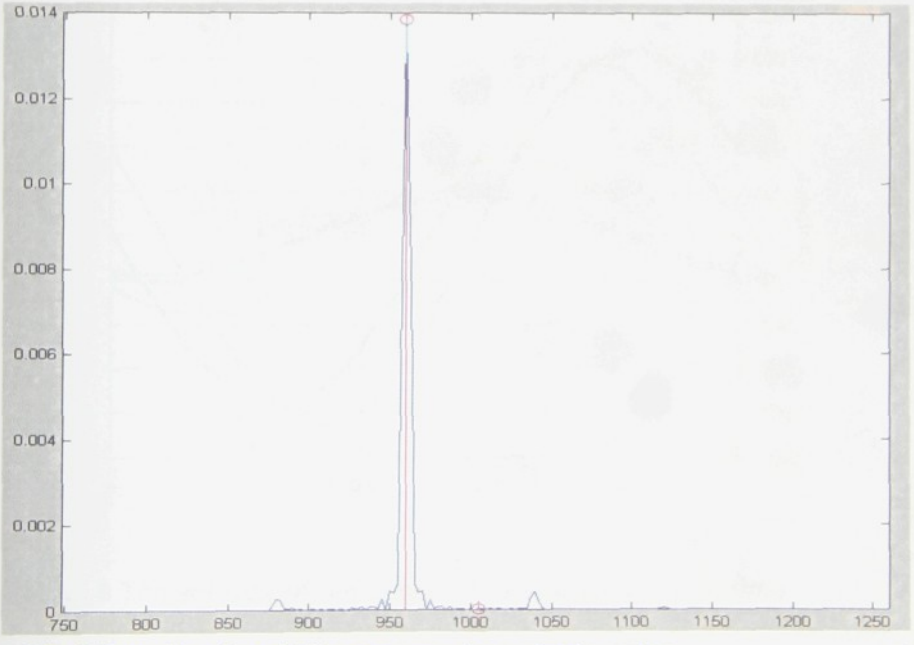

Fig.4 Results of an FFT response to a single pulse f

5.2. Vibrometry Measurement

Figures 5 and 6 show the results of vibrometry measurements. In this case, the driving signal is harmonic and has frequencies of 50, 60, 100, 200 and 950Hz. The value of frequency 950Hz is close to the eigenfrequency determined in previous experiments. The amplitude of the actuating voltage on the piezoceramic was adjusted to ±10V.

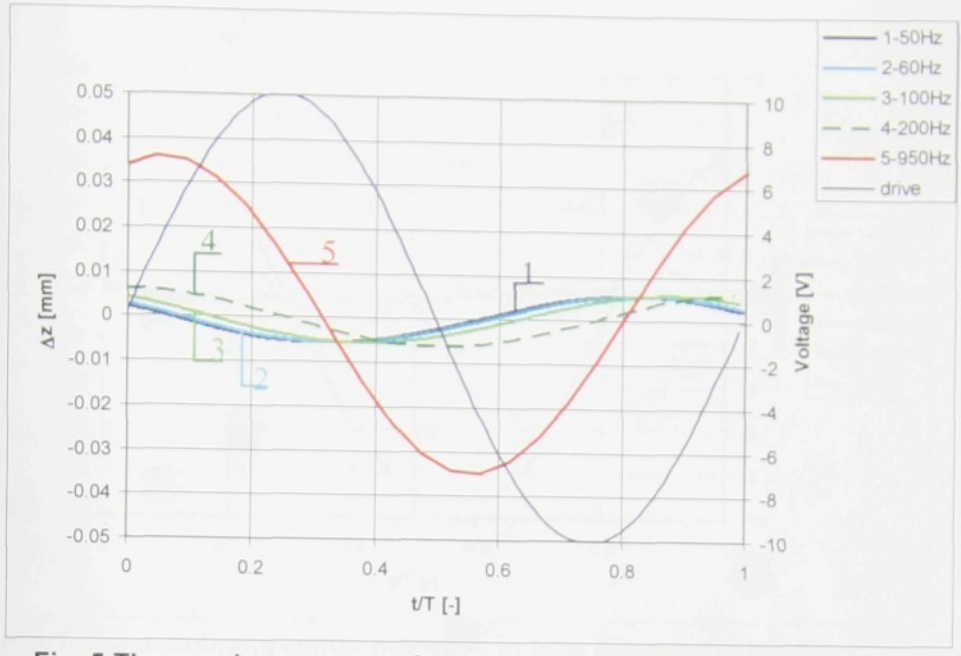

Fig. 5 The membrane center deviation in time (sinusoidal driving signal)

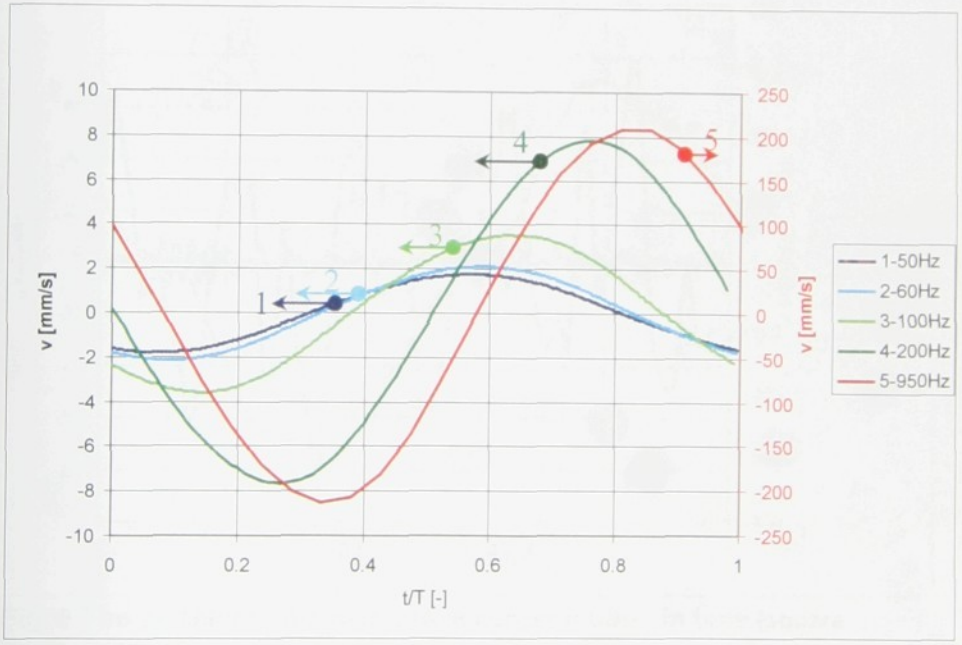

Fig. 6 The velocity of the center membrane motion in time (sinusoidal driving signal)

Figure 5 shows the time deviation of the center of the membrane. It is evident that the largest displacement of the membrane center was achieved at the frequency 950Hz, which was close to its eigenfrequency of 960Hz.

Figure 6 shows the time deviation of the velocity of the membrane center. The highest velocity was achieved at the driving signal frequency of 950Hz. The value of the velocity at 950Hz is at its maximum, two orders higher than the velocity at other frequencies. That is why its range is shown on the right side axis.

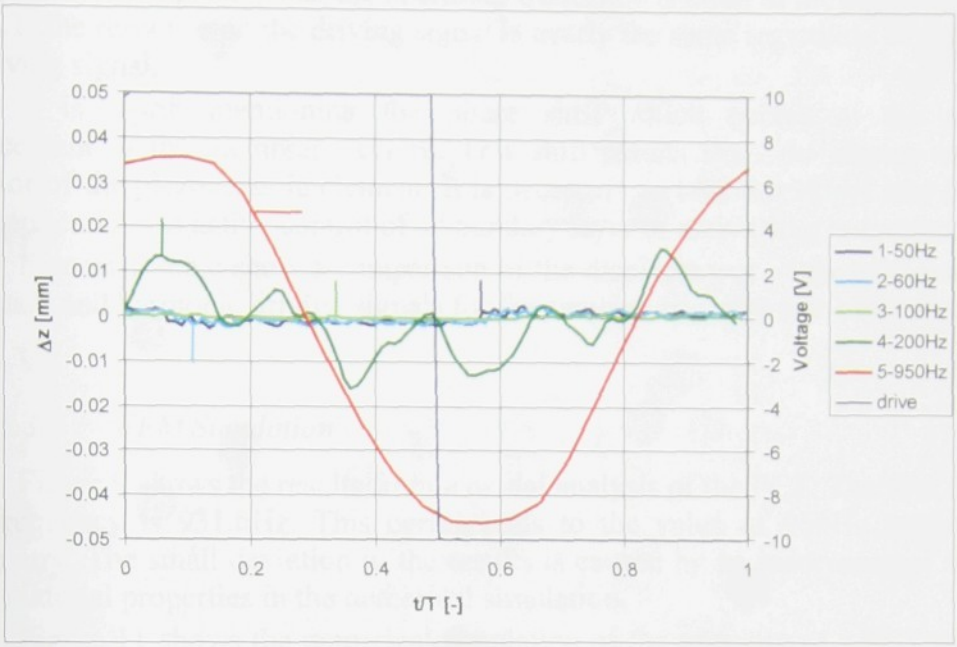

Fig. 7 The membrane center deviation in time (square driving signal)

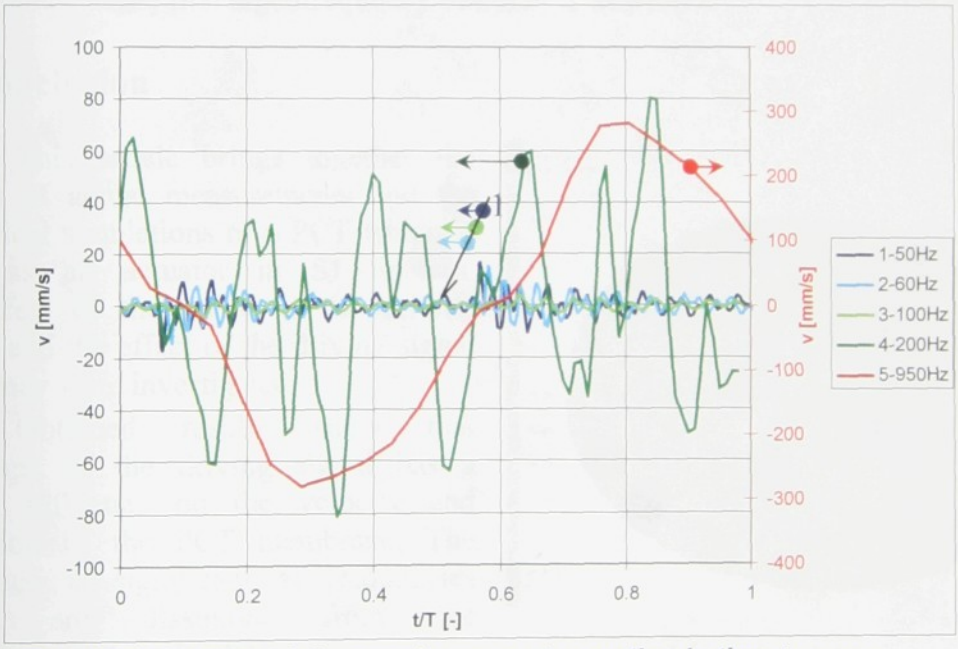

Fig. 8 The velocity of the membrane center motion in time (square driving signal)

Figures 7 and 8 shows the results of vibrometry measurements in the case of a square driving signal at frequencies 50, 60, 100, 200 and 950 Hz. Fig. 7 shows membrane displacement. In all cases except at 950Hz, peak values of membrane displacement are lower than the results achieved from the harmonic signal (cf. Fig. 5). The peak values and the shape of the time deviation are nearly the same for the driving frequency of 950Hz. It is also evident that membrane displacement at a frequency of 950Hz is sinusoidal in character, regardless of the square character of the driving signal.

Figure 8 shows the values of membrane center velocities, which are much higher than the velocities generated by the harmonic signal. Consequently, a PCT fed with a square driving signal is more powerful (has a higher pumping output) than a PCT fed

with a sinusoidal signal. When the operating frequency is close to the eigenfrequency of the PCT, the response on the driving signal is nearly the same regardless of the shape of the driving signal.

It is worth mentioning the phase shift which occurs at the maximum displacement of the membrane centre. This shift results from the electro-mechanical behavior of the piezoceramic element. It is necessary to take this effect into account in such applications as active control of a boundary layer or active drag reduction.

Figures 10a,b,c show a comparison of the displacement of the membrane center for square and harmonic driving signals for frequencies 200, 950 and 1200Hz.

5.3. FEM Simulation

Figure 9 shows the results from a modal analysis of the PCT. The first calculated eigenfrequency is 931.6Hz. This corresponds to the value of 960Hz achieved from vibrometry. The small deviation in the results is caused by an inaccuracy of the values of the material properties in the numerical simulation.

Figure 11 shows the numerical simulation of the response of a PCT on a single step 10V applied to the top surface. The frequency of the outstanding waves corresponds to the first eigenfrequency of the PCT at 960Hz.

6. Conclusion

This article brings together the results of actual measurements and the numerical simulations of a PCT which is used as an actuator in SJ devices. The effect of the shape of the driving signal and the effect of the driving signal frequency were investigated.

Obtained results show that the shape of the driving signal has a strong influence on the velocity and deviation of the PCT membrane. The influence is significant at frequencies which are dissimilar from the eigenfrequency of the PCT.

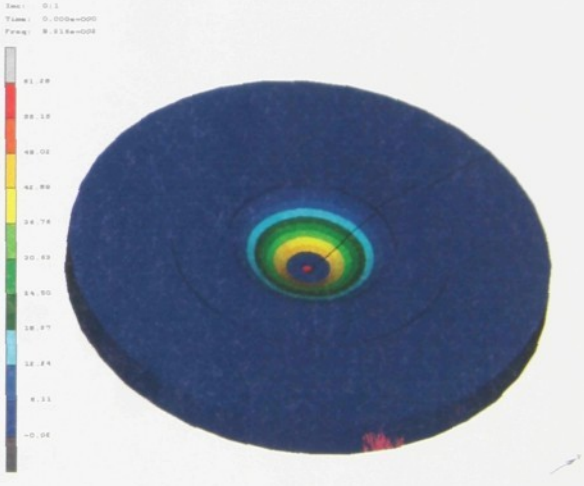

Fig. 9 The displacement of the membrane at the first eigenfrequency

A comparison of the experimental and numerical results demonstrates that the usage of numerical simulations for vibration analysis of piezoceramic elements is possible. This paper reveals that the results of numerical simulations agree almost completely with the results of our experiments. Numerical models should be used for reliable descriptions of the studied phenomenon. These results should be used to improve the design and efficiency of SJ device actuators.

Follow-up research will show the interaction between the movement of the membrane and the motion of the working fluid. Experiments in both air and water are planned.

Acknowledgments

We gratefully acknowledge the support of the Grant Agency of the Czech Republic GAČR 101/05/2681 and Research Target of the Ministry of Education of the Czech Republic - MSM 4674788501.

References

1. Dančová P., Studie proudění typu "Synthetic Jet", Diplomová práce, (Analysis of the "Synthetic Jet", Diploma thesis), TU Liberec, Czech Republic, (2006), in Czech language.
2. Z. Trávníček, J. Vogel, J. Hošek, T. Vít: Numerical simulation and flow vizualization of Synthetic Jet, conference "Topical Problems of Fluid Mechanics 2005", Institute of Thermomechanics AS CR, Prague, February 16.-17., (2005).
3. OMETRON: Vibration measurement system, http://www.ometron.com/home.html
4. J. Erhart: Piezoelektrické "chytré" materiály pro elektrotechniku, Elektro 11, 4-7, (2002), in Czech language.
5. Smith B. L., Glezer A., The formation and evolution of synthetic jet, Phys. Fluids, Vol. 10 (1998), 2281 - 2297.

CHAPTER 11

CONCLUSIONS

The particular results for each research topic are presented at the ends of individual chapters. Hence only the most significant results will be mentioned here.

It has been found that cylinder heating in water increases the frequency of the vortex shedding (thermal effect in water). The present results confirm that the concept of effective temperature – originally suggested for heated cylinders in air – is suitable and extendable to heated cylinders in water.

Based on these successful experiments a new towing tank has been built at the Technical University of Liberec. This tank allows us to prepare, among other things, even more detailed experiments and to repeat the set of experiments not only for water and air but for other liquids as well. For example, the flow behind a cooled body or the control of a bluff body wake by pulsatile jets seems to be a motivation for further research. Experiments carried out for different values of temperature ratio or for liquids with different viscosity would be very helpful in analyzing the stability of the boundary layers.

The first papers which deal with the SJ were focused on the main parameters of SJ, the selection of suitable experimental methods and the validation of the first experimental results. The first experiments were based on the work of Swift and Glazer. The experiments presented in *Chapter 7*, however, show the results of unique experiments with water as the working fluid. In the latest research these basic experiments help to study another complex problem which is the interaction of the SJ with a crossflow (see [32]).

The results presented in *Chapter 8* and *Chapter 9* are closely connected with the practical application of SJ for improving the efficiency of heat transfer. This research shows four different setups of heating/cooling devices and their influence on the value of the heat transfer coefficient.

Fig.11.1. Towing tank at TU Liberec

We must mention the great interest from industry in developing an applicable device. Currently there is intensive cooperation with companies working in the field of plastics manufacturing to develop a device to heat up molds that will work on the principle of SJ. Projects focusing on the construction of a valveless pump to be used in practice, and on the SJ principle used in the technology of nanofiber production, are also under preparation.

REFERENCES

[1] Vít T: Experimental and Theoretical Study of the Heated Coanda Jet, Dissertation Thesis, TU Liberec 2004

[2] Vít T, Dančová P, Kotek M, Pírková L: Použití různých experimentálních metod pro analýzu proudění typu „Synthetic Jet",XXIV mezinárodní věd. konf. kateder a pracovišť mech. tekutin a termomechaniky, pp. 45-49, Blansko, ČR, 2005

[3] Kovasnay L.S.G., (1949) Hot-wire investigation of the wake behind cylinders at low Reynolds numbers, Proc.R.Soc.London, Ser. A 198, 174-190.

[4] Collis D.C., Williams M.J. (1959) Two–dimensional convection from heated wires at low Reynolds numbers, J. Fluid Mechanic, 6, 357-384.

[5] Strouhal V. :Uber eine besondere Art der Tonerregung. Wied. Anna. Phys. und Chem. (Leipzig),Series 3 216-251 (1878).

[6] Rayleigh L.:Aeolian tones. *Phil. Mag.* 29 433 (1915)

[7] von Kármán T.: The Wind and Beyond: Theodore von Kármán Pionneer in Aviation and Pathfinder in Space , New York: Little, Brown (1967).

[8] Williamson C.H.K. (1996) Vortex dynamics in the cylinder wake, Annual. Rev. Fluid. Mech., 28, 477-539.

[9] Van Dyke M.:"An Album of Fluid Motion", New York: Parabolic (1982).

[10] Williamson C.H.K. (1989) Oblique and parallel modes of vortex shedding in the wake of a circular cylinder at low Reynolds numbers, J. Fluid Mech., 206, 579-627.

[11] Ren M., Rindt C. C. M., van Steenhoven A. A., "Experimental and numerical investigation of the vortex formation process behind a heated cylinder," Phys. Fluids 16, 3103 (2004).

[12] Huerre P.: 4.Open Shear Flow Instabilities, in Perspectives in Fluid Dynamics, Edited by G.K. Batchelor, H.K.Moffatt, M.G.Worster, Cambridge University Press 2000

[13] Provansal M., Mathis C., Boyer L., "Bénard-von Kármán instability: transient and forced regimes" J. Fluid Mech. 182 1–22 (1987).

[14] Landau L.D., Lifshitz E.M.: Fluid Mechanics, Second Edition: Volume 6 (Course of Theoretical Physics), Butterworth-Heinemann; 2 edition (January 15, 1987)

[15] Mathis C., Provansal M., Boyer L.,"The Bénard-von Kármán instability: an experimental study near the threshold" J. Physique Lett, 45 L-483–L-491 (1984).

[16] Sreenivasan K.R., Strykowski P.J., Olinger D.J., "Hopf bifurcation, Landau equation and vortex shedding behind cylinders", in Forum on Unsteady Flow Separation (eds.K. N. Ghia), New York ASME, FED 52 1–13 (1986).

[17] Oertel H.:Wakes behind blunt bodies. Ann. Rev. Fluid Mech. : 539 (1990).

[18] Monkewitz A.:The absolute and convective nature of instability in two-dimensional wakes at low Reynolds numbers. Phys. Fluids 31, 999-1096, 1988

[19] Ramberg S.E., "The effects of yaw and finite length upon the vortex wakes of stationary and vibrating cylinders." J. Fluid Mech. 128 81 (1983).

[20] Tritton D.J., "Experiments on the flow past a circular cylinder at low Reynolds numbers." J.Fluid Mech. 6 547 (1959).

[21] de Boer P., Coherent structures in synthetic jets and non-isothermal wakes, Research Report,Institute of Thermomechanics AS CR, No. Z-1333/03, Prague, 2003.

[22] Yang, W-J.: Handbook of flow visualization, Hemisphere Publish. Corp., 1989

[23] Cornell, D.: Smoke generation for Flow Visualisation, Mississippi State Univ, Aerophysics Res. Rep, 54, 1964

[24] Travníček, Z., Wang, A-B., Maršík, F.: Flow visualization of the laminar vortex shedding behind a cooled cylinder, In: Int. Symposium on Experimental Mechanics ISEM (CD- proceedings), 2002 - Taipei, C209

[25] Honji H., Taneda S., Tatasuno M., "Some practical details of the electrolytic precipitation method of flow visualization," Rep. Res. Inst. Appl. Mech. (Kyushu Univ.) 28, 83 (1980)

[26] Geankoplis, C.J. Transport processes and separation process principles (2003). Fourth Edition, p.475.

[27] Bruun, H. H.:Hot wire anemometry, Oxford Univ. Press, 1995

[28] Perry, A. E.:Hot Wire Anemometry, Clarendon Press, Oxford, 1982

[29] van der Hegge Zijnen, B. G: Modified correlation for the heat transfer by natural and by forced convection from horizontal cylinders, Appl. Sci. Res, A6, 1956, pp. 129-140

[30] Swaminathal, M. K., Rankin, G. W., Sridhal, K.: A note on the response equations for hot-wire anemometry, Jour. Fluids Eng, 108, 1986, p. 115-118

[31] Sonnenberger R., Graichen K., Erk P.: Fourier averaging: a phase-averaging method for periodic flow, Journal Experiments in Fluids, Volume 28, Number 3 / March, 2000, pp. 197-283

[32] Dančová P, de Lange R, Trávníček Z, Vít T: PIV Measurements of a Synthetic Jet in a Channel Flow, 12th International conference: Developments in Machinary Design and Control, September 9–12, 2008, Nowogród, Poland pp.23-24 + CD